מכון ויצמן למדע

WEIZMANN INSTITUTE OF SCIENCE

Thesis for the degree
Doctor of Philosophy

Submitted to the Scientific Council of the
Weizmann Institute of Science
Rehovot, Israel

עבודת גמר (תזה) לתואר
דוקטור לפילוסופיה

מוגשת למועצה המדעית של
מכון ויצמן למדע
רחובות, ישראל

By
Arbel Haim

מאת
ארבל חיים

מצבי מָיוֹרָנָה קשורים במערכות חומר מעובה: מימושים וחתימות פיסיקאליות

Majorana Bound States in Condensed Matter Systems: Realizations and Physical Signatures

Advisor:
Prof. Yuval Oreg

מנחה:
פרופ' יובל אורג

August 2016

ניסן תשע"ו

Contents

Abstract

In 1937 Ettore Majorana hypothesized the existence of a putative fermionic particle whose its own antiparticle. Whether this particle, which has received the name Majorana fermion, exists in nature as an elementary particle is still unknown. In condensed matter physics, however, we are not limited by what nature is kind enough to offer. Indeed, Majorana fermions (usually called Majorana zero modes or Majorana bound states in the context of condensed matter physics) can emerge as a zero-energy excitation at the boundaries of a new phase of matter known as a topological superconductor. This phase of matter can arise in low-dimensional systems due to interplay between superconductivity, magnetism and spin-orbit interaction. Much of the interest in Majorana bound states comes from their nonlocal nature, a property which makes them insensitive to local perturbations and to decoherence. This, along with their non-abelian exchange statistics, makes them a potential platform for fault-tolerant quantum information processing.

When studying Majorana bound states in condensed matter physics, either from an application point of view, or from a purely theoretical one, several questions arise. First, what are the physical systems which give rise to topological superconductivity? In particular, what are the setups which are most robust and allow maximal control of the Majorana bound states? Second, what would be the physical signatures of the Majorana mode in these systems? and in particularly, can we witness their nonlocal nature? In the thesis presented here, we attempt to shed light on these issues.

We begin in chapter 1 by introducing the subject of topological states of matter, and by briefly reviewing the recent developments leading to the current status in the study of Majorana bound states. We focus in particular on realizations of topological superconductivity in semiconducting nanowires and signatures of Majorana bound states in these systems in differential conductance measurements.

Chapter 2 deals with the realization of a time-reversal invariant topological superconductor (TRITOPS). We show that, unlike the time-reversal broken case, here repulsive electron-electron interactions are crucial for realizing the topological phase. In particular, one cannot realize this phase in a noninteracting system coupled to a conventional s-wave superconductor. We then turn to study the effect of repulsive

interactions. We present and study a general low-energy model for a one-dimensional proximity-coupled system, showing that it is driven into the TRITOPS phase in the presence of short-ranged repulsive interactions. The effect of interactions is studied using both a mean-field approach and a renormalization group analysis. We further propose two experimental setups and show that they realize this model at low-energies. To test our conclusions we study a microscopic model for one of this setups using a numerical Hartree-Fock calculation and the density-matrix renormalization group.

In chapter 3 we study signatures of Majorana bound states. The first two sections therein discuss current cross correlations in a setup which we term *Majorana beam splitter*. This is a T-junction composed of a grounded topological superconductor and of two normal-metal leads which are biased at a voltage V. We show that the existence of an isolated Majorana bound state in the junction dictates a universal behavior for the cross correlation of the currents through the two normal-metal leads of the junction. The cross correlation is negative and approaches zero at high bias voltages as $-1/V$. This behavior is robust in the presence of disorder and multiple transverse channels, and persists at finite temperatures. In contrast, an accidental low-energy Andreev bound state gives rise to nonuniversal behavior of the cross correlation. We analyze in detail the special case of spin-resolved current correlations, where the distinction between the case of a Majorana bound state and that of a trivial Andreev bound state becomes most pronounced. In the last section of the chapter we examine the case of a long but finite topological superconductor, in which the two Majorana bound states at the boundaries of the system have a small overlap. While in an infinite system the Majorana bound state carries no charge, this is no longer true in a finite system, when the two Majorana bound states begin to overlap. We show that even though the density of states is peaked near the ends of the system, the acquired charge density is delocalized across the wire. This nonintuitive behavior can serve to identify weakly-coupled Majorana bound states in finite systems.

In chapter 4 we explore theoretically the possibility of realizing Majorana bound states in a robust and controllable setup. We propose achieving this by splitting the system into a chain of quantum dots, which are then tuned to the conditions under which the chain can be viewed as an effective Kitaev model, so that it is in a robust topological phase with well-localized Majorana states in the outermost dots. This setup overcomes the obstacles that disorder and high density of states pose to the creation of unpaired Majorana bound states in one-dimensional systems. The tuning algorithm that we develop involves controlling the gate voltages and the superconducting phases. Resonant Andreev spectroscopy allows us to make the tuning adaptive, so that each pair of dots may be tuned independently of the other.

The calculated quantized zero bias conductance serves then as a signature of the topological nature of the tuned phase.

Acknowledgments

First I would like to thank my PhD advisor Yuval Oreg. Thank you for teaching me how physics should be done. You have been a wonderful mentor to me, I learned a lot from you about physics, life, and their interface.

Thanks go also to Erez Berg. You have been like a second PhD advisor to me, and I was extremely lucky to collaborate with you. Your impact on this work is invaluable.

During my PhD study I have benefited from collaboration with many other people, and it is my pleasure to acknowledge all of them: Anton R. Akhmerov, Ian Appelbaum, Gilad Ben-Shach, Yonatan Cohen, Karsten Flensberg, Ion C. Fulga, Bertrand I. Halperin, Moty Heiblum, Jung-Hyun Kang, Anna Keselman, Felix von Oppen, Maria-Theresa Rieder, Yuval Ronen, Hadas Shtrikman, Konrad Wölms, and Amir Yacoby.

I am grateful to my office-mates, past and present, for making this journey so much fun: Assaf Carmi, Anna Keselman, Natalie Lezmi, Dean Mark, Maria-Theresa Rieder, Zohar Ringel, Yoni Schattner, and Inbar Seroussi.

I am in debt to my parents, Moshe and Shirley, and to my brother and sister, Tavor and Yarden. Thank you for always showing me your love and support.

Finally, I owe a special thank to my wife Michal for so many things, but mostly for providing balance to my life.

List of Publications

1. Arbel Haim, Konrad Wölms, Erez Berg, Yuval Oreg, Karsten Flensberg, "*Interaction-Driven Topological Superconductivity in One Dimension*", arXiv: 1605.09385

2. Arbel Haim, Erez Berg, Karsten Flensberg, Yuval Oreg, "*No-go theorem for a time-reversal invariant topological phase in noninteracting systems coupled to conventional superconductors*", arXiv:1605.07179

3. Yuval Ronen, Yonatan Cohen, Jung-Hyun Kang, Arbel Haim, Maria-Theresa Rieder, Moty Heiblum, Hadas Shtrikman,
"*Charge of a Quasiparticle in a Superconductor*", PNAS **113**, 1743-1748 (2016)

4. Arbel Haim, Erez Berg, Felix von Oppen, Yuval Oreg, "*Current Correlations in a Majorana Beam Splitter*", Phys. Rev. B **92**, 245112 (2015)

5. Arbel Haim, Erez Berg, Felix von Oppen, Yuval Oreg, "*Signatures of Majorana Zero Modes in Spin-Resolved Current Correlations*", Phys. Rev. Lett. **114**, 166406 (2015)

6. Gilad Ben-Shach, Arbel Haim, Ian Appelbaum, Yuval Oreg, Amir Yacoby, Bertrand I. Halperin, "*Detecting Majoranas in 1D wires by charge sensing*", Phys. Rev. B **91**, 045403, (2015)

7. Arbel Haim, Anna Keselman, Erez Berg, Yuval Oreg, "*Time-Reversal Invariant Topological Superconductivity Induced by Repulsive Interactions in Quantum Wires*",
Phys. Rev. B **89**, 220504(R) (2014)

8. Ion C. Fulga, Arbel Haim, Anton R. Akhmerov, Yuval Oreg, "*Adaptive tuning of Majorana fermions in a quantum dot chain*", New J. Phys. **15**, 045020 (2013)

Chapter 1

Introduction

1.1 Topological Phases of Matter

One of the main themes in condensed matter physics is the study of phases and of phase transitions. That is, the study of the various ways in which interaction between the constituents of matter can lead to distinct physical behaviors known as phases. One of the accomplishments of physics in the previous century was the understanding and classification of phases based on the notion of spontaneous symmetry breaking. Within this paradigm, due to Landau, a phase is characterized according to the symmetry which is spontaneously broken at the transition. For example, the ferromagnetic phase breaks spin-rotational symmetry, even though the interactions between the electrons are SU(2) symmetric. As another example, in a transition from a liquid to a solid the ions arranged themselves in a lattice, thereby spontaneously breaking translational symmetry.

The discovery of the quantum Hall effect (QHE) in 1980 by von Klitzing *et al.* [1] introduced a new notion of phase transitions which goes beyond Landau's paradigm. In the QHE, the transverse (Hall) conductance in a two-dimensional electron gas exhibits a series of plateaus as a function of magnetic field, in which it is precisely quantized to an integer value in units of e^2/h. Within these plateaus the spectrum of the system has a bulk gap and the longitudinal conductance drops to zero. The transition between plateaus is a second-order phase transition accompanied by a closing of the gap and a diverging correlation length. However, unlike continuous phase transitions which are described within Landau's theory, here no symmetry is broken, and no local order parameter exists. Instead, the distinction between the phases on both sides of the transition is topological [2]; one cannot go smoothly between the two phases (say by varying system's parameters) without closing the bulk gap in the process. The precise quantization of the Hall conductance has

its roots in the fact that it is a *topological invariant*; namely it cannot change in response to smooth variation of system parameters, so long as the bulk gap remains open. Although the bulk is gapped, current in the QHE is conducted through gapless modes which reside at the edge, and whose number corresponds to the Hall conductance. The existence of these edge modes is dictated by the topological nature of the bulk [3], and is a manifestation of the bulk-edge correspondence.

For a while it was thought that breaking of time-reversal symmetry (TRS) is crucial in order to have a topological phase, such as the QHE. The reason might be the fact that the Hall conductance vanishes in the presence of TRS. Following progress by Haldane [4], a breakthrough was made in 2005 when Kane *et al.* [5] introduced a model for a topological insulator (TI) with protected edge modes that, however, does not break TRS. While the Hall conductance indeed vanishes in this model, there is a different topological invariant which can only take one of two values, and cannot change as long as the bulk gap remains intact. While the topological invariant in the case of the QHE is a $\mathbb{Z}$ invariant (the Hall conductance can assume any integer value), the invariant in the case of the topological insulator is $\mathbb{Z}_2$; namely there are only two topologically distinct phases. The phase which supports edge modes is called the topological phase, while the one having gapped edges is called trivial.

In the case of quadratic Hamiltonians of fermions* a full topological classification exists [6, 7]. It is based on the presence or absence of time-reversal symmetry, particle-hole symmetry and their combination - the chiral symmetry. Time-reversal symmetry is defined as an antiunitary operator, Θ, which commutes with the Hamiltonian, $[\mathcal{H}, \Theta] = 0$. Particle-hole symmetry (PHS) is an antiunitary symmetry which anticommutes with the Hamiltonian, $\{\mathcal{H}, \Xi\} = 0$. The multiplication of these two symmetries forms a unitary operator, $\Pi = \Theta\Xi$. Chiral symmetry is said to exists if $\{\mathcal{H}, \Pi\} = 0$. It can be shown [8] that in the absence of ordinary symmetries (i.e. unitary operators which commute with the Hamiltonian), there can be at most only one TRS, and one PHS. It can further be shown, in this case, that acting with the same antiunitary symmetry twice is equivalent to the identity operator up to a sign, $\Theta^2 = \pm 1$, $\Xi^2 = \pm 1$. For each of the symmetries Θ and Ξ there are three options: absent, present and squares to $+1$, or present and squares to -1. Naively, one might conclude there is a total of nine options, however, one should note that the case where both Θ and Ξ are absent actually contains two scenarios; the chiral symmetry, $\Pi = \Theta\Xi$, can either be absent or present in this case. This leaves us with a classification of topological phases according to ten symmetry classes (and according to dimensionality), as presented in Table. 1.1.

*That is Hamiltonians of free fermions or of systems which are described within mean-field theory, such as Bardeen Cooper Schrieffer (BCS) superconductors.

Symmetry				d							
	Θ	Ξ	Π	1	2	3	4	5	6	7	8
A	0	0	0	0	$\mathbb{Z}$	0	$\mathbb{Z}$	0	$\mathbb{Z}$	0	$\mathbb{Z}$
AIII	0	0	1	$\mathbb{Z}$	0	$\mathbb{Z}$	0	$\mathbb{Z}$	0	$\mathbb{Z}$	0
AI	1	0	0	0	0	0	$\mathbb{Z}$	0	$\mathbb{Z}_2$	$\mathbb{Z}_2$	$\mathbb{Z}$
BDI	1	1	1	$\mathbb{Z}$	0	0	0	$\mathbb{Z}$	0	$\mathbb{Z}_2$	$\mathbb{Z}_2$
D	0	1	0	$\mathbb{Z}_2$	$\mathbb{Z}$	0	0	0	$\mathbb{Z}$	0	$\mathbb{Z}_2$
DIII	-1	1	1	$\mathbb{Z}_2$	$\mathbb{Z}_2$	$\mathbb{Z}$	0	0	0	$\mathbb{Z}$	0
AII	-1	0	0	0	$\mathbb{Z}_2$	$\mathbb{Z}_2$	$\mathbb{Z}$	0	0	0	$\mathbb{Z}$
CII	-1	-1	1	$\mathbb{Z}$	0	$\mathbb{Z}_2$	$\mathbb{Z}_2$	$\mathbb{Z}$	0	0	0
C	0	-1	0	0	$\mathbb{Z}$	0	$\mathbb{Z}_2$	$\mathbb{Z}_2$	$\mathbb{Z}$	0	0
CI	1	-1	1	0	0	$\mathbb{Z}$	0	$\mathbb{Z}_2$	$\mathbb{Z}_2$	$\mathbb{Z}$	0

Table 1.1: Classification of topological insulators and topological superconductors [6, 7]. Symmetry classes of quadratic Hamiltonians are defined according to time-reversal symmetry, Θ, particles-hole symmetry, Ξ, and the chiral symmetry, $\Pi = \Theta\Xi$. Within a symmetry class, and for a given dimension, d, all gapped Hamiltonians can be divided into equivalence classes which form a group structure. Two Hamiltonians belong to the same equivalence class if and only if they can be smoothly deformed into each other without closing the gap. When the group structure is marked by 0, it means that all gapped Hamiltonians in the symmetry class can be smoothly deformed into each other without closing the gap.

For example, class A in two dimensions ($d = 2$) corresponds to the QHE with a $\mathbb{Z}$ topological invariant (which is the Hall conductance). It has no TRS, no PHS, and no chiral symmetry (by convention, the absence of a symmetry is marked by zero in Table. 1.1). The topological insulator of Kane *et al.* corresponds to symmetry class AII in 2d, with a $\mathbb{Z}_2$ invariant. The value listed under Θ signifies that it squares to -1, as appropriate for a system of spinful electrons. A more mundane example is that of class A in 3d. The corresponding entry contains a zero, signifying that no distinct topological phases exits. Namely, all gapped Hamiltonians in this symmetry class in 3d can be smoothly deformed into each other without closing the gap, and are therefore topologically equivalent.

In the present work we will be mostly interested in symmetry classes D and DIII, in 1d. Both describe superconducting Hamiltonians whose topological phases support zero-energy Majorana bound states (to be defined below). The $\mathbb{Z}_2$ classification corresponds to two distinct phases; with and without Majorana bound states (MBSs). While both classes have a PHS which squares to 1, class DIII contains in addition a TRS which squares to -1. This has the consequence that in class DIII MBSs come in spatially-overlapping degenerate pairs, in accordance with Kramers' theorem. Below we discuss the origin of particle-hole symmetry in superconductors and the conditions for them to be in the topological phase which hosts MBSs. In the rest of the introduction we shall concentrate on class D. Class DIII is covered in chapter 2 in depth.

1.2 Particle-Hole Symmetry of Superconductors

We consider a general mean-field Hamiltonian describing a superconductor,

$$H = \sum_{ij} h_{ij} c_i^\dagger c_j + \Delta_{ij} c_i^\dagger c_j^\dagger + \Delta_{ij}^* c_j c_i, \tag{1.1}$$

where $\{c_i^\dagger\}_{i=1}^N$ creates a fermion in a state labeled by the index i, which can include momentum, spin, atomic orbitals etc. Here, h_{ij} is a hermitian matrix describing the normal part of the Hamiltonian, and Δ_{ij} is an antisymmetric matrix describing pairing of electrons*. Being quadratic in creation and annihilation operators, H can be written in the following form

$$H = \frac{1}{2}\sum_{ij} (c_i^\dagger, c_i) \mathcal{H}_{ij} \begin{pmatrix} c_j \\ c_j^\dagger \end{pmatrix} + \frac{1}{2}\mathrm{Tr}(h) \quad , \quad \mathcal{H}_{ij} = \begin{pmatrix} h_{ij} & \Delta_{ij} \\ \Delta_{ji}^* & -h_{ji} \end{pmatrix}. \tag{1.2}$$

*More precisely, the symmetric part of Δ_{ij} cancels upon summing over i and j due to the anti commutativity of the fermionic operators.

where $\mathcal{H}$ is a $2N \times 2N$ matrix, also known as the Bogoliubov-de Gennes (BdG) Hamiltonian.

By construction, the matrix $\mathcal{H}$ obeys the following anti-unitary particle-hole symmetry

$$\Xi \mathcal{H} \Xi^{-1} = -\mathcal{H} \quad , \quad \Xi = \tau^x \mathcal{K} \tag{1.3}$$

where $\mathcal{K}$ stands for complex conjugation, τ_x is the first Pauli matrix, operating on the particle-hole degree of freedom, and we have used the hermiticity of h and the antisymmetry of Δ. Notice that we did not have to assume anything about H in order to have the symmetry, Ξ; it followed from our construction of $\mathcal{H}$. This means that this symmetry cannot really be broken. This particle-hole symmetry squares to $+1$, namely $\Xi^2 = \tau^x \tau^{x*} = 1$. If no further symmetries apply to $\mathcal{H}$, it therefore belongs to symmetry class D (see Table. 1.1).

It follows from Eq. (1.3) that for each eigenvector, $\phi_i^\nu = (u_i^\nu, v_i^\nu)^{\mathrm{T}}$, of $\mathcal{H}$ with energy ε_ν, there is an eigenvector with energy $-\varepsilon_\nu$, given by

$$(\Xi \phi^\nu)_i = \tau^x \begin{pmatrix} u_i^\nu \\ v_i^\nu \end{pmatrix}^* . \tag{1.4}$$

The eigenvectors of $\mathcal{H}$ are related to the elementary excitations of H through

$$\Gamma_\nu^\dagger = \sum_i (c_i^\dagger, c_i) \begin{pmatrix} u_i^\nu \\ v_i^\nu \end{pmatrix} , \tag{1.5}$$

as one can check that $[H, \Gamma_\nu] = \varepsilon_\nu \Gamma_\nu$. Notice that the hermitian conjugate of Γ_ν is obtained by replacing $\phi_i^\nu = (u_i^\nu, v_i^\nu)^{\mathrm{T}}$ with its particle-hole partner,

$$\Gamma_\nu = \sum_i (c_i^\dagger, c_i) \tau^x \begin{pmatrix} u_i^\nu \\ v_i^\nu \end{pmatrix}^* . \tag{1.6}$$

This signifies that Γ_ν describes an excitation with energy $-\varepsilon_n$. This relation can generally be written as

$$\Gamma_\varepsilon^\dagger = \Gamma_{-\varepsilon} . \tag{1.7}$$

1.3 Search for Majorana Bound States

In 1937 Ettore Majorana hypothesised a fermionic particle whose its own antiparticle [9], later to be known as a *Majorana fermion*. The best candidate among

elementary particles to be a Majorana fermion is the neutrino. Experiments are underway to examine this possibility, by seeking to observe a neutrino-less double β decay [10]. Such a process is only possible if the neutrino is its own antiparticle, namely if creating a neutrino is equivalent to annihilating one, $\gamma = \gamma^\dagger$.

In condensed matter physics, the notion of elementary particles is replaced by that of *elementary excitations* of a system. One can therefore ask whether there can be a system which hosts a fermionic excitation obeying $\gamma = \gamma^\dagger$. From Eq. (1.7) we immediately conclude that such an excitation carries zero energy, $\varepsilon = 0$. This is a manifestation of the fact that creating such a particle is equivalent to destroying it. More generally, this means that it cannot carry any kind of quantum number including energy, charge, spin, etc. Such an excitation is refereed to as a *Majorana zero mode*.

The fact that such an excitation has zero energy has important consequence relating to its robustness. Imagine a system with a single *isolated* excitation γ at zero energy, separated by an energy gap. Let us add a local perturbation to the system and ask whether it is possible that the energy of γ will change from 0 to $\delta\varepsilon$. To comply with PH symmetry, the system must have *another* excitation with energy $-\delta\varepsilon$. However, since by our assumption we started with only a single zero-energy excitation, we conclude this is not possible; an isolated zero-energy excitation is protected from acquiring a finite energy.

The next obvious question is: where to look for such excitations? First, we note that if a bulk energy gap exists, such an excitation can only reside near a defect or at the boundary of a 1d system*. We therefore refer to such an excitation as a Majorana bound state (MBS). Since we are looking for a fermionic excitation which is described by a hermitian operator, $\gamma = \gamma^\dagger$, an immediate candidate would be $\gamma = uc + u^* c^\dagger$, with c being a normal fermionic operator, and u a complex number. This reminds us of the quasiparticle excitations in a BCS superconductor. In a conventional s-wave superconductor, the pairing is between electrons of opposite spin, giving rise to excitations of the form $uc_\uparrow + v^* c_\downarrow^\dagger$, which are not hermitian for any value of u and v. In a spinless superconductor, on the other hand, excitations would generally be of the form $uc + v^* c^\dagger$, which is hermitian if $v = u^*$. To conclude, one should look for MBSs at the boundary of a 1d spinless superconductor.

*Subgap excitations can also reside on the boundary of a 2d or 3d system, however, they would generally form a band and not a *single* excitation separated from the rest by an energy gap.

1.4 The Spinless p-wave Superconductor

Following Kitaev [11], we consider a one dimensional superconductor made out of spinless electrons. The mean-field Hamiltonian describing such a superconductor is given by*

$$\begin{aligned} H_{\mathrm{K}} &= \int \mathrm{d}x \Psi^\dagger(x) \mathcal{H}_{\mathrm{K}}(x) \Psi(x) \quad ; \quad \Psi^\dagger(x) = [\psi^\dagger(x), \psi(x)] \\ \mathcal{H}_{\mathrm{K}}(x) &= \left[-\partial_x^2/2m - \mu(x)\right] \tau^z - i\Delta' \partial_x \tau^y, \end{aligned} \tag{1.8}$$

where $\psi^\dagger(x)$ creates a spinless electron at position x. Notice that under $x \to -x$, the pairing potential acquires a minus sign, namely it has a p-wave symmetry. This property is unavoidable, due to the spinless nature of the electrons in Eq. (1.8). In this respect, the name spinless p-wave superconductor is redundant.

We wish to show that this system hosts a MBS at each of its two ends. First, however, let us obtain the bulk spectrum by considering the system with periodic boundary conditions. By going to Fourier space one obtains

$$\varepsilon_k = \sqrt{(k^2/2m - \mu)^2 + (\Delta' k)^2}. \tag{1.9}$$

where k is the momentum, and where we have taken $\mu(x)$ to be uniform. Note that the system remains gapped except for $\mu = 0$, at which point the gap closes at $k = 0$. Since the existence of a MBS is protected by a gap, it suffices to examine a certain limit of the parameters. One can then vary the parameters away from this limit, without affecting the presence or absence of the MBS, as long as the bulk gap remains open. The phase corresponding to $\mu < 0$ is obviously trivial, namely does not host MBSs. To see this note we can adiabatically deform the Hamiltonian into that of the vacuum, $\Delta' \to 0$, $\mu \to -\infty$, without closing the gap.

To examine the $\mu > 0$ phase, let us create an interface between it and the trivial phase, $\mu < 0$, by letting $\mu(x)$ change its sign at $x = 0$, going from a constant negative value at $x \to -\infty$, to a constant positive value at $x \to \infty$ (see Fig. 1.1). For $\mu(x)$ being small enough we can linearize the spectrum near $k = 0$, which results in the BdG Hamiltonian

$$\mathcal{H}_{\mathrm{K}}(x) = -\mu(x)\tau^z - i\Delta' \partial_x \tau^y. \tag{1.10}$$

We are looking for a zero-energy solution, $\mathcal{H}_{\mathrm{K}} \phi_0(x) = 0$, with $\phi_0(x)$ a two-component spinor in particle-hole space. This is solved by

$$\phi_0(x) = \exp\left[-\frac{1}{\Delta'} \int_0^x \mu(x') \mathrm{d}x' \tau^x\right] \cdot \phi_0(0). \tag{1.11}$$

*In Ref. [11] Kitaev actually considered a lattice version of the model, however, the conclusions remain essentially the same.

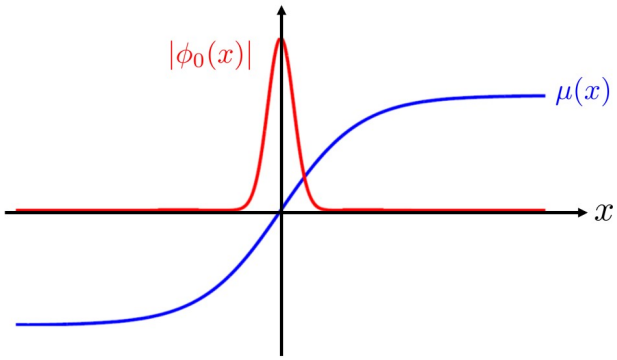

Figure 1.1: A domain wall between the trivial phase and the topological phase of a spinless p-wave superconductor. In blue, the chemical potential, $\mu(x)$, in arbitrary units as a function of position, x. The system is in the trivial phase for $\mu < 0$, and in the topological phase for $\mu > 0$. A zero-energy Majorana bound state (MBS) is localized at the domain wall ($x = 0$). In red, the wave function of the MBS in arbitrary units [see also Eq. (1.12)].

To determined $\phi(0)$ we notice that the integral in the exponent in Eq. (1.11) is positive and diverging for $x \to \pm\infty$. This means that to obtain a non-diverging result, $\phi_0(0)$ must be proportional to the eigenvector of τ^x with eigenvalue $+1$ (we assumed without loss of generality that $\Delta' > 0$), namely

$$\phi_0(x) = \begin{pmatrix} 1 \\ 1 \end{pmatrix} C \exp\left[-\frac{1}{\Delta'}\int_0^x \mu(x')\mathrm{d}x'\right], \tag{1.12}$$

with C being a normalization constant. Notice that as expected, $\phi_0(x)$ is localized near $x = 0$ (see Fig. 1.1), and that the operator creating the bound state,

$$\gamma = \int \Psi^\dagger(x) \cdot \phi_0(x)\mathrm{d}x, \tag{1.13}$$

is hermitian.

Finally, we can relax the constraints which have led to the Hamiltonian of Eq. (1.10). In particular, we are not limited to $\mu(x)$ being small. We can also deform the Hamiltonian in the half space $x < 0$ to the vacuum, thereby obtaining a system with open boundary conditions. Since the bulk gap did not close in the process, the MBS remains bound to the interface.

1.5 Proximity-Coupled Semiconductor Nanowires

Above we saw that a spinless superconductor can be in a topological superconducting phase, with MBSs. In practice, however, electrons have spin, and so it is not immediately obvious that Kitaev's spinless superconductor can be realized in an actual system. Fortunately, it has been shown that electronic systems can effectively behave as spinless superconductor (namely a topological superconductor), thanks to a combination of Zeeman splitting, spin-orbit coupling, and proximity-induced superconductivity [12–16]. We shall review briefly the proposal for realization of topological superconductivity in semiconductor nanowires [15, 16].

Consider a 1d semiconductor nanowire having Rashba spin-orbit coupling (SOC), coupled to a conventional superconductor, and in an external magnetic field. If the magnetic field is applied in the direction of the wire (the x direction) and the surface of the superconductor is parallel to the (xy) plane, then the Hamiltonian for the system is given by

$$\begin{aligned} H_{\rm nw} &= \int \mathrm{d}x \Psi^\dagger(x) \mathcal{H}_{\rm nw}(x) \Psi(x) \quad ; \quad \Psi^\dagger(x) = [\psi_\uparrow^\dagger(x), \psi_\downarrow^\dagger(x), \psi_\downarrow(x), -\psi_\uparrow(x)] \\ \mathcal{H}_{\rm nw}(x) &= \left(\frac{-\partial_x^2}{2m^*} - \mu \right) \tau^z + i\lambda_{\rm R} \partial_x \tau^z \sigma^y - E_{\rm Z} \sigma^x + \Delta \tau^x, \end{aligned} \tag{1.14}$$

where $\{\sigma^\alpha\}_{\alpha=x,y,z}$ and $\{\tau^\alpha\}_{\alpha=x,y,z}$ are sets of Pauli matrices operating on the spin and particle-hole degrees of freedom, respectively. Here, m^* is the effective electron mass, $\lambda_{\rm R}$ is the Rashba SOC constant, E_Z is the Zeeman coupling due to the applied magnetic field, and $\Delta_{\rm ind}$ is the induced pairing potential as a result of the superconducting proximity effect. Notice we have chosen here a basis for the BdG Hamiltonian which is different than one in Eq. (1.2). Here, $\Psi^\dagger(x)$ is defined such that the holes are acted on with a time-reversal operation*, $[\psi_\uparrow(x), \psi_\downarrow(x)] \to [\psi_\downarrow(x), -\psi_\uparrow(x)]$. In this basis particle-hole symmetry is represented by $\Xi = \tau^y \sigma^y \mathcal{K}$.

To see how this model can emulate the Kitaev spinless superconductor of Eq. (1.8), let us consider gradually the ingredients in Eq. (1.14), namely Zeeman splitting, SOC, and superconductivity. In the absence of these, the spectrum of the wire is given by a spin-degenerate parabolic dispersion [see Fig. 1.2(a)]. Upon applying magnetic field, the two spin bands are split due to the Zeeman coupling as shown in Fig. 1.2(b). If the chemical potential lies in the range $-E_{\rm Z} < \mu < E_{\rm Z}$, than the Fermi level is no longer spin degenerate. Close to the Fermi level, the electrons thus behave effectively spinless. The problem, however, is that using proximity to a conventional s-wave superconductor, one cannot induce pairing between electrons

*This basis has the advantage that SU(2) spin rotations are represented by $\exp[i\boldsymbol{\theta}\boldsymbol{\sigma}/2]$, just like in the non BdG case.

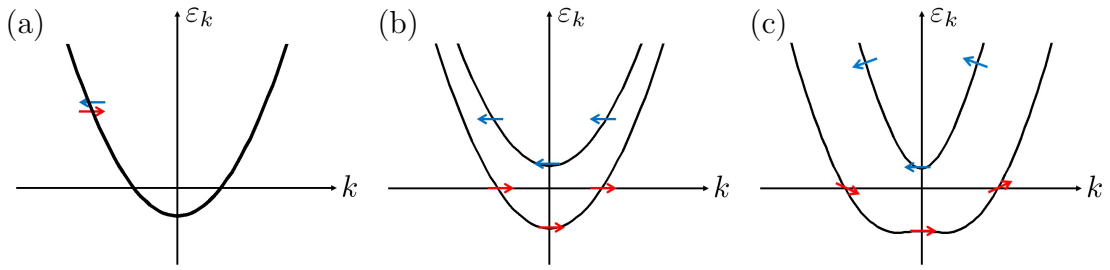

Figure 1.2: Spectrum of the Hamiltonian in Eq. (1.14) before the consideration of induced superconductivity. (a) In the absence of magnetic field, $E_{\rm Z} = 0$, and of spin-orbit coupling, $\lambda_{\rm R} = 0$, the spectrum is doubly degenerate due to spin-rotation symmetry. (b) Applying a magnetic field, $E_{\rm Z} \neq 0$, causes the spectrum to split into two opposite-spin bands due to Zeeman coupling. (c) Upon considering spin-orbit coupling, $\lambda_{\rm R} \neq 0$, the states on the Fermi level in a given band acquire an anti-aligned spin component. This then enables pairing of electrons in a single nondegenerate band by induced superconductivity from a conventional s-wave superconductor. Namely, near the Fermi level the system behaves as a spinless superconductor which was shown to be topological (see Sec. 1.4).

of the same spin. This is where the SOC comes into play. Upon considering the effect of SOC, the spins of the electrons at the two Fermi points are no longer perfectly aligned, but rather have a component which is anti-aligned in the y direction [see Fig. 1.2(c)]. Finally, considering induced superconductivity, $\Delta_{\rm ind}$ pairs electrons within a single band. If $\Delta_{\rm ind}$ is small compared with the splitting between the bands, we can project out the upper band and remain with a single nondegenerate band, realizing an effective spinless superconductor. When the system has open boundary conditions, two MBSs therefore appear; one at each end of the system.

We can now go beyond the limit of small $\Delta_{\rm ind}$. As long as the bulk gap does not closes the system is in the topological phase with MBSs. We can obtain the bulk energy spectrum of the system by Fourier transforming $\mathcal{H}_{\rm nw}(x)$ and squaring it twice,

$$\begin{aligned}\varepsilon_k^2 =& E_{\rm Z}^2 + \Delta_{\rm ind}^2 + (k^2/2m^* - \mu)^2 + (\lambda_{\rm R} k)^2 \\ & \pm 2\sqrt{E_{\rm Z}^2\Delta_{\rm ind}^2 + [E_{\rm Z}^2 + (\lambda_{\rm R}k)^2](k^2/2m^* - \mu)^2}.\end{aligned} \tag{1.15}$$

Assuming $\Delta_{\rm ind}, \lambda_{\rm R} \neq 0$, the gap remains open except for $E_{\rm Z}^2 = \Delta_{\rm ind}^2 + \mu^2$, at which point the gap closes at momentum $k = 0$. One therefore concludes [15, 16] that the system is topological for $E_{\rm Z}^2 > \Delta_{\rm ind}^2 + \mu^2$, and trivial for $E_{\rm Z}^2 < \Delta_{\rm ind}^2 + \mu^2$.

Figure 1.3: Andreev reflection of an electron into a hole at the interface between a normal-metal lead and a superconductor. When the superconductor is a topological superconductor, electrons (or holes) at the Fermi level experience perfect Andreev reflection.

1.6 Majorana-Induced Perfect Andreev Reflection

The presence of a MBS at the end of a superconductor has important consequences when probing the system using transport measurements. Consider attaching a normal-metal lead to a topological superconductor. Electrons approaching the interface from the lead can experience an Andreev reflection [17]; a process in which an electron is reflected as a hole, as depicted in Fig. 1.3. We shall now demonstrate that if the superconductor is a topological superconductor, then electrons at the Fermi level are Andreev reflected with unit probability [18–21], regardless of details such as quality of the interface or presence of a barrier.

The reflection matrix, $r_{\rm NS}(\varepsilon)$, relates the incoming and outgoing modes in the lead with energy ε relative to the Fermi level,

$$\begin{bmatrix}\phi^{\rm e}_{\rm out}(\varepsilon)\\ \phi^{\rm h}_{\rm out}(\varepsilon)\end{bmatrix} = r_{\rm NS}(\varepsilon)\begin{bmatrix}\phi^{\rm e}_{\rm in}(\varepsilon)\\ \phi^{\rm h}_{\rm in}(\varepsilon)\end{bmatrix} \quad ; \quad r_{\rm NS}(\varepsilon) = \begin{bmatrix}r^{\rm ee}(\varepsilon) & r^{\rm eh}(\varepsilon)\\ r^{\rm he}(\varepsilon) & r^{\rm hh}(\varepsilon)\end{bmatrix}. \tag{1.16}$$

At energies inside the superconducting gap there is no transmission into the superconductor, only reflection. Conservation of quasiparticles current then dictates that the reflection matrix unitary, $r^{\dagger}_{\rm NS}(\varepsilon)r_{\rm NS}(\varepsilon) = 1$. Let us now see how particle-hole symmetry is manifested in the reflection matrix. For each solution with energy ε, there is a solution with energy $-\varepsilon$, related by particle-hole symmetry, namely

$$\tau^x\begin{bmatrix}\phi^{\rm e}_{\rm out}(\varepsilon)\\ \phi^{\rm h}_{\rm out}(\varepsilon)\end{bmatrix}^* = r_{\rm NS}(-\varepsilon)\tau^x\begin{bmatrix}\phi^{\rm e}_{\rm in}(\varepsilon)\\ \phi^{\rm h}_{\rm in}(\varepsilon)\end{bmatrix}^*. \tag{1.17}$$

Operating on both sides with $\tau^x\mathcal{K}$ and comparing with Eq. (1.16) results in the

$$\tau^x r^*_{\rm NS}(-\varepsilon)\tau^x = r_{\rm NS}(\varepsilon). \tag{1.18}$$

At zero energy, Eq. (1.18) dictates that $r^{\rm ee}(0) = r^{\rm hh*}(0)$; $r^{\rm he}(0) = r^{\rm eh*}(0)$. In the spinless case that we consider here, $r_{\rm NS}(0)$ is a 2×2 matrix. The unitarity of

$r_{\rm NS}(0)$ then reduces to $|r^{\rm ee}(0)|^2 + |r^{\rm he}(0)|^2 = 1$, $r^{\rm ee}(0)r^{\rm he}(0) = 0$. The matrix $r_{\rm NS}(0)$ is therefore restricted to have one of two forms:

$$r_{\rm NS}(0) = \begin{bmatrix} e^{i\alpha} & 0 \\ 0 & e^{-i\alpha} \end{bmatrix} \quad \text{or} \quad r_{\rm NS}(0) = \begin{bmatrix} 0 & e^{i\beta} \\ e^{-i\beta} & 0 \end{bmatrix}, \tag{1.19}$$

namely, either perfect normal reflection or perfect Andreev reflection. These two options correspond to two topologically-distinct cases*. Indeed, one cannot go smoothly between these matrices without closing the bulk gap of the superconductor†.

As in Sec. 1.4, this means that it suffices to calculate $r_{\rm NS}(0)$ at a certain limit. Focusing again on the spinless superconductor, Eq. (1.8), we consider the limit $\mu \gg \Delta'^2/m$, corresponding to the Fermi level being far from the bottom of the band. Furthermore, let us consider the clean limit of a smooth interface between the lead and the superconductor. Since normal reflection involves having a large momentum transfer $k_{\rm F} \to -k_{\rm F}$, while Andreev reflection has a zero momentum transfer, it is clear that in this limit there is only Andreev reflection. This in itself is not special; this happens also in a conventional (spinful) superconductor. What special is the fact that we can now add a barrier, or vary μ, Δ', and m (without closing the gap), and the perfect Andreev reflection would survive. In the trivial phase ($\mu < 0$), on the other hand, electrons and holes experience perfect normal reflection. To see this, we start from the limit, $\Delta' = 0$, where it is clear that only normal reflection is possible. We can now turn on Δ', however, as long a the gap is open the perfect normal reflection survives due to the constraint of Eq. (1.19).

The perfect Andreev reflection in the topological phase has a signature in the differential conductance at zero bias voltage. At zero temperature, the latter is related to the reflection matrix through [23, 24]

$$G(V) = \frac{e^2}{h}\left[1 - |r^{\rm ee}(eV)|^2 + |r^{\rm he}(eV)|^2\right] = \frac{2e^2}{h}|r^{\rm he}(eV)|^2, \tag{1.20}$$

where in the last step we have used the unitarity of $r_{\rm NS}$. The differential conductance $G(V)$ is therefore expected to have a peak at zero bias voltage, quantized to $2e^2/h$. Note, however, that at finite temperatures $G(0)$ gets contribution also from electrons at nonzero energies (namely above or below the Fermi level), and therefore the perfect quantization is lost. Recently, the zero-bias conductance peak has been

*This topological distinction between two forms of the reflection matrix can be generalized to the case of a multi-channel wire [22].

†When the gap of the superconductor closes, transmission trough the superconductor is possible, in which case the reflection matrix is no longer unitary, allowing for a smooth deformation between the two matrices in Eq. (1.19).

observed in proximity-coupled semiconductor wires [25–29], in agreement with the prediction that this system supports a topologically superconducting phase.

Chapter 2

Time-Reversal Invariant Topological Superconductivity

2.1 Introduction

Topological phases in condensed matter are generally characterized by having unique surface properties which are dictated by the topological properties of the bulk. The first and most famous example is the quantum Hall effect (QHE) [1–3], in which gapless chiral edge modes, protected only by topology, reside on the edges of a two-dimensional system and give rise to a quantized Hall conductivity.

Since then it has been realized that upon invoking symmetries, a rich variety of topological phases can emerge [6, 7, 30]. These phases also contain gapless surface states which are related to the topological nature of the bulk, however, they are only protected in the presence of some imposed symmetries, and could otherwise become gapped. Here, the paradigmatic example is the topological insulator (TI) [5, 31, 32] which in two dimensions can be thought of as two copies of the QHE, related by time-reversal. The edge of the system now host gapless *helical* modes which are protected by the presence of time-reversal symmetry (TRS).

The various topological phases are classified according to the possible symmetries present in a given system [6, 7]. These are TRS, particle-hole symmetry (PHS) and chiral symmetry [33]. Of particular interest is the so-called class-D topological superconductor (TSC) [22, 34] which is protected solely by PHS. This symmetry is special since it exists in all superconducting systems, and in fact cannot truly be broken. This makes its edge states, the Majorana modes, extremely robust. In that sense, the TSC can be viewed as the superconducting analog of the QHE.

One is then prompted to ask: what is the superconducting analog of the topological insulator? This would be the time-reversal invariant topological superconductor

(TRITOPS) which belongs to class DIII [35, 36]. In one or two dimensions, it can be described as two copies of a class D TSC, related by time-reversal transformation. Each edge (or end) of this phase hosts a Kramers' pair of time-reversal related Majorana modes, analogous to the pair of helical edge modes of the two-dimensional (2d) TI. Unlike single Majorana zero modes, Majorana Kramers' pairs do not have a well defined braiding statistics [37, 38]; however, they have non-trivial spin structure [39, 40].

Experimentally realizing the TRITOPS phase is a major outstanding challenge in the study of topological phases in condensed matter. To this date, however, attempts have been focused on realizing the class D TSC. An important breakthrough in this context was the understanding that one can realize class D TSC using a combination of spin-orbit coupling and proximity to an s-wave superconductor, in a system of noninteracting electrons [12–16, 41]. This prediction lead to a series of experiments showing evidence consistent with the presence of Majorana bound states [25–29, 42–44].

The goal of the study presented in this chapter is to construct experimentally-realizable models for a time-reversal invariant topological superconductor in class DIII in one dimension. We begin in Sec. 2.2 by showing [45] that unlike in class D, the topological phase of class DIII cannot be realized using proximity of an s-wave superconductor to a system of noninteracting electrons. Namely electron-electron interaction are essential for realizing the TRITOPS phase. In Sec. 2.3 we consider a minimal low-energy model for a proximity-coupled system in the presence of repulsive interactions. We show how short-ranged repulsive interactions can drive this model into its topologically non-trivial phase [46] by effectively suppressing singlet pairing, while strengthening triplet pairing. In Sec. 2.4 we suggest two microscopic models and show they are described at low energies by the minimal model. These are (i) a narrow 2d TI partially covered by an s-wave SC [see Fig. 2.6(a)], and (ii) a quasi 1d semiconductor nanowire proximitized by an s-wave SC [see Fig. 2.7(a)]. Finally, in Sec. 2.5 we numerically simulate the proximitized nanowire system [47]. By employing numerical Hartree-Fock calculations as well as a Density Matrix Renormalization (DMRG) analysis, we show that in a certain parameters range the system indeed enters the TRITOPS phase.

2.2 Necessity of Interactions

In this section we prove that, unlike in class D, the topological phase of class DIII cannot be realized using proximity of a conventional s-wave superconductor to a system of noninteracting electrons. This suggests that to realize the TRITOPS phase

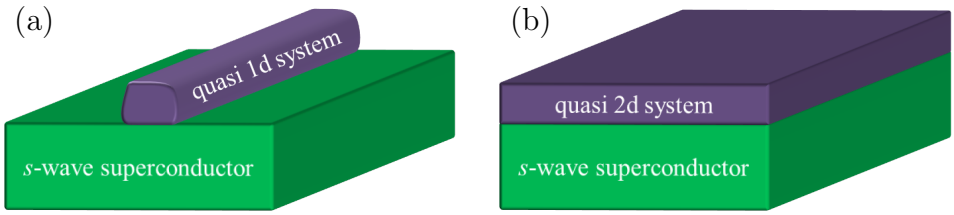

Figure 2.1: The considered physical setups. (a) A quasi one-dimensional system (referred to as wire) in proximity to a conventional s-wave superconductor. As long as there are no interactions between the electrons in the wire, the system will never be in the topological phase of class DIII. (b) This statement can be extended to the case of a quasi two-dimensional system.

one should consider interactions between the electrons [46–52], or use proximity to unconventional superconductors [53–55]. One can also use *two* s-wave superconductors with a phase difference between them which is tuned to π [39, 56, 57]. In 2d and 3d, intrinsic TRITOPS have been proposed [58–62]*, which do not involve the proximity effect†.

We start by writing the model, consisting of both the parent superconductor and the system as depicted in Fig. 2.1(a). We integrate out the superconductor's degrees of freedom and obtain the Green's function of the system alone. Next we construct the $\mathbb{Z}_2$ topological invariant for a general class-DIII system in 1d, and show that this invariant always takes its trivial value. We then extend this result to the case of a 2d proximitized system [see Fig. 2.1(b)]. Finally, we generalize the proof to include also non translationally-invariant systems.

2.2.1 The model

We consider a quasi–1d system (hereafter referred to as a "wire") of noninteracting electrons, coupled to a bulk superconductor (SC). The Hamiltonian describing the

*Similarly to intrinsic TRITOPS, the He-3 B phase is an example of a time-reversal invariant topological *superfluid* [63].

†In 1d proximity coupling is necessary in order to have a gapped spectrum. Gapless TSC in 1d have also been suggested [40].

combined system reads

$$\begin{aligned} H &= H_{\rm w} + H_{\rm sc} + H_{\rm c}, \\ H_{\rm w} &= \sum_k \psi_k^\dagger h_k^{\rm w} \psi_k, \\ H_{\rm sc} &= \sum_k \left[\eta_k^\dagger h_k^{\rm sc} \eta_k + \frac{1}{2}(\eta_k^\dagger \Delta_k \eta_{-k}^{\dagger {\rm T}} + {\rm h.c.}) \right], \\ H_{\rm c} &= \sum_k (\eta_k^\dagger t_k \psi_k + {\rm h.c.}), \end{aligned} \tag{2.1}$$

where k is the momentum along the wire's axis. $H_{\rm w}$ and $H_{\rm sc}$ are the Hamiltonians describing the wire and the SC, respectively, and $H_{\rm c}$ describes the coupling between them. For every k, $\psi_k^\dagger$ and $\eta_k^\dagger$ are row vectors of fermionic creation operators of states in the wire and the superconductor, respectively. These states include all degrees of freedom within a unit cell including spin, transverse modes, sublattice sites, atomic orbitals etc. Correspondingly, $h_k^{\rm w}$, $h_k^{\rm sc}$, Δ_k, and t_k are matrices operating on these internal degrees of freedom. In writing Eq. (2.1) we have assumed that the interactions in the SC are adequately described within mean-field theory through the pairing potential matrix, Δ_k*. Due to fermionic statistics one can, without loss of generality, take the pairing matrix to obey $\Delta_{-k}^{\rm T} = -\Delta_k$, where the superscript stands for the transpose of a matrix. In Eq. (2.1), we have assumed that the system is translationally invariant; however, below we argue that our conclusions hold even in non-translationally invariant systems, e.g., in the presence of disorder.

Here, we consider systems which belong to symmetry class DIII. The Hamiltonian H has TRS that squares to -1. The application of such a time-reversal operation most generally reads

$$\mathbb{T}\psi_k\mathbb{T}^{-1} = \mathcal{T}_{\rm w}\psi_{-k} \quad ; \quad \mathbb{T}\eta_k\mathbb{T}^{-1} = \mathcal{T}_{\rm sc}\eta_{-k} \quad ; \quad \mathbb{T}i\mathbb{T}^{-1} = -i, \tag{2.2}$$

where $\mathcal{T}_{\rm w}$ and $\mathcal{T}_{\rm sc}$ are unitary matrices operating in the spaces of states in the wire and the superconductor, respectively, and which furthermore obey $\mathcal{T}_{\rm w(sc)}\mathcal{T}_{\rm w(sc)}^* = -1$. The last property is what distinguishes systems in class DIII from systems in class BDI [64, 65] in which TRS squares to 1. Enforcing TRS on the system, $\mathbb{T}H\mathbb{T}^{-1} = H$, amounts to the following conditions

$$\mathcal{T}_{\rm w}^\dagger h_{-k}^{\rm w*}\mathcal{T}_{\rm w} = h_k^{\rm w} \quad ; \quad \mathcal{T}_{\rm sc}^\dagger h_{-k}^{\rm sc*}\mathcal{T}_{\rm sc} = h_k^{\rm sc} \quad ; \quad \mathcal{T}_{\rm sc}^\dagger t_{-k}^*\mathcal{T}_{\rm w} = t_k \quad ; \quad \mathcal{T}_{\rm sc}^\dagger \Delta_{-k}^*\mathcal{T}_{\rm sc}^* = \Delta_k. \tag{2.3}$$

*The reverse proximity effect in the SC may reduce Δ_k near the interface with the wire, compared to the bulk value. This effect should be small when the density of states in the SC (within a coherence length away from the interface) is large compared to the density of states in the wire, or alternatively, when the coupling to the wire is weak.

The last equality, together with the property $\Delta_{-k}^{\mathrm{T}} = -\Delta_k$, guarantee that $\Delta_k \mathcal{T}_{\mathrm{sc}}$ is a Hermitian matrix.

In this work, we focus on the case where the pairing potential of the parent superconductor satisfies that $\Delta_k \mathcal{T}_{\mathrm{sc}}$ is a positive semi-definite (PSD) matrix*. Namely $\langle u|\Delta_k \mathcal{T}_{\mathrm{sc}}|u\rangle \geq 0$ for all vectors $|u\rangle$, and all momenta k. In particular, this includes for example the case of a *conventional s-wave superconductor*, in which the order parameter has a uniform phase on all the bands (and no interband pairing). Note also that this condition excludes both the case considered in Ref. [54], where the superconductor has an $s_\pm$ order parameter with a relative π phase between different bands, and the case of Refs. [39, 56], where there are two superconducting leads that form a π junction.

The simplest example of a time reversal invariant superconductor with a positive semi-definite $\Delta_k \mathcal{T}_{\mathrm{sc}}$ is a single band s-wave superconductor, whose pairing potential is

$$(\Delta_k)_{\boldsymbol{k}_{\mathrm{T}},s;\boldsymbol{k}'_{\mathrm{T}},s'} = \Delta_0 i\sigma^y_{ss'}\delta_{\boldsymbol{k}_{\mathrm{T}},-\boldsymbol{k}'_{\mathrm{T}}}, \tag{2.4}$$

where $\{\sigma^\alpha\}_{\alpha=x,y,z}$ is the set of pauli matrices operating in spin space, $\boldsymbol{k}_{\mathrm{T}}$ labels the transverse momenta of states in the superconductor, and Δ_0 is a number which we can choose to be real and positive. The time-reversal matrix is given in this example by $(\mathcal{T}_{\mathrm{sc}})_{\boldsymbol{k}_{\mathrm{T}},s;\boldsymbol{k}'_{\mathrm{T}},s'} = -i\sigma^y_{ss'}\delta_{\boldsymbol{k}_{\mathrm{T}},-\boldsymbol{k}'_{\mathrm{T}}}$, which indeed results in $\Delta_k \mathcal{T}_{\mathrm{sc}} = \Delta_0$ being a PSD matrix. In what follows we will not limit ourselves to the example of Eq. (2.4), but rather consider the most general matrix Δ_k for which $\Delta_k \mathcal{T}_{\mathrm{sc}}$ is PSD. Our results thus apply to a wide class of parent superconductors, for instance a multiple band superconductor with spin-orbit coupling.

Below we prove that as long as $\Delta_k \mathcal{T}_{\mathrm{sc}}$ is PSD, the wire is in the topologically-trivial phase. We do this in two steps. First, we show that upon integrating out the SC, the anomalous part of the zero-frequency self energy is also PSD. Second, we show that, as a result, the $\mathbb{Z}_2$ topological invariant always assumes its trivial value.

2.2.2 Integrating out the superconductor

We wish to obtain the Green's function describing the wire, where the superconducting proximity effect is expressed by an anomalous self-energy term. We start by writing the Hamiltonian in a BdG form

$$H = \frac{1}{2}\sum_k \Psi_k^\dagger \begin{pmatrix} \mathcal{H}_k^{\mathrm{w}} & V_k^\dagger \\ V_k & \mathcal{H}_k^{\mathrm{sc}} \end{pmatrix} \Psi_k, \tag{2.5}$$

*More generally, $\Delta_k \mathcal{T}_{\mathrm{sc}}$ can be a PSD matrix times some complex number that does not depend on k. The phase of this complex number can always be absorbed in the definition of $\mathcal{T}_{\mathrm{sc}}$, rendering $\Delta_k \mathcal{T}_{\mathrm{sc}}$ PSD.

using the Nambu spinor $\Psi_k^\dagger = (\psi_k^\dagger, \psi_{-k}^{\mathrm{T}}\mathcal{T}_{\mathrm{w}}, \eta_k^\dagger, \eta_{-k}^{\mathrm{T}}\mathcal{T}_{\mathrm{sc}})$, where

$$\mathcal{H}_k^{\mathrm{w}} = \tau^z \otimes h_k^{\mathrm{w}}, \tag{2.6a}$$
$$\mathcal{H}_k^{\mathrm{sc}} = \tau^z \otimes h_k^{\mathrm{sc}} + \tau^x \otimes \Delta_k \mathcal{T}_{\mathrm{sc}}, , \tag{2.6b}$$
$$V_k = \tau^z \otimes t_k, \tag{2.6c}$$

and where $\{\tau^\alpha\}_{\alpha=x,y,z}$ are Pauli matrices in particle-hole space. In writing Eqs. (2.5, 2.6), we have used the relations given in Eq. (2.3). The Green's function of the wire, $\mathcal{G}_k^{\mathrm{w}}(\omega)$, is obtained by integrating out the SC,

$$\mathcal{G}_k^{\mathrm{w}}(\omega) = [i\omega - \mathcal{H}_k^{\mathrm{w}} - \Sigma_k(\omega)]^{-1}, \tag{2.7a}$$
$$\Sigma_k(\omega) = V_k^\dagger g_k^{\mathrm{sc}}(\omega) V_k, \tag{2.7b}$$
$$g_k^{\mathrm{sc}}(\omega) = (i\omega - \mathcal{H}_k^{\mathrm{sc}})^{-1}, \tag{2.7c}$$

where $\Sigma_k(\omega)$ is the self energy, and $g_k^{\mathrm{sc}}(\omega)$ is the Green's function of the parent SC in the absence of coupling to the wire.

Using Eqs. (2.6b) and (2.7c), one can check that $g_k^{\mathrm{sc}}(0)$ is Hermitian and obeys $\tau^y g_k^{\mathrm{sc}}(0)\tau^y = -g_k^{\mathrm{sc}}(0)$. It therefore has the following structure:

$$g_k^{\mathrm{sc}}(0) = \tau^z \otimes g_k^{\mathrm{N}} + \tau^x \otimes g_k^{\mathrm{A}}, \tag{2.8}$$

where g_k^{N} and g_k^{A} are Hermitian matrices. This also means that the zero-frequency self energy has the same structure, $\Sigma_k(0) = \tau^z \otimes \Sigma_k^{\mathrm{N}} + \tau^x \otimes \Sigma_k^{\mathrm{A}}$, with $\Sigma_k^{\mathrm{N}} = t_k^\dagger g_k^{\mathrm{N}} t_k$ and $\Sigma_k^{\mathrm{A}} = -t_k^\dagger g_k^{\mathrm{A}} t_k$ being the normal and anomalous parts, respectively. Upon rotating $g_k^{\mathrm{sc}}(0)$ in Eq. (2.7c) by the unitary transformation $\exp(i\pi\tau^x/4)$, and using Eqs. (2.6b) and (2.8), it follows that

$$(\Delta_k \mathcal{T}_{\mathrm{sc}} - i h_k^{\mathrm{sc}})(g_k^{\mathrm{A}} + i g_k^{\mathrm{N}}) = -\mathbb{1}. \tag{2.9}$$

One then arrives at

$$\begin{aligned} &\langle u|\Sigma_k^{\mathrm{A}}|u\rangle = -\langle u|t_k^\dagger g_k^{\mathrm{A}} t_k|u\rangle = -\mathrm{Re}\langle u|t_k^\dagger (g_k^{\mathrm{A}} - i g_k^{\mathrm{N}}) t_k|u\rangle \\ &= \mathrm{Re}\langle u|t_k^\dagger (g_k^{\mathrm{A}} - i g_k^{\mathrm{N}})(\Delta_k \mathcal{T}_{\mathrm{sc}} - i h_k^{\mathrm{sc}})(g_k^{\mathrm{A}} + i g_k^{\mathrm{N}}) t_k|u\rangle \\ &= \mathrm{Re}\langle v|\Delta_k \mathcal{T}_{\mathrm{sc}} - i h_k^{\mathrm{sc}}|v\rangle = \langle v|\Delta_k \mathcal{T}_{\mathrm{sc}}|v\rangle \geq 0, \end{aligned} \tag{2.10}$$

where $|u\rangle$ is an arbitrary vector, $|v\rangle \equiv (g_k^{\mathrm{A}} + i g_k^{\mathrm{N}}) t_k|u\rangle$, and we have used the fact that g_k^{N}, g_k^{A}, and h_k^{sc} are Hermitian. Namely, we have proved that Σ_k^{A} is PSD.

2.2.3 The topological invariant

We now construct the $\mathbb{Z}_2$ topological invariant for a general gapped quasi 1d system in class DIII*. We then apply it to the system under consideration and show that, due to the positivity of Σ_k^{A}, the invariant always assumes its trivial value. We define the effective Hamiltonian of the wire system using its Green's function, $\mathcal{H}_k^{\mathrm{eff}} = -[\mathcal{G}_k^{\mathrm{w}}(0)]^{-1}$. By setting $\omega = 0$ in Eq. (2.7a) one obtains

$$\mathcal{H}_k^{\mathrm{eff}} = \tau^z \otimes (h_k^{\mathrm{w}} + \Sigma_k^N) + \tau^x \otimes \Sigma_k^{\mathrm{A}}, \tag{2.11}$$

where we have used the structure of $\Sigma_k(0)$ as given below Eq. (2.8). This Hamiltonian obeys a time-reversal symmetry, $\mathcal{T}_{\mathrm{w}}^\dagger \mathcal{H}_{-k}^{\mathrm{eff}*} \mathcal{T}_{\mathrm{w}} = \mathcal{H}_k^{\mathrm{eff}}$, as well as a chiral symmetry, $\tau^y \mathcal{H}_k^{\mathrm{eff}} \tau^y = -\mathcal{H}_k^{\mathrm{eff}}$, and is therefore in class DIII.

Written in the basis which diagonalizes the chiral symmetry, the Hamiltonian takes the form

$$e^{i\frac{\pi}{4}\tau^x} \mathcal{H}_k^{\mathrm{eff}} e^{-i\frac{\pi}{4}\tau^x} = \begin{pmatrix} 0 & Q_k \\ Q_k^\dagger & 0 \end{pmatrix}. \tag{2.12}$$

We use the singular value decomposition to write $Q_k = U_k^\dagger D_k V_k$, where U_k, V_k are unitary matrices and D_k is a square diagonal matrix with non-negative elements on its diagonal. By squaring $\mathcal{H}_k^{\mathrm{eff}}$ it becomes apparent that the elements of D_k are the positive eigenvalues of $\mathcal{H}_k^{\mathrm{eff}}$. Since $\mathcal{H}_k^{\mathrm{eff}}$ is gapped, there are no zero elements on the diagonal of D_k, and it is thus positive definite.

We can adiabatically deform D_k to the identity matrix without closing the gap, and therefore without changing the topological invariant. This in turn deforms the Hamiltonian, $\mathcal{H}_k^{\mathrm{eff}} \to \tilde{\mathcal{H}}_k^{\mathrm{eff}}$, such that $\tilde{\mathcal{H}}_k^{\mathrm{eff}}$ has two flat bands at energies ± 1 (in the appropriate units), but the same eigenstates as $\mathcal{H}_k^{\mathrm{eff}}$ (and therefore the same symmetries). $\tilde{\mathcal{H}}_k^{\mathrm{eff}}$ is given by Eq. (2.12) with Q_k replaced by $\tilde{Q}_k = U_k^\dagger V_k$, which is now a unitary matrix. The TRS of $\tilde{\mathcal{H}}_k^{\mathrm{eff}}$ implies that $\mathcal{T}_{\mathrm{w}}^\dagger \tilde{Q}_{-k}^* \mathcal{T}_{\mathrm{w}} = \tilde{Q}_k^\dagger$. Together with the unitarity of $\tilde{Q}_k$ this dictates that for every eigenstate

$$\tilde{Q}_k |\alpha_{n,k}\rangle = e^{i\theta_{n,k}} |\alpha_{n,k}\rangle, \tag{2.13}$$

there is another eigenstate of $\tilde{Q}_k$, $\mathcal{T}_{\mathrm{w}}^\dagger |\alpha_{n,-k}\rangle^*$ with an eigenvalue $\exp(i\theta_{n,-k})$. Thus, at the time-reversal invariant momenta, $k = 0, \pi$, the eigenvalues of $\tilde{Q}_k$ come in Kramers' degenerate pairs.

Considering the spectrum of $\tilde{Q}_k$ as a function of $k \in [-\pi, \pi]$, it follows that the number of pairs of degenerate states at a given value θ cannot change by an

*Alternative approaches for obtaining the class-DIII topological invariant in 1d can be found in Refs. [36, 48, 66–68].

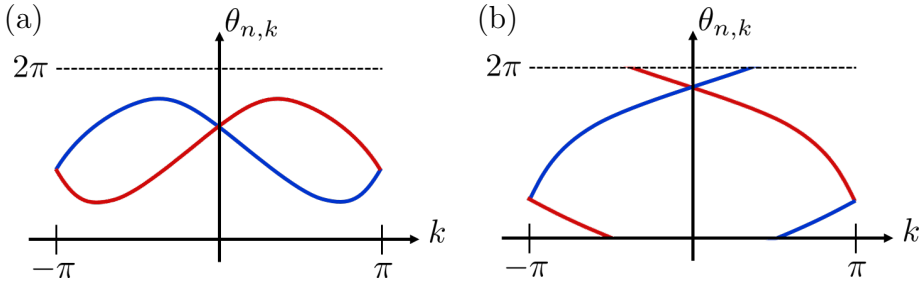

Figure 2.2: Examples of spectra of the unitary matrix $\tilde{Q}_k$ [see Eq. (2.12) and below], corresponding to (a) a topologically trivial case, and (b) a topologically nontrivial case. The eigenvalues of $\tilde{Q}_k$ are phases given by $\{\exp(i\theta_{n,k})\}_n$. Due to time-reversal symmetry the eigenvalues come in pairs, $\theta_{n,k}$ and $\theta_{n,-k}$, corresponding to the blue and red lines, respectively. The parity of the winding number of the blue (or red) line gives the class-DIII topological invariant in 1d. For a noninteracting system in proximity to an s-wave superconductor, the winding number of any angle $\theta_{n,k}$ will always be zero [see Eq. (2.15) and below], rendering such a system topologically trivial.

odd number during an adiabatic change which leaves the gap of $\mathcal{H}_k^{\rm eff}$ open. The parity of the number of degenerate pairs is therefore a topological invariant. Alternatively stated, upon dividing the eigenvalues of $\tilde{Q}_k$ to two groups $\{\exp(i\theta^{\rm I}_{n,k})\}_n$ and $\{\exp(i\theta^{\rm II}_{n,k})\}_n$, related by time reversal, $\theta^{\rm II}_{n,k} = \theta^{\rm I}_{n,-k}$, the topological invariant is given by

$$\nu_{\rm 1d} = (-1)^W \quad ; \quad W = \sum_n \frac{1}{2\pi} \int_{k=-\pi}^{k=\pi} {\rm d}\theta^{\rm I}_{n,k}, \tag{2.14}$$

namely, the parity of the sum of windings of $\{\theta^{\rm I}_{n,k}\}_n$. Figure 2.2 presents examples of trivial and topological spectra of $\tilde{Q}_k$.

Eq. (2.14) is correct for any quasi 1d system in class DIII. Let us now concentrate on the system at hand, namely one which is given by Eq. (2.1), with $\Delta_k \mathcal{T}_{\rm sc}$ being PSD. Inserting Eq. (2.11) in Eq. (2.12), one arrives at $Q_k = \Sigma^{\rm A}_k - i(h^{\rm w}_k + \Sigma^{\rm N}_k)$. From the positivity of $\Sigma^{\rm A}_k$, derived in Eq. (2.10), and the fact that $h^{\rm w}_k$ and $\Sigma^{\rm N}_k$ are Hermitian, it follows that

$$\begin{aligned} 0 \leq & \langle \alpha_{n,k} | \Sigma^{\rm A}_k | \alpha_{n,k} \rangle = {\rm Re} \langle \alpha_{n,k} | Q_k | \alpha_{n,k} \rangle = {\rm Re} \langle \alpha_{n,k} | U_k^\dagger D_k V_k | \alpha_{n,k} \rangle \\ = & {\rm Re} \langle \alpha_{n,k} | \tilde{Q}_k V_k^\dagger D_k V_k | \alpha_{n,k} \rangle = 2 \cos\theta_{n,k} \cdot \langle V_k \alpha_{n,k} | D_k | V_k \alpha_{n,k} \rangle, \end{aligned} \tag{2.15}$$

and since D_k is positive definite, we conclude that $\cos\theta_{n,k} \geq 0$ for all n and k. Namely none of the phases $\theta_{n,k}$ can have a non-zero winding number as k changes

from $-\pi$ to π, which in particular means that the topological invariant, Eq. (2.14), is always trivial, $\nu_{1\mathrm{d}} = 1$.

2.2.4 Two dimensions

We wish to generalize our result to the case of a 2d system in proximity to a bulk superconductor, as depicted in Fig. 2.1(b). The combined system is described by the Hamiltonian of Eq. (2.1), with $k \to \boldsymbol{k} = (k_x, k_y)$. All the above results, excluding Eq. (2.14), are still valid in the 2d case under this substitution. The $\mathbb{Z}_2$ two-dimensional topological invariant can be obtained from the 1d invariant by*

$$\nu_{2\mathrm{d}} = \nu_{1\mathrm{d}}[\mathcal{H}^{\mathrm{eff}}_{k_x=0,k_y}] \cdot \nu_{1\mathrm{d}}[\mathcal{H}^{\mathrm{eff}}_{k_x=\pi,k_y}]. \tag{2.16}$$

Before proving Eq. (2.16), let us first draw from it our main conclusion. The Hamiltonians $\mathcal{H}^{\mathrm{eff}}_{k_x=0,k_y}$ and $\mathcal{H}^{\mathrm{eff}}_{k_x=\pi,k_y}$ both belong to class DIII in 1d, and are of the form of Eq. (2.11) with a PSD anomalous part. Consequently, as we proved above, both $\mathcal{H}^{\mathrm{eff}}_{k_x=0,k_y}$ and $\mathcal{H}^{\mathrm{eff}}_{k_x=\pi,k_y}$ are topologically trivial. From Eq. (2.16) it then follows that the 2d Hamiltonian $\mathcal{H}^{\mathrm{eff}}_{k_x,k_y}$ is trivial as well†.

We now argue that the two-dimensional topological invariant in class DIII is given by Eq. (2.16). This is most readily seen by considering a semi-infinite system with periodic boundary conditions in the x direction, and an edge along the line $y = 0$. The non-trivial phase is characterized by having an odd number of helical edge modes. At the edge of such system, at every energy inside the bulk gap, there must be an odd number of Kramers' pairs of edge states, similarly to the case of the two-dimensional topological insulator [5, 69]. Let us focus on $E = 0$ (which is in the middle of the gap, due to particle-hole symmetry). At $k_x = 0$, the number of Kramers' pairs is equal to the $\mathbb{Z}_2$ invariant of the corresponding DIII one-dimensional Hamiltonian $\mathcal{H}^{\mathrm{eff}}_{k_x=0,k_y}$. The same is true at the other time reversal invariant momentum, $k_x = \pi$. Due to time reversal and chiral symmetries, the number of zero energy Kramers' pairs at momenta away from $k_x = 0, \pi$ must be even. Therefore, the parity of the total number of Kramers' pairs at $E = 0$ is equal to $\nu_{1\mathrm{d}}[\mathcal{H}^{\mathrm{eff}}_{k_x=0,k_y}] \cdot \nu_{1\mathrm{d}}[\mathcal{H}^{\mathrm{eff}}_{k_x=\pi,k_y}]$, which is the right hand side of Eq. (2.16).

*Note that most generally k_x and k_y should be considered as coordinates along the reciprocal primitive vectors, $\boldsymbol{G}_{1,2}$, in units of $|\boldsymbol{G}_{1,2}|/2\pi$, respectively.

†We note that since *both* $\mathcal{H}^{\mathrm{eff}}_{k_x=0,k_y}$ and $\mathcal{H}^{\mathrm{eff}}_{k_x=\pi,k_y}$ (and similarly $\mathcal{H}^{\mathrm{eff}}_{k_x,k_y=0}$ and $\mathcal{H}^{\mathrm{eff}}_{k_x,k_y=\pi}$) are trivial, the weak topological indices are trivial as well.

2.2.5 Extension to non-translationally invariant systems

So far, we assumed that the system is translationally invariant along the direction of the wire in the 1d case, or in the plane of the system in the 2d case [Figs. 2.1(a) and 2.1(b), respectively]. However, our results holds even without translational symmetry, e.g., in the presence of disorder.

To see this, consider a disordered system in either 1d or 2d, coupled to a superconductor. Imagine a disorder realization which is periodic in space, with a period that is much larger than any microscopic length scale (in particular, the induced superconducting coherence length). By the arguments presented in the preceding sections, the resulting translationally invariant system is topologically trivial. Hence, at its boundary there are no topologically non-trivial edge states. Since the size of the unit cell is much larger than the coherence length, the periodicity of the system cannot matter for the existence or the lack of edge states. Therefore, a *single* unit cell corresponds to a finite disordered system, which (as its size tends to infinity) is in the topologically trivial phase, as well.

2.3 Low-Energy Theory

Above we have shown that the TRITOPS phase cannot arise in a noninteracting system coupled to a conventional superconductor. We are therefore prompted to investigate the effect of electron-electron interactions in the proximitized system. In this section we consider a general "minimal" model (see Fig. 2.3) which can arise as a low-energy theory of various spin-orbit coupled 1d systems in proximity to an s-wave SC. The model has four Fermi points with two right moving modes and two left-moving modes. Due to spin-orbit coupling, proximity-induced superconductivity results in both a singlet and a triplet pairing potential, Δ_{s} and Δ_{t}, respectively. As we now show, short-range repulsive interactions suppress Δ_{s} with compare to Δ_{t}, thereby driving the system into the topological phase. We map the phase diagram of this minimal model using both a mean-field approximation and an analytically controlled renormalization group (RG) analysis.

While we consider clean systems in this work, we expect our results to hold also for systems with weak disorder. Namely, we expect the topological phase to survive as long as the mean free time associated with disorder is large compared to the inverse energy gap, similar to the case of the class D topological SC [70, 71].

Our minimal model is described in the absence of interactions by the following

Hamiltonian

$$\begin{aligned} H &= H_0 + H_\Delta, \\ H_0 &= -i \int \mathrm{d}x \left\{ v_+ \left[R_\uparrow^\dagger(x) \partial_x R_\uparrow(x) - L_\downarrow^\dagger(x) \partial_x L_\downarrow(x) \right] \right. \\ &\qquad \left. + v_- \left[R_\downarrow^\dagger(x) \partial_x R_\downarrow(x) - L_\uparrow^\dagger(x) \partial_x L_\uparrow(x) \right] \right\}, \\ H_\Delta &= \int \mathrm{d}x \left[\Delta_+ R_\uparrow^\dagger(x) L_\downarrow^\dagger(x) + \Delta_- L_\uparrow^\dagger(x) R_\downarrow^\dagger(x) + \mathrm{h.c.} \right], \end{aligned} \tag{2.17}$$

where R_s (L_s) is an annihilation operator of a right (left) moving fermionic mode of spin s. Here, Δ_+ and Δ_- are two induced pairing potentials. Δ_+ describes pairing between the modes of positive helicity, $R_\uparrow$ and $L_\downarrow$, while Δ_- describes pairing between the modes of negative helicity, $L_\uparrow$ and $R_\downarrow$*. Similarly, $v_\pm$ are the velocities of the modes with positive and negative helicity, respectively. The dispersion of H_0 is shown in Fig. 2.3.

The time-reversal operation is defined by†

$$\mathbb{T} R_s(x) \mathbb{T}^{-1} = i\sigma^y_{ss'} L_{s'}(x) \quad ; \quad \mathbb{T} L_s(x) \mathbb{T}^{-1} = i\sigma^y_{ss'} R_{s'}(x) \quad ; \quad \mathbb{T} i \mathbb{T}^{-1} = -i, \tag{2.18}$$

where $\{\sigma^i\}_{i=x,y,z}$ is the set of Pauli matrices operating in spin space. Requiring that H obeys time-reversal symmetry, $\mathbb{T} H \mathbb{T}^{-1} = H$, imposes the constraints that both Δ_+ and Δ_- are real. In the absence of inversion symmetry, the Fermi momenta k_F^+ and k_F^- generally differ from one another (see Fig. 2.3). In this case, H is the most general low-energy quadratic Hamiltonian which describes a single-channel 1d system with TRS‡.

The time-reversal operation in Eq. (2.18) squares to -1, placing this system in class DIII of the Altland-Zirnbauer classification [33], with a $\mathbb{Z}_2$ topological invariant [6, 7]. By applying the result of Sec. 2.2.3 to the model of Eq. (2.17), it can be shown that the topological invariant is determined by the product of the signs of the pairing potentials at the Fermi points§,

$$\nu = \mathrm{sgn}(\Delta_+) \cdot \mathrm{sgn}(\Delta_-), \tag{2.19}$$

*It should be noted that the identification of the index $s = \uparrow, \downarrow$ as the spin is not crucial. One can instead consider any two modes $R_1(x)$, $R_2(x)$ and their time-reversal partners $L_2(x)$, $L_1(x)$, respectively.

†Notice Eq. (2.18) is a special case of Eq. (2.2).

‡If $k_\mathrm{F}^+ = k_\mathrm{F}^-$ one can have, for example, a term $(\Delta' R_\uparrow L_\uparrow + \Delta'^* L_\downarrow R_\downarrow + \mathrm{h.c.})$. For $k_\mathrm{F}^+ \neq k_\mathrm{F}^-$, however, this term would be suppressed at low energies due to momentum mismatch.

§This topological invariant was originally derived by Qi *et al.* [36] in the weak-pairing limit. However, for the linearized low-energy model of Eq. (2.17) it is exact.

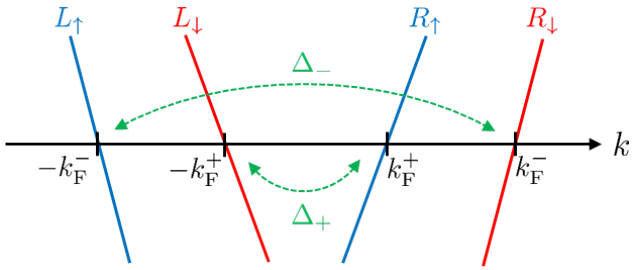

Figure 2.3: Dispersion of the low-energy Hamiltonian H_0, having two right-moving modes and two left-moving modes [see Eq. (2.17)]. The Hamiltonian H_Δ describes induced superconductivity. The pairing potential Δ_+ couples the modes of positive helicity, while Δ_- couples the modes of negative helicity. The system is in its topologically nontrivial phase when $\mathrm{sgn}(\Delta_+)\mathrm{sgn}(\Delta_-) = -1$ [see Eq. (2.19)].

where $\nu = -1$ corresponds to the topologically non-trivial phase, having a Kramers' pair of Majorana bound states at each end of the system. In Appendix 2.A we derive this results directly using a scattering-matrix approach.

It is instructive to write the superconducting part of the Hamiltonian in the following form

$$\begin{aligned} H_\Delta = \int \mathrm{d}x \Big\{ &\Delta_{\rm s} \left[R_\uparrow^\dagger(x) L_\downarrow^\dagger(x) - R_\downarrow^\dagger(x) L_\uparrow^\dagger(x) \right] \\ &+ \Delta_{\rm t} \left[R_\uparrow^\dagger(x) L_\downarrow^\dagger(x) + R_\downarrow^\dagger(x) L_\uparrow^\dagger(x) \right] + \mathrm{h.c.} \Big\}, \end{aligned} \tag{2.20}$$

where $\Delta_{\rm s,t} = (\Delta_+ \pm \Delta_-)/2$ are the singlet and triplet pairing potentials respectively. Inserting this in Eq. (2.19) results in

$$\nu = \mathrm{sgn}(\Delta_{\rm s}^2 - \Delta_{\rm t}^2). \tag{2.21}$$

Namely, the topological phase ($\nu = -1$) is obtained when the triplet pairing term exceeds in magnitude the singlet pairing term.

For a noninteracting system in proximity to a conventional s-wave SC we have seen that the system will always be in the topologically trivial phase [45, 48, 54], namely $|\Delta_{\rm s}| \geq |\Delta_{\rm t}|$. We now show that repulsive short-range interactions effectively suppress the singlet pairing term $\Delta_{\rm s}$ in comparison with the triplet term $\Delta_{\rm t}$. Depending on the bare ratio $|\Delta_{\rm t}|/|\Delta_{\rm s}|$, strong enough interactions can therefore drive the system to the topological phase. A system in which initially $|\Delta_{\rm t}|$ is of the order of (but less than) $|\Delta_{\rm s}|$, is therefore more susceptible to become topological by the presence of repulsive interactions.

The full Hamiltonian is given by $H_0 + H_\Delta + H_{\rm int}$, with H_0 and H_Δ given in Eq. (2.17), and with

$$H_{\rm int} = \int {\rm d}x \left\{ g_1^\perp \left[R_\uparrow^\dagger(x) L_\downarrow^\dagger(x) R_\downarrow(x) L_\uparrow(x) + {\rm h.c.} \right] + g_2^+ \rho_{{\rm R}\uparrow}(x)\rho_{{\rm L}\downarrow}(x) + g_2^- \rho_{{\rm R}\downarrow}(x)\rho_{{\rm L}\uparrow}(x) + g_2^\parallel \left[\rho_{{\rm R}\uparrow}(x)\rho_{{\rm L}\uparrow}(x) + \rho_{{\rm L}\downarrow}(x)\rho_{{\rm R}\downarrow}(x) \right] \right\}, \tag{2.22}$$

where $\rho_{{\rm R}s}(x) = R_s^\dagger(x) R_s(x)$ and $\rho_{{\rm L}s}(x) = L_s^\dagger(x) L_s(x)$. Here, $g_1^\perp$ is a backscattering interaction term, while g_2^+, g_2^-, and $g_2^\parallel$ are forward scattering interaction terms. In the absence of symmetry under inversion ($x \to -x$), the Fermi momenta are generally different, $k_{\rm F}^+ \neq k_{\rm F}^-$ (see Fig. 2.3). In this case $H_{\rm int}$ is the most general low-energy time-reversal symmetric Hamiltonian describing interaction between modes of opposite chirality. Interaction terms between modes of the same chirality can exist, however, they would not affect the RG flow (see Appendix 2.C), nor would they contribute to our mean-field solution, and therefore we do not include them here.

2.3.1 Mean-field theory

Before analyzing the effect of interactions using the renormalization group, it is instructive to study the mean-field solution. In this analysis we replace the low-energy interacting Hamiltonian by a quadratic Hamiltonian of the form of Eq. (2.17) with *effective* pairing potentials $\bar{\Delta}_+$ and $\bar{\Delta}_-$. Upon determining $\bar{\Delta}_\pm$ by solving self-consistent equations [see Eq. (2.26)], one can easily extract the topological invariant from this mean-field Hamiltonian.

The $g_2^\parallel$ term in Eq. (2.22) involves interaction between electrons of the same spin species. It will therefore not affect the pairing potentials $\Delta_\pm$, and its sole effect would be to change the effective chemical potential. Hence, we shall ignore it in the present mean-field treatment.

We begin by writing

$$\begin{aligned} L_\downarrow(x) R_\uparrow(x) &\equiv \langle L_\downarrow(x) R_\uparrow(x) \rangle + \delta_+(x), \\ R_\downarrow(x) L_\uparrow(x) &\equiv \langle R_\downarrow(x) L_\uparrow(x) \rangle + \delta_-(x). \end{aligned} \tag{2.23}$$

In the mean-field approximation we assume that the system has a superconducting order, and accordingly the averages of the pairing terms, $\langle L_\downarrow(x) R_\uparrow(x) \rangle$ and $\langle R_\downarrow(x) L_\uparrow(x) \rangle$, are large compared to their respective fluctuations, δ_+ and δ_-. We therefore substitute Eq. (2.23) into Eq. (2.22) and retain terms only to first order in

$\delta_\pm$. This results (up to a constant) in a mean-field Hamiltonian $H^{\rm MF} = H_0 + H_\Delta^{\rm MF}$, with H_0 given in Eq. (2.17), and with

$$H_\Delta^{\rm MF} = \int \mathrm{d}x \left[\bar{\Delta}_+ R_\uparrow^\dagger(x) L_\downarrow^\dagger(x) + \bar{\Delta}_- L_\uparrow^\dagger(x) R_\downarrow^\dagger(x) + \text{h.c.} \right], \tag{2.24}$$

where

$$\begin{aligned} \bar{\Delta}_+ &= \Delta_+ + g_1^\perp \langle R_\downarrow(x) L_\uparrow(x) \rangle + g_2^+ \langle L_\downarrow(x) R_\uparrow(x) \rangle \\ \bar{\Delta}_- &= \Delta_- + g_1^\perp \langle L_\downarrow(x) R_\uparrow(x) \rangle + g_2^- \langle R_\downarrow(x) L_\uparrow(x) \rangle. \end{aligned} \tag{2.25}$$

Since $H^{\rm MF}$ is a quadratic Hamiltonian, one can easily calculate the above pair correlation functions and arrive at self-consistent equations for $\bar{\Delta}_+$ and $\bar{\Delta}_-$. One then obtains (see Appendix 2.B)

$$\bar{\Delta}_+ = \Delta_+ - \frac{g_1^\perp}{2\pi v_-} \bar{\Delta}_- \sinh^{-1}\left(v_- \Lambda / |\bar{\Delta}_-| \right) - \frac{g_2^+}{2\pi v_+} \bar{\Delta}_+ \sinh^{-1}\left(v_+ \Lambda / |\bar{\Delta}_+| \right), \tag{2.26a}$$

$$\bar{\Delta}_- = \Delta_- - \frac{g_1^\perp}{2\pi v_+} \bar{\Delta}_+ \sinh^{-1}\left(v_+ \Lambda / |\bar{\Delta}_+| \right) - \frac{g_2^-}{2\pi v_-} \bar{\Delta}_- \sinh^{-1}\left(v_- \Lambda / |\bar{\Delta}_-| \right). \tag{2.26b}$$

These coupled equations can be solved numerically for $\bar{\Delta}_\pm$, after which the topological invariant of $H^{\rm MF}$ is obtained by $\nu = \mathrm{sgn}(\bar{\Delta}_+)\mathrm{sgn}(\bar{\Delta}_-)$. One can, however, make further analytical progress by searching for the phase boundary between $\nu = 1$ and $\nu = -1$. This occurs when either $\bar{\Delta}_- = 0$, or $\bar{\Delta}_+ = 0$. By Plugging $\bar{\Delta}_\pm = 0$ in Eq. (2.26), one obtains the conditions on the parameters of the original Hamiltonian, Eqs. (2.17) and (2.22), to be on the phase boundary. If the phase boundary occurs at $\bar{\Delta}_+ = 0$, then it is described by

$$\frac{v_- \Lambda g_1^\perp}{|g_1^\perp \Delta_- - g_2^- \Delta_+|} = \sinh\left(\frac{2\pi v_- \Delta_+}{g_1^\perp \Delta_- - g_2^- \Delta_+} \right), \tag{2.27}$$

while if it occurs at $\bar{\Delta}_- = 0$,

$$\frac{v_+ \Lambda g_1^\perp}{|g_1^\perp \Delta_+ - g_2^+ \Delta_-|} = \sinh\left(\frac{2\pi v_+ \Delta_-}{g_1^\perp \Delta_+ - g_2^+ \Delta_-} \right). \tag{2.28}$$

As a relevant example we can consider a Hubbard-type interaction, $g_1 = g_2^+ = g_2^- = U$, and furthermore $v_+ = v_- = \bar{v}$. Let us assume without loss of generality

that $|\Delta_+| > |\Delta_-|$. This means that the phase boundary will occur when $\bar{\Delta}_- = 0$, namely when

$$\frac{U}{\pi\bar{v}} = \frac{\Delta_{\rm s}/\Delta_{\rm t} - 1}{\sinh^{-1}\left(\bar{v}\Lambda/2|\Delta_{\rm t}|\right)}. \tag{2.29}$$

Figure 2.4 presents the topological phase diagram, obtained using Eq. (2.29) (see dashed line), as a function of U and the ratio $\Delta_{\rm t}/\Delta_{\rm s}$, for different values of Δ_s. As expected, for $\Delta_{\rm t}/\Delta_{\rm s} \to 0$ no finite amount of interactions can bring the system to the topological phase. In contrast, when $\Delta_{\rm t} = \Delta_{\rm s}$, the system is already at a phase transition, and any nonzero U suffices to drive the system to the topological phase. In the intermediate regime, the system will become topological for some finite interaction strength which increases with $\Delta_{\rm s}$.

2.3.2 Renormalization group analysis

In this section we study the full interacting Hamiltonian $H_0 + H_\Delta + H_{\rm int}$, given in Eqs. (2.17) and (2.22), using the renormalization group (RG). We are interested in the RG flow close to the noninteracting fixed point of free electrons, described by H_0. Both the singlet and triplet induced pairing potentials are relevant perturbations to H_0, namely this is an unstable fixed point. Below we show that the introduction of $H_{\rm int}$ causes the instability to be more towards triplet pairing with compare to singlet pairing.

To derive the flow equations of the various terms in H_Δ and $H_{\rm int}$ we use perturbative momentum shell Wilsonian RG for Fermions [72]. This procedure, whose details are given in Appendix 2.C, results in

$$\dot{y}_1^\perp = -y_2 y_1^\perp, \tag{2.30a}$$

$$\dot{y}_2 = -\frac{1}{2}\left(\frac{\bar{v}^2}{v_+ v_-} + 1\right) {y_1^\perp}^2, \tag{2.30b}$$

$$\dot{y}_2^+ = -\frac{1}{2}\frac{\bar{v}^2}{v_+ v_-} {y_1^\perp}^2, \tag{2.30c}$$

$$\dot{y}_2^- = -\frac{1}{2}\frac{\bar{v}^2}{v_+ v_-} {y_1^\perp}^2, \tag{2.30d}$$

$$\dot{\Delta}_+ = \left(1 - \frac{1}{2}y_2^+\right)\Delta_+ - \frac{1}{2}\frac{\bar{v}}{v_-} y_1^\perp \Delta_-, \tag{2.30e}$$

$$\dot{\Delta}_- = \left(1 - \frac{1}{2}y_2^-\right)\Delta_- - \frac{1}{2}\frac{\bar{v}}{v_+} y_1^\perp \Delta_+, \tag{2.30f}$$

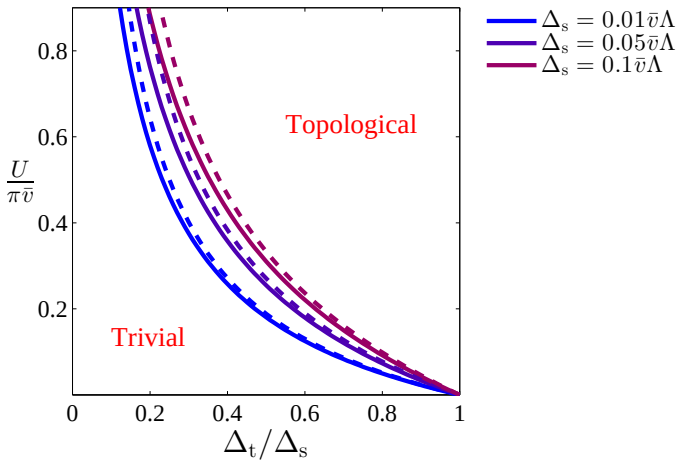

Figure 2.4: Phase diagram of the interacting model described in Eqs. (2.17) and (2.22). The phase diagram is analyzed as a function of the interaction strength $U = g_1 = g_2^+ = g_2^-$, and the ratio Δ_t/Δ_s, for different fixed values of Δ_s. Δ_s and Δ_t are the singlet and triplet induced pairing potentials, respectively (referred to $\Delta^0_{s,t}$ in Sec. 2.3.2), and are related to the pairing potentials $\Delta_\pm$ through $\Delta_{s,t} = (\Delta_+ \pm \Delta_-)/2$. The solid lines are the phase boundaries calculated using weak-coupling RG, while the dashed lines are those calculated from Eq. (2.29), obtained from a mean-field treatment. Notice that for $\Delta_t = 0$ the system cannot be driven into the topological phase for any interaction strength, i.e., some initial triplet pairing term is required. For a nonzero Δ_t, the system goes through a topological phase transition at a finite value of U which increases with Δ_s. For $\Delta_t = \Delta_s$ the system is on the verge of becoming topological, and any finite interaction will drive it to the topological phase.

where we have defined $\bar{v} = (v_+ + v_-)/2$, and the dimensionless couplings $y_1^\perp = g_1^\perp/\pi\bar{v}$, $y_2^+ = g_2^+/\pi v_+$, $y_2^- = g_2^-/\pi v_-$, and $y_2 = g_2^+/2\pi v_+ + g_2^-/2\pi v_- - g_2^\parallel/\pi\bar{v}$. The above equations have been derived using a perturbative treatment and they are valid when y_1, $y_2^\parallel$, $y_2^\pm$ and $\Delta_\pm/v_\pm\Lambda$ are all smaller than 1.

Equations (2.30a,2.30b) give rise to a Kosterlitz-Thouless (KT) type of flow for $y_1^\perp$ and y_2. It is described by the constant of motion $A^2 = y_2^2 - y_1^2$, where $y_1 \equiv y_1^\perp\sqrt{(\bar{v}^2/v_+v_- + 1)/2}$. Of greatest interest for us is the region $y_2 > y_1 \geq 0$, this corresponds to an interaction which is repulsive on all length scales. In this case, the flow of y_1 and y_2 is given by

$$y_1(\ell) = A\,\mathrm{csch}\left[A\ell + \mathrm{arcoth}\,\frac{y_2(0)}{A}\right], \tag{2.31a}$$

$$y_2(\ell) = A\coth\left[A\ell + \mathrm{arcoth}\,\frac{y_2(0)}{A}\right]. \tag{2.31b}$$

Both y_1 and y_2 flow down, saturating after an RG time $\ell_{\mathrm{sat}} \sim A^{-1}$, at 0 and A, respectively. One can insert these solutions into Eqs. (2.30c) and (2.30d), and integrate to obtain y_2^+ and y_2^-, respectively. The interaction couplings $y_1^\perp$, y_2^+, and y_2^- can then be inserted into Eqs. (2.30f,2.30e) which generally require a numerical solution for $\Delta_\pm$.

We wish to determine the topological phase diagram of the system as a function of its initial couplings. We solve the above flow equations up to an RG time ℓ^*, at which one of the pairing potential flows to strong coupling, namely $|\Delta_\pm(\ell^*)|/v_\pm\Lambda = 1$. Beyond this point the perturbative RG treatment is not valid anymore. Let us assume, without loss of generality, that Δ_+ flows to strong coupling first. This in particular means that the interaction couplings (which have flown down) are small in comparison to it, namely $y_1^\perp, y_2^\parallel, y_2^\pm \ll |\Delta_+(\ell^*)|/v_+\Lambda = 1$. If at this point $\Delta_-(\ell^*)/v_-\Lambda$ happens also to be large in comparison to $y_1^\perp, y_2^\parallel, y_2^\pm$, then we can neglect the interaction couplings. One can then use the topological invariant of a noninteracting system [see Eq. (2.19)], $\nu = \mathrm{sgn}[\Delta_+(\ell^*)]\mathrm{sgn}[\Delta_-(\ell^*)]$. Generally, however, $\Delta_-(\ell^*)$ can be small, and one has to modify the expression for ν to account for the non-negligible interaction terms.

To this end we note that since $\Delta_+(\ell^*)$ is large, the positive-helicity degrees of freedom [$R_\uparrow(x)$ and $L_\downarrow(x)$] are gapped, and we can safely integrate them out. Upon doing that, one is left with an action containing only the negative-helicity fields [$R_\downarrow(x)$ and $L_\uparrow(x)$], with a pairing potential $\Delta'_- = \Delta_-(\ell^*) + \delta\Delta_-$. To leading order in the interaction couplings, the correction is given by (see Appendix 2.C)

$$\delta\Delta_- = -\frac{\bar{v}}{2v_+}y_1^\perp(\ell^*)\Delta_+(\ell^*)\sinh^{-1}\left[\frac{v_+\Lambda}{|\Delta_+(\ell^*)|}\right] = -\frac{1}{2}y_1^\perp(\ell^*)\mathrm{sgn}[\Delta_+(\ell^*)]\sinh^{-1}(1)\bar{v}\Lambda.$$

(2.32)

At this point we can continue the RG procedure, applied only to the negative-helicity degrees of freedom,

$$\dot{y}_2^- = 0, \tag{2.33a}$$

$$\dot{\Delta}'_- = \left(1 - \frac{1}{2}y_2^-\right)\Delta'_-, \tag{2.33b}$$

namely Δ'_- flows to strong coupling (without changing sign), while y_2^- remains perturbative. We can therefore use the topological invariant of noninteracting systems, only with $\Delta_-(\ell^*)$ substituted by Δ'_-, $\nu = \mathrm{sgn}[\Delta_+(\ell^*)]\mathrm{sgn}[\Delta'_-]$. Finally, accounting also for the possibility that Δ_- flows to strong coupling before Δ_+, we can write

$$\begin{aligned}\nu =& \mathrm{sgn}\left\{\frac{\Delta_+(\ell^*)}{\bar{v}\Lambda} - \frac{\sinh^{-1}(1)}{2}y_1^\perp(\ell^*)\mathrm{sgn}[\Delta_-(\ell^*)]\right\}\times \\ & \mathrm{sgn}\left\{\frac{\Delta_-(\ell^*)}{\bar{v}\Lambda} - \frac{\sinh^{-1}(1)}{2}y_1^\perp(\ell^*)\mathrm{sgn}[\Delta_+(\ell^*)]\right\},\end{aligned} \tag{2.34}$$

where ℓ^* is the RG time when the first of Δ_+ and Δ_- reaches strong coupling.

To understand how repulsive interactions drive the system into the TRITOPS phase, let us concentrate on the special case, $v_+ = v_-$, $y_2^- = y_2^+$, for which Eqs. (2.30f, 2.30e) reduce to

$$\dot{\Delta}_\mathrm{s} = \left(1 - \frac{1}{2}y_2^+ - \frac{1}{2}y_1\right)\Delta_\mathrm{s}, \tag{2.35a}$$

$$\dot{\Delta}_\mathrm{t} = \left(1 - \frac{1}{2}y_2^+ + \frac{1}{2}y_1\right)\Delta_\mathrm{t}. \tag{2.35b}$$

The effect of forward scattering and of backscattering on the pairing potentials is now apparent. The forward scattering term y_2^+ equally suppresses the singlet and triplet pairing terms. The backscattering term y_1, on the other hand, suppresses Δ_s, while strengthening Δ_t, causing the latter to flow faster to strong coupling. From Eq. (2.35) one can extract the ratio between the triplet and singlet pairing terms as a function of RG time,

$$\frac{\Delta_\mathrm{t}(\ell)}{\Delta_\mathrm{s}(\ell)} = \frac{\Delta_\mathrm{t}^0}{\Delta_\mathrm{s}^0}\exp\left[\int_0^\ell \mathrm{d}\ell' y_1(\ell')\right]. \tag{2.36}$$

If the time it takes y_1 to flow to zero, ℓ_sat, is much shorter than ℓ^*, we can approximate the ratio $\Delta_\mathrm{t}(\ell^*)/\Delta_\mathrm{s}(\ell^*)$ by taking the upper limit of the above integral

to infinity. Using Eq. (2.31a), one obtains in this case

$$\frac{\Delta_{\rm t}(\ell^*)}{\Delta_{\rm s}(\ell^*)} \simeq \frac{\Delta_{\rm t}^0}{\Delta_{\rm s}^0}\sqrt{\frac{y_2^0+y_1^0}{y_2^0-y_1^0}}. \tag{2.37}$$

Furthermore, since by our assumption $y_1(\ell^*) \simeq 0$ (follows from $\ell_{\rm sat} \ll \ell^*$), Eq. (2.34) tells us that the condition for the system to be topological is simply $|\Delta_{\rm t}(\ell^*)| > |\Delta_{\rm s}(\ell^*)|$. We wish to understand when this approximation is valid. To this end, we can estimate the time it would take for one of the pairing potentials to reach strong coupling, $\ell^* \sim \ln(v_\pm\Lambda/\Delta_\pm^0)$*. Namely, the above long RG-time approximation will be valid if the initial pairing potentials are small enough such that $\Delta_\pm^0 \ll v_\pm\Lambda\exp(-1/A)$. Note that the above approximation will necessarily be violated close to the separatrix of the KT flow, since there $A \to 0$.

We can now use the result, Eq. (2.37) to construct the phase diagram of the system as a function of the initial values of y_2 and y_1, given fixed initial conditions for $\Delta_{\rm s}$ and $\Delta_{\rm t}$. Assuming that we can take the long RG-time limit, we can find an equation for the phase boundary in the y_2y_1-plane, by setting equation (2.37) to 1 and solving for y_1. One then immediately finds that the phase boundary obeys the equation

$$y_1^0 = \frac{1-(\Delta_{\rm t}^0/\Delta_{\rm s}^0)^2}{1+(\Delta_{\rm t}^0/\Delta_{\rm s}^0)^2}\cdot y_2^0, \tag{2.38}$$

namely, the system is in the topological phase above this line in the y_1y_2-plane. The topological region becomes bigger as the ratio $\Delta_{\rm t}^0/\Delta_{\rm s}^0$ increases. In Fig. 2.5 we present the topological phase diagram in the y_2y_1-plane for fixed initial values $\Delta_{\rm s}$ and $\Delta_{\rm t}$. The phase boundary is obtained by numerically solving Eq. (2.30) up to a time ℓ^*, and then invoking Eq. (2.34), with ℓ^* being the RG time when the first coupling becomes 1. The dashed red line shows the long-RG time approximation of the phase boundary, Eq. (2.38). As anticipated, it becomes more accurate as A increases. We note that above the separatrix of the KT flow, y_1 and y_2 flow to strong coupling and the system is driven into an intrinsically topological phase [40, 73], irrespective of the initial induced potentials $\Delta_\pm$. Some nonvanishing induced pairing is however necessary to keep the system fully gapped.

Let us now reconsider the case of a Hubbard-type interaction, $g_1^\perp = g_2^+ = g_2^- = U$, and $g_2^\parallel = 0$. Note that for $v_+ = v_-$ this mean $y_2 = y_1$, while for $v_+ \neq v_-$, this means $y_2 \geq y_1$ [see the definitions below Eq. (2.30)]. Importantly, in both cases the KT

*This estimation is obtained upon neglecting the second order terms in Eqs. (2.30e,2.30f) and integrating them up to $\Delta_\pm(\ell^*) = v_\pm\Lambda$.

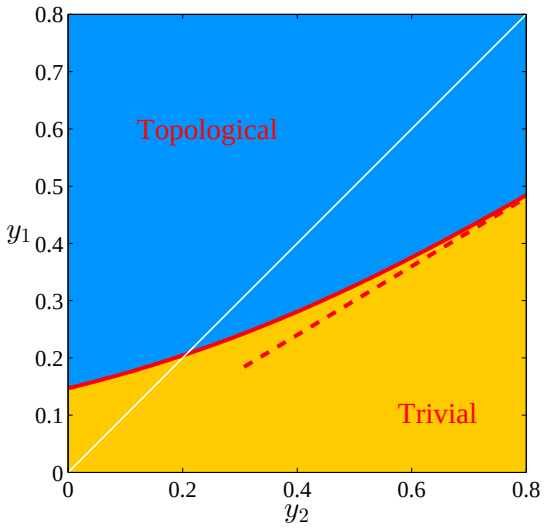

Figure 2.5: Phase diagram of the interacting model described in Eqs. (2.17) and (2.22), as a function of forward (y_2) and backward (y_1) scattering interaction terms. The solid red line shows the phase boundary, calculated using the RG flow equations, Eq. (2.30), and the topological invariant, Eq. (2.34). The dashed red line indicates the long RG-time approximation for the phase boundary, Eq. (2.38). It agrees with the numerical result when $\Delta_{\pm}^0 \ll v_{\pm}\Lambda \exp(-1/A)$, where $A^2 = y_2^2 - y_1^2$. The white solid line corresponds to the separatrix of the Kosterlitz- Thouless flow, above which y_1 and y_2 flow to strong coupling. In obtaining this phase diagram, we have used $v_- = v_+ = \bar{v}$, $y_2^+ = y_2^- = y_2$, and the initial singlet and triplet pairing potentials were taken to be $\Delta_{\rm t}^0 = 0.01\bar{v}\Lambda$ and $\Delta_{\rm s}^0 = 0.02\bar{v}\Lambda$, respectively.

flow equations dictates that the interaction couplings flow down. Figure 2.4 shows the phase diagram for this Hubbard-type interaction, for $v_+ = v_-$. The critical interaction strength U which defines the phase boundary is numerically calculated as a function of the initial ratio $\Delta_{\rm t}^0/\Delta_{\rm s}^0$, for different fixed values of $\Delta_{\rm s}^0$. We note that this phase boundary (solid lines) agrees well with that obtained from the mean field analysis (dashed lines), given in Eq. (2.29).

The results presented in Figs. 2.4 and 2.5 are both for the case of $g_2^+ = g_2^-$, $v_+ = v_-$. Under these conditions, if the initial triplet term is zero, it will remain zero for all RG times, as can be seen from Eq. (2.35b). This is no longer the case upon relaxing one of these conditions, since the flow equations generally couple $\Delta_{\rm t}$ to $\Delta_{\rm s}$ [see Eq. (2.30)]. Consequently, a phase transition into the topological phase can occur at a finite interaction strength, even for vanishingly small initial

$\Delta_{\rm t}^0$. Nevertheless, systems in which the initial triplet term can be of the order of the singlet term, such as those presented in Sec. 2.4, are more susceptible to being driven into the topological phase by the effect of repulsive interactions.

2.4 Microscopic Models

In the previous section we have studied a general low-energy Hamiltonian, and showed that it is driven into the TRITOPS phase due to repulsive interactions. In this section we wish to explore specific microscopic models of systems which can be realized in currently-available experimental setups. These are (i) a narrow 2d quantum spin Hall insulator (QSHI) partially covered by an s-wave SC, and (ii) a quasi 1d semiconductor nanowire proximitized by an s-wave SC. We show that these systems are described at low energies by the minimal model studied above with a nonvanishing induced triplet pairing. Later, in Sec. 2.5 we shall perform numerical mean-field calculations and *Density Matrix Renormalization Group* (DMRG) calculations on system (ii) to verify that it indeed enters the topological phase.

2.4.1 Narrow quantum spin Hall insulator

We consider a narrow two-dimensional quantum spin Hall Insulator (QSHI) in proximity to an s-wave SC [74]. A QSHI [5, 31, 32] is a phase characterized by a pair of counter-propagating helical modes on each edge of the system as depicted in Fig. 2.6(a). We define the correlation length $\xi_{\rm QSHI}$ as the characteristic length with which the helical edge modes decay into the bulk. If the width of the bar d is of the order of $\xi_{\rm QSHI}$ or less, then gapless modes of opposite edges are coupled and an energy gap is opened [cf. Fig. 2.6(b) and Fig. 2.6(c)]. When the chemical potential lies above or below the gap, the low-energy sector of the system is described by a one-dimensional model having four Fermi points, similar to the Hamiltonian H_0 of Eq. (2.17). We now show that coupling one of the edges to a conventional s-wave SC results in a nonvanishing triplet pairing component.

In the absence of interactions, the two coupled edges are described by the following Hamiltonian

$$\begin{aligned} H_{\rm QSHI} &= \sum_k \Psi_k^\dagger \mathcal{H}(k) \Psi_k \;\; ; \;\; \Psi_k^\dagger = (a_{k\uparrow}^\dagger, b_{k\uparrow}^\dagger, a_{-k\downarrow}, b_{-k\downarrow}) \\ \mathcal{H}(k) &= [-\mu + (\delta\mu + vk)\lambda^z + t\lambda^x]\tau^z + \frac{\Delta_{\rm ind}}{2}(1+\lambda^z)\tau^x, \end{aligned} \tag{2.39}$$

where $a_{ks}^\dagger$ ($b_{ks}^\dagger$) creates an electron with momentum k and spin $s =\uparrow,\downarrow$ on the lower (upper) edge of the sample. $\{\tau^i\}_{i=x,y,z}$ and $\{\lambda^i\}_{i=x,y,z}$ are sets of Pauli matrices in

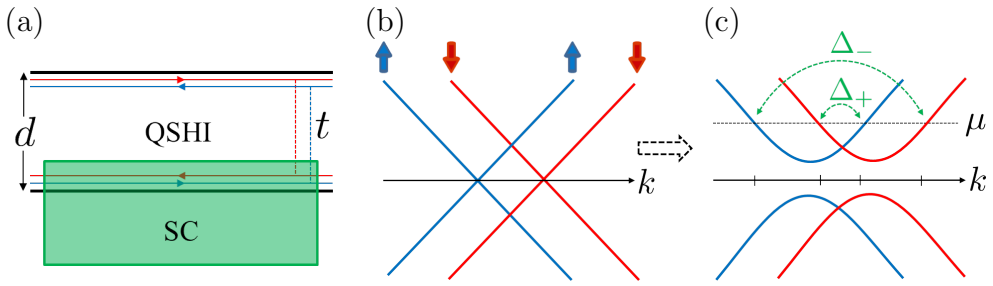

Figure 2.6: (a) A narrow two dimensional quantum spin Hall insulator in proximity to a conventional s-wave superconductor. (b) In the absence of induced superconductivity and tunneling between opposite edges, the low-energy electronic spectrum is described by two pairs of helical edge states, the helicity being opposite for the two edges. (c) If the width of the sample d is of the order of the characteristic correlation length ξ_{QSHI} or less, then the opposite edges are coupled (with a coupling constant t), and an energy gap is opened. Such a coupling between the edge modes is necessary in order to have nonzero backscattering interaction, which is crucial for realizing the topological phase (see Sec. 2.3.1 and Sec. 2.3.2).

the particle-hole space and the lower edge-upper edge space, respectively. Here, v is the propagation velocity of the edge modes, t is the coupling constant between the lower and upper edge modes (which results from the finite width of the sample), $\mu \pm \delta\mu$ are the chemical potentials at the upper and lower edge, respectively, and Δ_{ind} is the pairing potential induced by the SC on the lower edge of the sample [cf. Fig. 2.6(a)].

We consider the case where, in the absence of proximity, the chemical potential lies inside the upper band [see Fig. 2.6(c)]*, and where the induced pairing, Δ_{ind}, is small in comparison with the distance to the lower band, $\mu + |t|$. We can therefore project out the lower band, arriving at the following effective Hamiltonian for the upper band

$$H_{\mathrm{eff}} = \sum_k \left\{ \sum_{s=\uparrow,\downarrow} \left(\sqrt{t^2 + (\delta\mu + svk)^2} - \mu \right) c_{ks}^\dagger c_{ks} + \Delta(k) \left(c_{k\uparrow}^\dagger c_{-k\downarrow}^\dagger + \mathrm{h.c.} \right) \right\}, \tag{2.40}$$

with the effective pairing potential

$$\Delta(k) = \frac{\Delta_{\mathrm{ind}}}{2} \left[1 + (\delta\mu + vk)/\sqrt{t^2 + (\delta\mu + vk)^2} \right]. \tag{2.41}$$

*Similar results are obtained if one consider the case where the chemical potential lies inside the lower band.

Here, $c^\dagger_{ks}$ describes electronic modes in the upper band with momentum k and spin s. It is related to the left and right edge modes through

$$\begin{aligned} &c^\dagger_{ks} = \cos(\phi_{ks}) a^\dagger_{ks} + \sin(\phi_{ks}) b^\dagger_{ks}, \\ &\cos(2\phi_{ks}) = (\delta\mu + vks)/\sqrt{t^2 + (\delta\mu + vks)^2}, \\ &\sin(2\phi_{ks}) = t/\sqrt{t^2 + (\delta\mu + vks)^2}, \end{aligned} \tag{2.42}$$

where we have used a convention in which $s = 1$ corresponds to spin $\uparrow$, and $s = -1$ corresponds to spin $\downarrow$.

Assuming weak pairing*, we can linearize the spectrum near the Fermi energy and impose a momentum cutoff Λ, resulting in the following Hamiltonian

$$H^{\rm lin} = \sum_{|k|<\Lambda} \Big\{ \bar{v} k \sum_{s=\uparrow,\downarrow} (R^\dagger_{ks} R_{ks} - L^\dagger_{ks} L_{ks}) + (\Delta_+ R^\dagger_{k\uparrow} L^\dagger_{-k\downarrow} + \Delta_- L^\dagger_{k\uparrow} R^\dagger_{-k\downarrow} + \text{h.c.}) \Big\} \tag{2.43}$$

where

$$R_{k\uparrow} = c_{k^+_{\rm F}+k,\uparrow} \quad ; \quad L_{k\downarrow} = c_{-k^+_{\rm F}+k,\downarrow} \quad ; \quad R_{k\downarrow} = c_{k^-_{\rm F}+k,\downarrow} \quad ; \quad L_{k\uparrow} = c_{-k^-_{\rm F}+k,\uparrow}, \tag{2.44}$$

and

$$\Delta_+ = \Delta(k^+_{\rm F}) \quad ; \quad \Delta_- = \Delta(-k^-_{\rm F}). \tag{2.45}$$

The velocity of the modes at the Fermi points is given by

$$\bar{v} = v\sqrt{1 - (t/\mu)^2}, \tag{2.46}$$

and the Fermi momenta are given by $k^\pm_{\rm F} = (\mu\bar{v}/v \mp \delta\mu)/v$ (Notice that since the chemical potential is assumed to lie inside the upper band one has $\mu > |t|$). The Hamiltonian of Eq. (2.43) is exactly the minimal model Hamiltonian of Eq. (2.17), written in momentum space, with $v_+ = v_- = \bar{v}$.

As discussed above, the system is in its topological phase when $\text{sgn}(\Delta_+)\text{sgn}(\Delta_-) = -1$. Alternatively stated, this occurs when $|\Delta_{\rm t}| > |\Delta_{\rm s}|$ [see Eq. (2.20)]. For the model at hand one has

$$\Delta_{\rm s} = \Delta_{\rm ind}/2 \quad ; \quad \Delta_{\rm t} = \frac{\bar{v}}{v}\Delta_{\rm ind}/2. \tag{2.47}$$

*Weak pairing here means that the pairing potential is small with compare to the distance from the Fermi energy to the bottom of the band, namely $\mu - |t| \ll |\Delta(k)|$.

As expected, in the absence of interactions $|\Delta_{\rm t}| \leq |\Delta_{\rm s}|$. Importantly, however, $\Delta_{\rm t}$ is nonzero, and can generally be of similar magnitude to $\Delta_{\rm s}$, making the system susceptible to being driven into the TRITOPS phase by short-range repulsive interactions.

The existence of a nonvanishing triplet pairing term can also be understood from a simple qualitative argument. The lower and upper edges of the QSHI host modes of positive and negative helicity, respectively. Since the SC is coupled to the *lower* edge, the pairing of the positive-helicity modes, Δ_+, is larger in magnitude than that of the negative-helicity modes, Δ_-, and consequently $\Delta_{\rm t} \neq 0$. This agrees with Eqs. (2.46) and (2.47) which suggest that $|\Delta_{\rm t}|$ is maximal when the edges are maximally separated (namely when $t = 0$). We note, however, that some overlap between the edge modes is necessary in order to eventually achieve the TRITOPS phase. This is because in the absence of such overlap, the backscattering interaction vanishes. As was shown in Sec. 2.3.1 and Sec. 2.3.2, this interaction terms is crucial for the system to be driven into the topological phase.

2.4.2 Proximity-coupled semiconductor wire

Next we concentrate on another system which can be driven into the TRITOPS phase by repulsive interactions, a spin-orbit coupled semiconductor nanowire. We now show that this system is described at low-energies by the Hamiltonian of Eq. (2.17) with a nonvanishing triplet pairing term.

Consider a semiconductor spin-orbit coupled nanowire in proximity to a bulk three-dimensional s-wave SC as depicted in Fig. 2.7(a). The wire is infinite in the x direction, while its lateral dimensions are $w_y \times w_z$. We wish to write the Hamiltonian for the lowest transverse mode of the wire. If the width of the wire is small compared to the spin-orbit coupling length, then the z component of the electron's spin is approximately conserved*. Under this assumption, and in the absence of electron-electron interactions, the effective Hamiltonian for the lowest band is given by

$$H_{\rm eff} = \sum_k \left\{ \sum_{ss'} \left[\left(\frac{k^2}{2m^*} - \mu \right) \delta_{ss'} + \alpha k \sigma^z_{ss'} \right] c^\dagger_{ks} c_{ks'} + \Delta(k)(c^\dagger_{k\uparrow} c^\dagger_{-k\downarrow} + \text{h.c.}) \right\}, \quad (2.48)$$

where $c^\dagger_{ks}$ creates an electron in the lowest transverse mode of the wire with spin s and momentum k along the x direction. Here m^* is the effective mass of electrons in the wire, μ is the chemical potential, and α is the spin-orbit coupling strength.

*See Appendix 2.D for a detailed derivation.

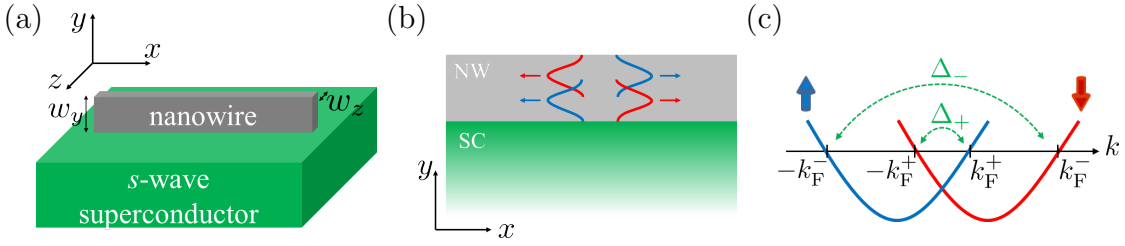

Figure 2.7: (a) A semiconductor quasi one-dimensional nanowire on top of a bulk s-wave superconductor. (b) As a result of spin-orbit coupling, the spatial profile of the electronic wave functions depends on the factor ks, with $s = 1$ for spin $\uparrow$, and $s = -1$ for spin $\downarrow$, and with k being the momentum in the x direction. Wave functions with positive helicity ($ks > 0$) are pushed towards the superconductor, while wave functions with negative helicity ($ks < 0$) are pushed away from it. (c) Dispersion of the lowest transverse mode of the semiconductor nanowire. The modes near $\pm k_F^+$ have a positive helicity and therefore experience a pairing potential Δ_+ which is larger than the pairing Δ_- of modes at $\pm k_F^-$ which have negative helicity. This results in a nonvanishing triplet pairing term $\Delta_t = (\Delta_+ - \Delta_-)/2$.

The induced pairing potential in the lowest transverse band is approximately given by

$$\Delta(k) = \Delta_{\text{ind}}(1 + \beta k), \tag{2.49}$$

where β is a constant which arises due to spin-orbit interaction. Equation (2.49) is derived in Appendix 2.D by perturbatively considering a general spin-orbit coupling term in the wire, and integrating out the superconductor's degrees of freedom [see Eq. (2.97)]. Physically, Eq. (2.49) implies that modes with different helicity have a different induced pairing potential [see Fig. 2.7(b-c)]; we will elaborate on the mechanism behind this effect below.

If the chemical potential lies inside the band, then there are two pairs of Fermi points $\pm k_F^+$ and $\pm k_F^-$ as depicted in Fig. 2.7(c). Assuming that the induced pairing potential is much smaller than distance to the bottom of the band, we linearize the spectrum near the Fermi points as in Sec 2.4.1. This results in exactly the same Hamiltonian of Eq. (2.43) and Eq. (2.17), where as before we define $R_{k\uparrow,\downarrow} = c_{k_F^\pm + k,\uparrow,\downarrow}$, $L_{k\uparrow,\downarrow} = c_{-k_F^\mp + k,\uparrow,\downarrow}$, and $\Delta_\pm = \Delta(\pm k_F^\pm)$. The velocities of the modes at the Fermi points are given by $v_+ = v_- = \sqrt{2\mu/m^* + \alpha^2} \equiv \bar{v}$, and the Fermi momenta are given by $k_F^\pm = m^*(\bar{v} \mp \alpha)$. The momentum dependence of $\Delta(k)$ results in the following

singlet and triplet pairing terms

$$\Delta_+ = \Delta_{\rm ind}(1+\beta k_{\rm F}^+) \quad ; \quad \Delta_- = \Delta_{\rm ind}(1-\beta k_{\rm F}^-), \tag{2.50}$$

which translate into

$$\Delta_{\rm s} = (1-\beta\alpha m^*)\Delta_{\rm ind} \quad ; \quad \Delta_{\rm t} = \beta m^* \bar{v} \Delta_{\rm ind}. \tag{2.51}$$

Equation (2.49) was derived in a perturbative treatment, and therefore it is valid only for sufficiently small β, for which $\Delta_{\rm s}$ exceeds $\Delta_{\rm t}$. This holds more generally, as the bare induced triplet pairing potential has to be smaller than the singlet term in the absence of interactions [45, 48].

The form of $\Delta(k)$ is derived in Appendix 2.D in detail, however the essence of that derivation can be captured in the following simplified model. Let us consider the electrons in the wire to be confined in the y direction by a harmonic potential $V_{\rm c}(y) = m^*\omega_{\rm c}^2 y^2/2$, where $y=0$ is at the center of the wire. The spin-orbit coupling in the wire contributes a term of the form $\mathcal{H}_{\rm so} = u\partial_y V_{\rm c}(y)\hat{p}_x\sigma^z$. Ignoring the z direction for the moment (justified when $w_z \ll w_y$), the electrons in the wire are governed by the first-quantized Hamiltonian

$$\mathcal{H}_{\rm wire} = \frac{\hat{p}_x^2+\hat{p}_y^2}{2m^*} + \frac{1}{2}m^*\omega_c^2(y+u\hat{p}_x\sigma^z)^2. \tag{2.52}$$

The eigenfunctions of $\mathcal{H}_{\rm wire}$ are $\exp(ikx)\eta_n(y+uks)$, where s is the spin, and $\eta_n(y)$ are the eigenfunctions of an harmonic oscillator of mass m^* and frequency ω_c. It is now apparent that states with $ks>0$ are shifted towards the SC ($y<0$), while states with negative $ks<0$ are shifted away from the SC ($y>0$) [75]. This is illustrated in Fig. 2.7(b) Upon coupling the SC to the wire, modes with $ks>0$ will therefore experience an induced pairing potential which is bigger that that of modes with $ks<0$, in accordance with Eq. (2.50).

2.5 Numerical Analysis

In this section we concentrate on the semiconductor nanowire realization of the TRITOPS phase (see Sec. 2.4.2), and numerically study its phase diagram. First, we construct a tight-binding model which captures the correct symmetry of the SOC in the wire. We then study its phase diagram using both a Hartree-Fock approximation and a DMRG analysis. We verify that for sufficiently strong repulsive interactions the model indeed gives rise to a TRITOPS phase. Finally, we study the behavior of the system under breaking of TRS, and demonstrate that the dependence of the

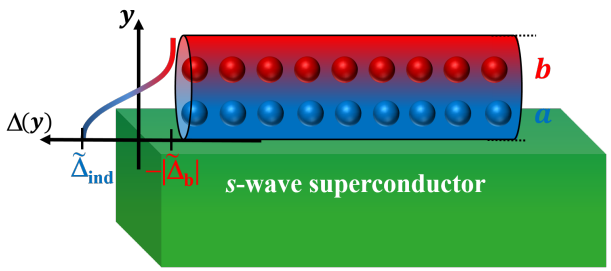

Figure 2.8: The proposed system consists of a single quasi-1D wire (modelled by two chains) with SOC, coupled to a conventional s-wave superconductor. Integrating out the degrees of freedom of the superconductor generates a pairing potential $\Delta_{\rm ind}$ on the chain adjacent to the superconductor. Repulsive interactions in the wire which resist local pairing of electrons, induce a pairing potential $\tilde{\Delta}_{\rm b}$ on the 'b' chain with an opposite sign to $\Delta_{\rm ind}$.

splitting of the zero-bias conductance peak on the direction of the Zeeman field can be used as a distinct experimental signature of the TRITOPS phase.

To model the proximity-coupled interacting semiconductor nanowire we consider the following two-chain tight-binding Hamiltonian (see Fig. 2.8):

$$\begin{aligned} H &= \frac{1}{2}\sum_k \Psi_k^\dagger \mathcal{H}_{0,k}\Psi_k + \sum_{i,\nu} U_\nu \hat{n}_{i\nu\uparrow}\hat{n}_{i\nu\downarrow} \\ \mathcal{H}_{0,k} &= \left[\bar{\xi}_k + \delta\xi_k\lambda^z - (\bar{\alpha}+\delta\alpha\lambda^z)\sin k\ \sigma^z + t_{\rm ab}\lambda^x\right]\tau^z + \Delta_{\rm ind}/2\ \cdot(1+\lambda^z)\,\tau^x, \end{aligned} \tag{2.53}$$

where $\Psi_k^\dagger = (\psi_k^\dagger,\ \ -i\sigma^y\psi_{-k})$. The two spatially distinct chains are labeled, a and b, such that $\psi_k^\dagger = (c_{{\rm a},k\uparrow}^\dagger\ \ c_{{\rm b},k\uparrow}^\dagger\ \ c_{{\rm a},k\downarrow}^\dagger\ \ c_{{\rm b},k\downarrow}^\dagger)$. $\{\tau_j\}_{j=x,y,z}$, $\{\lambda_j\}_{j=x,y,z}$, and $\{\sigma_j\}_{j=x,y,z}$ are sets of Pauli matrices operating on particle-hole (PH), chain and spin degrees of freedom, respectively. Here, $\bar{\xi}_k, \delta\xi_k, \bar{\alpha}$ and $\delta\alpha$ are defined as $(\xi_{k,{\rm a}}\pm\xi_{k,{\rm b}})/2$ and $\alpha_{\rm a}\pm\alpha_{\rm b}$, respectively, and $\xi_{k,\nu} = 2t_\nu\,(1-\cos k) - \mu_\nu$, $\nu = {\rm a},{\rm b}$. The parameters $t_\nu, \alpha_\nu, \mu_\nu$ and U_ν represent the hopping, SOC, chemical potential and on-site repulsion on each of the chains, $\nu = {\rm a},{\rm b}$, while $t_{\rm ab}$ is the hopping between the chains. The operator $\hat{n}_{i,\nu,s}$ represents the number of particles with spin s on site i of chain ν.

The need for (at least) two chains in the model comes from the need to simulate the dependence of the SOC in the y direction. As explained in Sec. 2.4.2 and in Appendix 2.D, the finite induced triplet pairing has its origin in the SOC term which stems from the asymmetric part of the electric field. In a lattice model this can be most-simply captured by assuming two parallel chains, with two different strength of SOC, $\alpha_{\rm a}$ and $\alpha_{\rm b}$.

2.5.1 Hartree-Fock

We are interested in the topological phase diagram of the Hamiltonian in Eq. (2.53). In the Hartree-Fock analysis we consider a set of trial wave-functions which are ground states of the following quadratic Hamiltonian:

$$H_{\rm HF} = \frac{1}{2}\sum_k \Psi_k^\dagger \mathcal{H}_k^{\rm HF} \Psi_k, \quad ; \quad \mathcal{H}_k^{\rm HF} = \tilde{\mathcal{H}}_{0,k} + \tilde{\Delta}_{\rm b}/2 \ \cdot (1-\lambda^z)\,\tau^x, \tag{2.54}$$

where $\tilde{\mathcal{H}}_{0,k}$ has the same form as $\mathcal{H}_{0,k}$, with effective parameters $\tilde{\mu}_{\rm a}, \tilde{\mu}_{\rm b}$ and $\tilde{\Delta}_{\rm ind}$, and where $\tilde{\Delta}_{\rm b}$ is an effective pairing potential on chain 'b'. Upon determining the four effective ~~parameter~~ parameters, the value of the topological invariant can be obtained by applying the results of Sec. (2.2.3) to Eq. (2.54). We determine the effective parameters by numerically minimizing the expectation value of the full Hamiltonian,

$$\begin{aligned} \langle H\rangle_{\rm HF} &= E_0 + \frac{1}{L}\sum_\nu U_\nu \left(N_{\nu,\uparrow}N_{\nu,\downarrow} + |P_\nu|^2\right), \\ N_{\nu,s} &= \textstyle\sum_k \langle c^\dagger_{\nu,k,s} c_{\nu,k,s}\rangle_{\rm HF}, \quad P_\nu = \sum_k \langle c^\dagger_{\nu,k,\uparrow} c^\dagger_{\nu,-k\downarrow}\rangle_{\rm HF} \ , \\ E_0 &= \frac{1}{2}\sum_{k,m,n} \mathcal{H}_{0,k,mn}\langle \Psi^\dagger_{k,m}\Psi_{k,n}\rangle_{\rm HF}, \end{aligned} \tag{2.55}$$

where L is the number of sites in each chain, and we have used Wick's theorem, noting the exchange term vanishes due to the σ^z conservation of $\mathcal{H}_k^{\rm HF}$.

We are interested in the conditions under which $\mathcal{H}_k^{\rm HF}$ is in the topological phase. We note this Hamiltonian possesses both TRS $\Theta = i\sigma^y K$ and PH symmetry $\Xi = \tau^y\sigma^y K$, expressed by $\Theta\mathcal{H}_k^{\rm HF}\Theta^{-1} = \mathcal{H}_{-k}^{\rm HF}$ and $\Xi\mathcal{H}_k^{\rm HF}\Xi^{-1} = -\mathcal{H}_{-k}^{\rm HF}$, confirming it is in symmetry class DIII [33]. Following Sec. 2.2.3, we obtain an expression for the $\mathbb{Z}_2-$invariant by using the chiral symmetry $\{\mathcal{H}^{\rm HF}, \tau^y\} = 0$, to divide $\mathcal{H}^{\rm HF}$ into two off-diagonal blocks

$$e^{i\frac{\pi}{4}\tau^x}\mathcal{H}^{\rm HF}(k)e^{-i\frac{\pi}{4}\tau^x} = \begin{pmatrix} 0 & \mathcal{B}_k \\ \mathcal{B}_k^\dagger & 0 \end{pmatrix}. \tag{2.56}$$

In this model we have an additional σ^z symmetry, allowing $\mathcal{B}_k$ to be further separated into two diagonal blocks, $\mathcal{B}_k^\uparrow$ and $\mathcal{B}_k^\downarrow = \mathcal{B}_{-k}^{\uparrow}$. The $\mathbb{Z}_2$ invariant is then given by the parity of the winding number of θ_k, defined by $\exp(i\theta_k) = \det\mathcal{B}_k^\uparrow/|\det\mathcal{B}_k^\uparrow|$. For the model at hand one has

$$\det\mathcal{B}_k^\uparrow = t_{\rm ab}^2 + \tilde{\Delta}_{\rm ind}\tilde{\Delta}_{\rm b} - \tilde{\varepsilon}_{{\rm a},k}\tilde{\varepsilon}_{{\rm b},k} - i(\tilde{\Delta}_{\rm ind}\tilde{\varepsilon}_{{\rm b},k} + \tilde{\Delta}_{\rm b}\tilde{\varepsilon}_{{\rm a},k}), \tag{2.57}$$

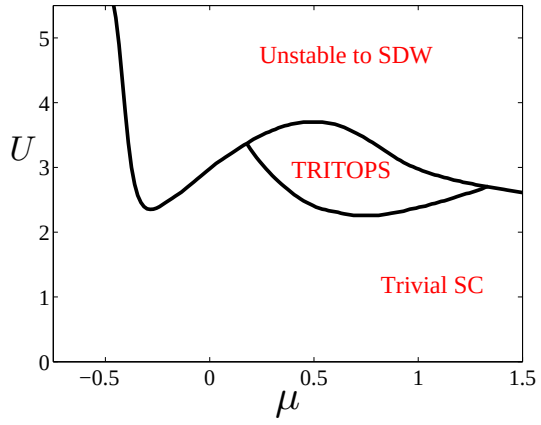

Figure 2.9: Hartree-Fock phase diagram as a function of chemical potential $\mu_{\rm a} = \mu_{\rm b} = \mu$, and interaction strength U, for $t_{\rm a} = t_{\rm b} = 1, t_{\rm ab} = 0.4, \alpha_{\rm a} = 0, \alpha_{\rm b} = 0.6$, and $\Delta_{\rm ind} = 1$. The diagram includes a time-reversal invariant topological superconductor phase (TRITOPS), a trivial superconductor phase, and a region in which the Hartree-Fock solution is locally unstable to the formation of spin-density waves (see the footnote $*$).

where $\tilde{\varepsilon}_{\nu,k} = 2t_\nu(1-\cos k) - 2\alpha_\nu \sin k - \tilde{\mu}_\nu$. It can be shown from Eq. (2.57) that in order to have a non-trivial winding number (i.e. odd), one must have different SOC on the two chains, $\alpha_{\rm a}/t_{\rm a} \neq \alpha_{\rm b}/t_{\rm b}$. We note, however, that this requirement can be relaxed by adding a SOC term associated with hopping between the chains. We can now solve the Hartree-Fock problem for the effective parameters, and then calculate the $\mathbb{Z}_2$ invariant using Eq. (2.57) to obtain the phase-diagram of the system.

In addition to the trivial and the topological superconducting phases other competing phases may appear, which are not accounted for in our trial wave-functions. In particular, absent from Eq. (2.54) are terms which break the lattice translational invariance and drive the system to a spin-density wave (SDW) state*. To examine this possibility, after obtaining the effective parameters in Eq. (2.54), we add to $H_{\rm HF}$ the term $-\sum_{\nu,q,s} \phi_{\nu-qs}\hat{\rho}_{\sigma qs}$, where $\hat{\rho}_{\nu qs}$ is the Fourier transform of $\hat{n}_{i,\nu s}$. We then use *linear response* to calculate the Hessian matrix $\partial^2\langle H\rangle_{\rm HF}/\partial\phi_{\nu',q,s'}\partial\phi_{\nu,-q,s}$. For the Hartree-Fock solution to be locally stable to formation of SDW we demand the Hessian to be positive definite (see Appendix 2.E for details). In Fig. 2.9 we present the Hartree-Fock phase diagram as a function of chemical potential and interaction

*This ordered phase is not permissible in the continuum limit in 1D, as it requires the breaking of a continuous symmetry. We therefore expect that long-range fluctuations (which are not accounted for in the Hartree-Fock treatment) would result in a Luttinger liquid phase.

strength for a specific set of wire parameters.

2.5.2 Density matrix renormalization group

We next verify the appearance of the topological phase using DMRG. As was already mentioned, the TRITOPS hosts two Majorana modes, related by time-reversal operation, at each end of the wire. We denote by $\gamma_{L(R)}$ one Majorana operator localized on the left (right) end of the wire, and by $\tilde{\gamma}_{L(R)}$ its time-reversed partner. These four Majorana operators give rise to two zero-energy fermionic operators $f_{L,R} = \gamma_{L,R} + i\tilde{\gamma}_{L,R}$. Denote by $|\Psi\rangle$ the many body ground state of the system in which both of these fermionic states are unoccupied $n_{f_R} = n_{f_L} = 0$, where $n_{f_{R(L)}} = \langle\Psi| f^\dagger_{R(L)} f_{R(L)} |\Psi\rangle$. It is clear then that the four states $|\Psi\rangle$, $f^\dagger_{L,R}|\Psi\rangle$ and $f^\dagger_L f^\dagger_R |\Psi\rangle$ are all degenerate in the thermodynamic limit. The four-fold degeneracy of the ground state is a distinct signature of the TRITOPS phase easily accessible using DMRG. Moreover, considering even and odd fermion parity sectors separately, we expect a double degeneracy in each. In a finite system, a non-vanishing overlap between the Majorana modes living on opposite ends of the wire will give rise to an energy splitting exponentially decreasing with the system size. However, the two odd fermion parity states will remain exactly degenerate for any system size due to Kramers' theorem.

A phase diagram obtained using DMRG is shown in Fig. 2.10(a). Keeping the chemical potential μ constant we vary the on-site repulsive interaction strength U. At $U = 0$ the system is in a trivial superconducting phase with a finite gap for single particle excitations. At a critical interaction strength, U_c, a phase transition occurs and the gap closes. For $U > U_c$ the gap re-opens with the system now being in the TRITOPS phase.

To obtain the phase diagram we calculate the lowest energy states and analyze the scaling of the gaps in the system as we increase its size. We take advantage of fermion parity conservation and calculate the energies in the even and odd fermion parity sectors separately. In Figs. 2.10(b-d) we present the scaling of the low-lying energy spectrum with the length of the wire at three different points in the phase diagram: one in the trivial superconducting phase, one in the TRITOPS phase and one at the critical point where the gap closes. In the trivial superconducting phase [Fig. 2.10(b)], we observe a unique ground state as expected. The gap to the first excited state extrapolates to a finite value in the limit of an infinite system. Note that this state is doubly degenerate due to Kramers' theorem, as it is in the odd fermion parity sector. The gap to the first excited state in the even fermion parity sector is nearly twice as large, as expected. At the phase transition, the gap closes. For a finite 1D system this means that the gaps should be inversely proportional to

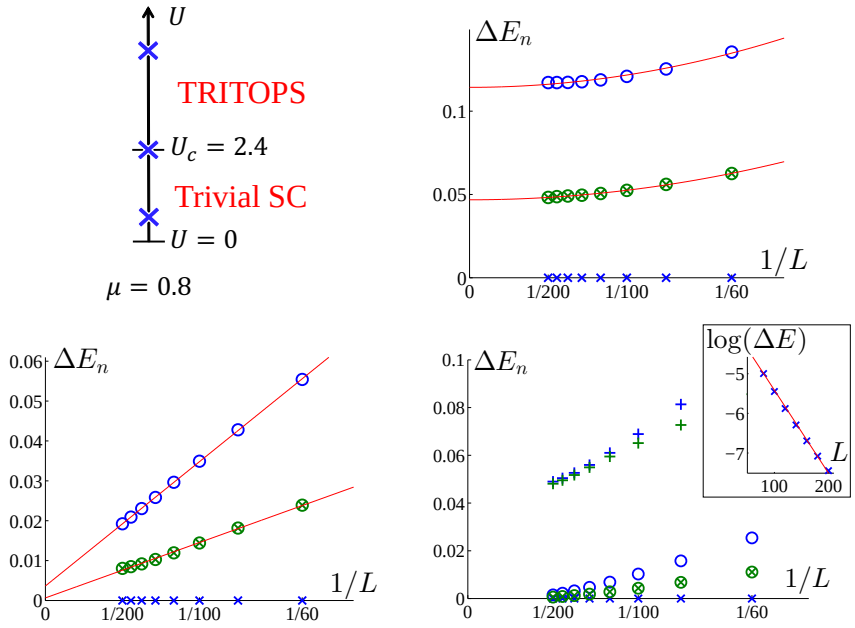

Figure 2.10: (a) Phase diagram obtained using DMRG. The system is in the trivial superconducting phase for $U < U_c$, and in the time-reversal-invariant topological superconductor (TRITOPS) phase for $U > U_c$. The system's parameters are $t_{\rm a} = t_{\rm b} = 1$, $t_{\rm ab} = 0.4$, $\alpha_{\rm a} = 0$, $\alpha_{\rm b} = 0.6$, $\Delta_{\rm ind} = 1$, $\mu = 0.8$. The low-lying energy spectrum of the system vs. $1/L$, where L is the length of the wire, for the three marked points is plotted in (b-d). Energies plotted in blue (green) correspond to energy states in the even (odd) fermion parity sectors. All energies are plotted with respect to the energy of the ground state, which is in all cases the lowest energy state in the even fermion parity sector, $\Delta E_n = E_n - E_0^{\rm even}$. (b) $U = 0.5 < U_c$. The system is in the trivial superconducting phase. The first two states in the even and odd fermion parity sectors are shown. The ground state is unique and the gap tends to a constant as $L \to \infty$, with a quadratic correction in $1/L$ as expected (the red lines are quadratic fits). The first excited state which lies in the odd parity sector is doubly degenerate as expected from Kramers' theorem. (c) $U = U_c = 2.4$. Phase transition point. Once again, the first two states in each fermion parity sector are shown. All gaps scale linearly with $1/L$ in agreement with the system being gapless in the infinite size limit (the red lines are linear fits). (d) $U = 5.5 > U_c$. The system is in the TRITOPS phase. Here, three lowest states in each fermion parity sector are shown. The result is consistent with a four-fold degenerate ground state in the thermodynamic limit, separated by a finite gap from the rest of the spectrum. The inset shows the energy difference ΔE between the lowest states in the even and odd fermion parity sectors on a semi-log scale as a function of L. The result is consistent with an exponential dependence of ΔE on the system size.

the size of the system, as can be clearly seen in Fig. 2.10(c). In the TRITOPS phase [Fig. 2.10(d)] the ground state is four-fold degenerate up to finite size splitting. The exponential dependence of the energy splitting on the length of the wire can be clearly seen from the inset. The two lowest energy states in the odd fermion parity sector indeed remain degenerate for any system size. Excited levels are separated from the ground state manifold by a finite gap.

We thus conclude that the DMRG study supports the Hartree-Fock analysis of the system confirming the appearance of the TRITOPS phase due to repulsive interactions.

2.5.3 Signature and breaking of time-reversal symmetry

In the TRITOPS phase the wire supports two MBS at each end. Measurement of differential conductance, through a lead coupled to the end of the wire, should therefore reveal those states via a peak at zero bias. At $T \to 0$ the height of the peak should be quantized to $4e^2/h$, as opposed to the TRS-broken topological superconductors in which the peak is generally quantized to $2e^2/h$ [18, 19, 76].

To explore this difference we can study the behavior of the system under the breaking of TRS, by introducing a uniform magnetic field via the Zeeman term $\mathcal{H}_B = -\vec{B} \cdot \vec{\sigma}$. When the magnetic field is applied parallel to the direction of the SOC (z in our setup), the zero-bias conductance peak (ZBCP) splits linearly with the magnetic field, as the MBS are no longer protected by TRS. In contrast, we can apply the field perpendicular to the SOC, e.g. along x. Even though TRS is now broken, the Hamiltonian still has an antiunitary symmetry $\Lambda = \sigma^x K$, expressed by $\Lambda \mathcal{H}_k \Lambda^{-1} = \mathcal{H}_{-k}$, which protects the MBS from splitting [77]. More specifically, due to this symmetry (together with PH symmetry) the Hamiltonian is in the BDI symmetry class [33] with a $\mathbb{Z}-$invariant, whose value determines the number of MBS at each end [6, 7]. In Fig. 2.5.3, we plot the number of MBS as a function of chemical potential and Zeeman field as inferred from the BDI $\mathbb{Z}-$invariant, calculated according to Ref. [77]. One should note that in reality this symmetry is fragile, as it can be broken for instance by introducing a term $\alpha_{\rm ab} \lambda^y \sigma^x \tau^z$, which describes Rashba-type SOC associated with motion transverse to the wire. In such a case, however, we still expect the splitting at small magnetic fields to be of the form [39] $\vec{B} \cdot \hat{n} + O(B^3)$, for a certain unit vector $\hat{n}$, which depends on details of the SOC. This means that as long as $\vec{B}$ is applied perpendicular to $\hat{n}$, the Zeeman splitting of the ZBCP scales as B^3 rather then linearly. This can serve as a distinct signature of the TRITOPS phase.

We next use the scattering matrix formalism to calculate the differential conductance through a single lead coupled to the system [23, 24], described by the

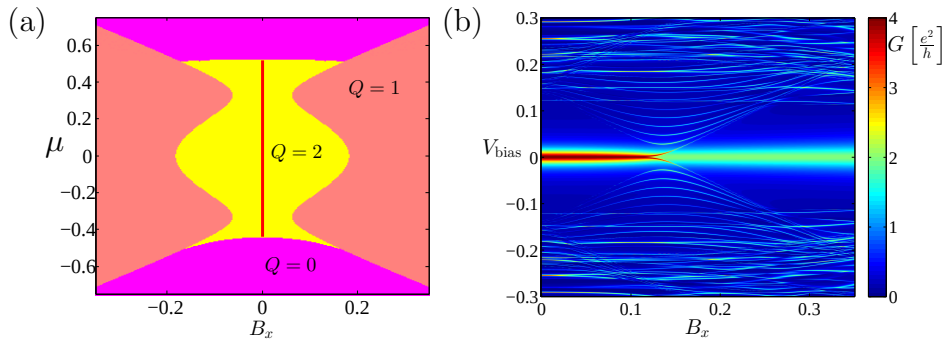

Figure 2.11: (a) Phase diagram of the Hartree-Fock Hamiltonian of Eq. (2.54) as function of chemical potential $\tilde{\mu}_{\text{a}} = \tilde{\mu}_{\text{b}} = \mu$, and Zeeman field along x (perpendicular to the SOC), for $t_{\text{a}} = t_{\text{b}} = 1, t_{\text{ab}} = 0.4, \alpha_{\text{a}} = 0, \alpha_{\text{b}} = 0.6, \tilde{\Delta}_{\text{ind}} = 0.3$ and $\tilde{\Delta}_{\text{b}} = -0.15$. The system is in symmetry class BDI, and is characterized by a $\mathbb{Z}$ invariant, Q. Q equals the number of MBS at each end of the wire. The TRITOPS phase is marked by a red line. (b) Differential conductance through a single lead connected to the wire as a function of bias voltage and Zeeman field for $\mu = 0.15$. A wire of $L = 100$ sites was used in the calculation.

Hamiltonian of Eq. (2.54) with an additional Zeeman field along x. As is evident in Fig. 2.5.3, there indeed exists a ZBCP quantized to $4e^2/h$ which does not split at low magnetic fields. As the field is further increased, a topological phase transition occurs to a phase with a single MBS at each end, at which point the ZBCP peak splits to three peaks. One of them stays at zeros-bias and is quantized to $2e^2/h$, while the other two become part of the bulk spectrum.

2.6 Discussion

In this chapter we have explored the possibility of realizing time-reversal invariant topological superconductivity (TRITOPS) in one dimension. It was concluded that, unlike the time-reversal symmetry broken topological superconductors, which can be realized in a noninteracting system coupled to a conventional SC [12–16, 41], here repulsive electron-electron interaction is a crucial ingredient. This was shown by studying the most general system of noninteracting electrons in proximity to a bulk conventional superconductor. Irrespective of any details of the electronic structure of the system and the form of its coupling to the superconductor, the system is always in a topologically trivial phase. These results have implications on the search for realizations of time-reversal invariant topological superconductors

in class DIII. In order to avoid the trivial fate of the system, one has to either invoke electron-electron interactions [46–52], or use a parent SC for which $\Delta_k \mathcal{T}_{\rm sc}$ is *not* positive semi-definite. This can either be an unconventional SC [53–55], or a combination of two SCs in a π junction* [39, 56, 57].

Following the above conclusions, we have studied the effect of electron-electron interactions in systems which are proximity-coupled to a conventional SC. We have constructed and studied a general low-energy model for a one-dimensional system, and showed that the interplay between externally-induced superconductivity and repulsive Coulomb interactions stabilizes a time-reversal invariant topological superconducting phase. This phase is characterized by a Kramers' pair of zero-energy Majorana bound state at each end of the system. This occurs since short-ranged repulsive interactions suppress the singlet component of the induced pairing potential, while strengthening the triplet component.

We have suggested two experimentally-accessible setups of proximity-coupled systems which realize this low-energy model, and which can therefore serve as a platforms for realizing time-reversal invariant topological superconductivity. These are (i) a narrow strip of a 2d topological insulator, partially covered by an s-wave superconductor, and (ii) a quasi 1d semiconductor nanowire in proximity to an s-wave superconductor. Our conclusions were corroborated in numerical simulation of a microscopic model for system (ii). Superconducting proximity effect has been established recently in both semiconducting nanowires and in topological insulators, which makes us hopeful that TRITOPS phase could be realized in these kind of system in the not too far future.

The models we have studied for realizing TRITOPS were of clean systems. We expect the excitation gap of the system to protect the topological phase against a moderate amount of disorder, namely disorder with associated mean free time which is large in comparison with the inverse energy gap. This is the case for the class-D TSC [70, 71], which can be thought of as "half" of a class-DIII TSC (namely TRITOPS).

When attempting to realize TRITOPS it is important to have a clear experimental signature of this phase. This can be accomplished by probing the Kramers' pair of Majorana bound states which reside at each end of the system. By coupling the end of the system to a normal-metal lead, the differential conductance can be measured. At zero temperature this should yield a zero-bias peak which is quantized to $4e^2/h$ [47, 53, 78]. The behavior of this conductance peak upon breaking time-reversal symmetry by a Zeeman field has features which are distinctive of a Majorana Kramers' pair [39, 47, 78]. Alternatively, current correlations in a two-

*Notice, however, that creating such a π junction requires in itself interactions or fine tuning of superconducting phases

lead setup can be used to detect signatures which are unique to Majorana bound states [79–81] (see also chapter 3). Coulomb-blockade spectroscopy, recently applied to TSC with broken TRS, can be used to probe also the TRITOPS phase, where the topological transition is expected to be manifested in the disappearance of the even-odd effect. Experimental signatures have also been suggested to exist in the anomalous behavior of Josephson junctions involving TRITOPS [82–84].

It is interesting to examine the strength of electron-electron interactions in the suggested experimental setups of Sec. 2.4. Given an estimate for the induced pairing potentials, $\Delta_{\rm s}$ and $\Delta_{\rm t}$, one can then try and place a given system on the phase diagram of Fig. 2.4 to predict whether it is in the topological or trivial phase. First we note that the Coulomb interaction between the electrons is screened by the presence of the SC. This sets a finite range for the interaction, given roughly by the lateral distance between the SC and the electrons in the system. This can be estimated as the width d of the QSHI strip (or of the wire in the case of the setup in Sec. 2.4.2). At short electron-electron distances ($|x-x'| \ll d$) the divergence of the Coulomb interaction is regularized by the finite width of the system, $V(x-x') \sim e^2/4\pi\varepsilon d$, where ε is the permittivity. If the Fermi wavelength is sufficiently larger than the interaction range d, then the forward and backward scattering interactions are of the same order,

$$g_1^{\perp}, g_2^{+}, g_2^{-} \sim d \cdot \frac{e^2}{4\pi\varepsilon d} = \frac{e^2}{4\pi\varepsilon}, \tag{2.58}$$

and accordingly the dimensionless interaction strength is $U/\pi\hbar\bar{v} \sim e^2/4\pi^2\hbar\bar{v}\varepsilon$. The velocity $\bar{v}$ depends on details such as the chemical potential. However, a reasonable estimate is $\bar{v} \sim 10^5$m/s. Takeing $\varepsilon \sim 10\varepsilon_0$ results in $U/\pi\hbar\bar{v} \sim 0.7$. Based on recent experiments [25, 27] one can estimate for the induced pairing potential, $\Delta_s \sim$ 0.1meV. The energy cutoff for the low-energy theory should be roughly given by the distance to the bottom of the band [see Figs. 2.6(c) and 2.7(c)] which again depends on the chemical potential. Looking at the phase diagram of Fig. 2.4, and assuming $\Delta_{\rm s}/\hbar\bar{v}\Lambda \sim 0.1$, we see that the system is expected to be in the topological phase for initial ratios $|\Delta_{\rm t}|/|\Delta_{\rm s}|$ greater than about 0.3.

Appendices for Chapter 2

2.A Topological Criterion

Formulas for the topological invariant of 1d Hamiltonians in class DIII were derived in several previous studies [36, 45, 47, 48, 66–68]. We shall focus here on the low-energy model described by the Hamiltonian of Eq. (2.17). Namely, we are interested in the condition on the parameters of Eq. (2.17) for which the system is in the TRITOPS phase with a Kramers pair of Majorana bound states at each end of the system. We shall use a scattering-matrix formalism to obtain a condition for the existence of a zero energy bound state [66, 85].

Let our system, which is described by $H = H_0 + H_\Delta$, extend from $x = 0$ to $x \to \infty$. We attach on the left a normal-metal stub, extending from $x = -d_N$ to $x = 0$, and described by H_0. This is depicted in Fig. 2.12. In the absence of a barrier at $x = 0$, a spin-$\uparrow$ ($\downarrow$) electron incident from the left at subgap energies is Andreev reflected as a hole with spin $\downarrow$ ($\uparrow$), with an amplitude a_+ (a_-), where [17, 86]

$$a_\pm(\varepsilon) = \frac{\varepsilon - i\sqrt{\Delta_\pm^2 - \varepsilon^2}}{\pm\Delta_\pm}, \tag{2.59}$$

for $\varepsilon \leq \Delta_\pm$, as can be checked by matching the wave functions at $x = 0$. The reflection matrix at the $x = 0$ interface is then given by

$$r_{\rm NS} = \begin{pmatrix} 0 & A^*(-\varepsilon) \\ A(\varepsilon) & 0 \end{pmatrix} \quad ; \quad A = \begin{pmatrix} 0 & a_-(\varepsilon) \\ a_+(\varepsilon) & 0 \end{pmatrix}. \tag{2.60}$$

At the end of the stub, $x = -d_N$, electrons and holes experience total normal reflection. The reflection matrix can therefore be written most generally as

$$r_{\rm N} = \begin{pmatrix} R(\varepsilon) & 0 \\ 0 & R^*(-\varepsilon) \end{pmatrix} \quad ; \quad R = \begin{pmatrix} e^{i\alpha(\varepsilon)} & 0 \\ 0 & e^{i\alpha(\varepsilon)} \end{pmatrix}, \tag{2.61}$$

where $\alpha(\varepsilon)$ is a phase which includes also the phase acquired during the propagation in the metallic region. The form of r_N is dictated by particle-hole symmetry, while

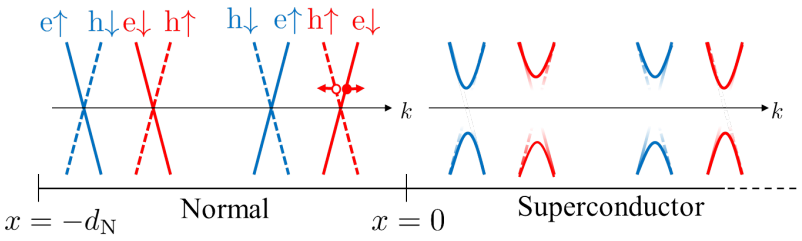

Figure 2.12: Theoretical construction for obtaining the criterion for the low-energy Hamiltonian $H = H_0 + H_\Delta$ to be in the topologically nontrivial phase [cf. Eq. (2.17)]. The semi-infinite region $x > 0$ is described by the Hamiltonian $H = H_0 + H_\Delta$, while the region $-d_N < x \leq 0$ is described by H_0. Using the scattering matrices at $x = 0$ and at $x = -d_N$ we obtain the condition for the existence of a zero-energy bound state (In fact two bound states due to Kramers' theorem), signifying that the system is in the topological phase.

the form of $R(\varepsilon)$ is dictated by time-reversal symmetry, $R(\varepsilon) = \sigma^y R^{\mathrm{T}}(\varepsilon)\sigma^y$, and by its unitarity.

Upon being reflected, once at $x = 0$ and once at $x = -d_N$, the wave function must comeback to itself. This implies a condition for the existence of a bound state

$$\det(1 - r_N r_{NS}) = 0. \tag{2.62}$$

At zero energy this reduces to

$$|1 - a_+^* a_-|^2 = 0, \tag{2.63}$$

and finally, since at zero energy $a_\pm(0) = -i\mathrm{sgn}(\Delta_\pm)$, the condition for having a zero-energy bound state is

$$\mathrm{sgn}(\Delta_+)\mathrm{sgn}(\Delta_-) = -1. \tag{2.64}$$

Notice that the power of 2 in Eq. (2.63) signifies that there are indeed *two* zero-energy solutions, these are the Kramers' pair of Majorana bound states.

2.B Self-Consistent Equations

We derive here the self-consistent mean-field equations (2.26a) and (2.26b), appearing in Sec. 2.3.1, by calculating the correlation functions in Eq. (2.25). To this end

we write the mean-field Hamiltonian, defined above Eq. (2.24), in momentum space

$$H^{\mathrm{MF}} = \sum_{|k|<\Lambda} \left\{ (R^\dagger_{k\uparrow}, L_{-k\downarrow}) \begin{pmatrix} v_+ k & \bar{\Delta}_+ \\ \bar{\Delta}_+ & -v_+ k \end{pmatrix} \begin{pmatrix} R_{k\uparrow} \\ L^\dagger_{-k\downarrow} \end{pmatrix} \right. \\ \left. + (L^\dagger_{-k\uparrow}, R_{k\downarrow}) \begin{pmatrix} v_- k & \bar{\Delta}_- \\ \bar{\Delta}_- & -v_- k \end{pmatrix} \begin{pmatrix} L_{-k\uparrow} \\ R^\dagger_{k\downarrow} \end{pmatrix} \right\}, \tag{2.65}$$

where $R_s(x) = (1/\sqrt{l}) \sum_{|k|<\Lambda} R_{ks} \exp(-ikx)$ and $L_s(x) = (1/\sqrt{l}) \sum_{|k|<\Lambda} L_{ks} \exp(-ikx)$, l being the length of the system, and Λ being the high momentum cutoff of the theory. H^{MF} can be readily diagonalized, yielding

$$H^{\mathrm{MF}} = E_{\mathrm{G}} + \sum_{|k|<\Lambda} \sum_{\tau=\pm} E_{k\tau} (\alpha^\dagger_{k\tau} \alpha_{k\tau} + \beta^\dagger_{k\tau} \beta_{k\tau}), \tag{2.66}$$

with $E_{k\pm} = \sqrt{\bar{\Delta}^2_\pm + (v_\pm k)^2}$, and with $\alpha_{k\pm}$ and $\beta_{k\pm}$ given by

$$\begin{pmatrix} \alpha_{k+} \\ \beta^\dagger_{k+} \end{pmatrix} = \begin{pmatrix} \cos\theta_{k+} & \sin\theta_{k+} \\ \sin\theta_{k+} & -\cos\theta_{k+} \end{pmatrix} \begin{pmatrix} R_{k\uparrow} \\ L^\dagger_{-k\downarrow} \end{pmatrix}, \tag{2.67a}$$

$$\begin{pmatrix} \alpha_{k-} \\ \beta^\dagger_{k-} \end{pmatrix} = \begin{pmatrix} \cos\theta_{k-} & \sin\theta_{k-} \\ \sin\theta_{k-} & -\cos\theta_{k-} \end{pmatrix} \begin{pmatrix} L_{-k\uparrow} \\ R^\dagger_{k\downarrow} \end{pmatrix}, \tag{2.67b}$$

where $\cos(2\theta_{k\pm}) = v_\pm k / \sqrt{\bar{\Delta}^2_\pm + (v_\pm k)^2}$ and $\sin(2\theta_{k\pm}) = \bar{\Delta}_\pm / \sqrt{\bar{\Delta}^2_\pm + (v_\pm k)^2}$.

By inverting Eq. (2.67), and using the fact that $\alpha_{k\pm}$ and $\beta_{k\pm}$ annihilate the ground state of H^{MF}, one obtains (at zero temperature)

$$\langle L_\downarrow(x) R_\uparrow(x) \rangle = \frac{1}{l} \sum_{|k|<\Lambda} \langle L_{-k\downarrow} R_{k\uparrow} \rangle = -\frac{1}{2l} \sum_{|k|<\Lambda} \sin(2\theta_{k+}) = \\ = -\frac{\bar{\Delta}_+}{4\pi} \int_{-\Lambda}^{\Lambda} \frac{\mathrm{d}k}{\sqrt{\bar{\Delta}^2_+ + (v_+ k)^2}} = -\frac{\bar{\Delta}_+}{2\pi v_+} \sinh^{-1}\left(v_+ \Lambda / |\bar{\Delta}_+| \right), \tag{2.68}$$

and similarly

$$\langle R_\downarrow(x) L_\uparrow(x) \rangle = -\frac{\bar{\Delta}_-}{2\pi v_-} \sinh^{-1}\left(v_- \Lambda / |\bar{\Delta}_-| \right). \tag{2.69}$$

Inserting Eqs. (2.68) and (2.69) in Eq. (2.25) results in the self-consistent equations for $\bar{\Delta}_\pm$, Eqs. (2.26a) and (2.26b).

2.C Derivation of Flow Equations

In this appendix we derive the flow equations, Eq. (2.30) in Sec. 2.3.2, by using a perturbative RG procedure. The action corresponding to the full Hamiltonian $H_0 + H_\Delta + H_{\rm int}$, specified in Eqs. (2.17) and (2.22), is given by $S = S_0 + S_\Delta + S_{\rm int}$, with

$$\begin{aligned} S_0 &= -\sum_s \int_{k,\omega} \left[(G^{\rm R}_{k\omega s})^{-1} \bar{R}_{k\omega s} R_{k\omega s} + (G^{\rm L}_{k\omega s})^{-1} \bar{L}_{k\omega s} L_{k\omega s} \right], \\ S_\Delta &= \sum_{s_1 s_2} \Delta_{s_1 s_2} \int_{k,\omega} \left(\bar{R}_{k\omega s_1} \bar{L}_{-k-\omega s_2} + L_{-k-\omega s_2} R_{k\omega s_1} \right), \\ S_{\rm int} &= \int_{1234} u^{s_1 s_2}_{s_3 s_4} \bar{R}_{k_1\omega_1 s_1} \bar{L}_{k_2\omega_2 s_2} L_{k_3\omega_3 s_3} R_{k_4\omega_4 s_4}, \end{aligned} \tag{2.70}$$

where $R_{k\omega s}$, $\bar{R}_{k\omega s}$, $L_{k\omega s}$, and $\bar{L}_{k\omega s}$ are Grassman fields, and where we have used the abbreviations

$$\int_{k,\omega} \equiv \int_{-\infty}^{\infty} \frac{{\rm d}\omega}{2\pi} \int_{-\Lambda}^{\Lambda} \frac{{\rm d}k}{2\pi}, \tag{2.71}$$

and

$$\int_{1234} \equiv (2\pi)^2 \prod_{i=1}^{4} \left(\sum_{s_i} \int_{-\Lambda}^{\Lambda} \frac{{\rm d}k_i}{2\pi} \int_{-\infty}^{\infty} \frac{{\rm d}\omega_i}{2\pi} \right) \delta(k_1 + k_2 - k_3 - k_4) \delta(\omega_1 + \omega_2 - \omega_3 - \omega_4). \tag{2.72}$$

Above we have used a compact notation for the action S, by using the Green functions $G^{\rm R,L}_{k\omega s}$ and the couplings $\Delta_{s_1 s_2}$ and $u^{s_1 s_2}_{s_3 s_4}$, which are defined by

$$G^{\eta}_{k\omega s} = (i\omega - \eta \cdot v_{\eta\cdot s} k)^{-1}, \tag{2.73a}$$

$$\Delta_{s_1 s_2} = \Delta_{\rm s} i\sigma^y_{s_1 s_2} + \Delta_{\rm t} \sigma^x_{s_1 s_2}, \tag{2.73b}$$

$$\begin{aligned} u^{s_1 s_2}_{s_3 s_4} = &- g_1^{\perp} \sigma^x_{s_1 s_2} \sigma^x_{s_2 s_3} \sigma^x_{s_3 s_4} + g_2^{\parallel} \delta_{s_1 s_2} \delta_{s_2 s_3} \delta_{s_3 s_4} \\ &+ (g_2^{+} \delta_{s_1\uparrow} + g_2^{-} \delta_{s_1\downarrow}) \sigma^x_{s_1 s_2} \delta_{s_2 s_3} \sigma^x_{s_3 s_4}. \end{aligned} \tag{2.73c}$$

On the right-hand side of Eq. (2.73a) we have used a convention where $\eta = {\rm R(L)}$ corresponds to $\eta = 1(-1)$, and $s = \uparrow(\downarrow)$ corresponds to $s = 1(-1)$.

To study the low-energy physics of the system, we iteratively integrate out the high-momentum modes within a small momentum shell, thereby obtaining an action with an effectively-decreasing cutoff, $\Lambda \exp(-\ell)$, where ℓ is the so-called RG

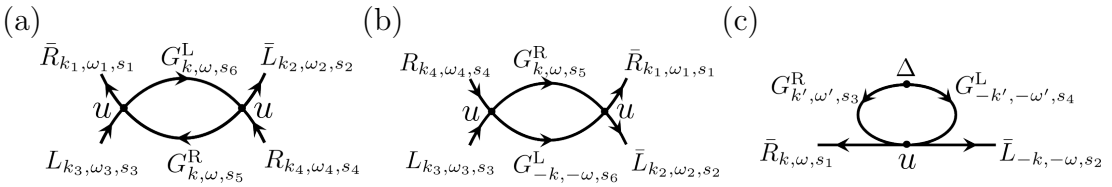

Figure 2.13: Diagrammatic representation of the second-order corrections to the S_0, appearing in Eq. (2.75). In (a) and (b) are diagrams which renormalize the interaction couplings, while in (c) is the diagram which renormalizes the induced pairing potentials. The corrections due to these diagrams are denoted by δu^{ZS} and δu^{BCS}, and $\delta\Delta$, respectively.

time [72]. We are interested in the flow of the couplings Δ_+, Δ_+, $g_1^\perp$, $g_2^\parallel$, g_2^+, and g_2^- as a function of ℓ.

At tree level, all the interaction couplings $g_1^\perp$, $g_2^\parallel$, g_2^+, and g_2^- are marginal with respect to the fixed point action S_0. The induced pairing potentials $\Delta_{\mathrm{s,t}}$ (or equivalently $\Delta_\pm$) are relevant, on the other hand, with a scaling dimension of 1. Importantly, the one-loop corrections will cause a difference in the flow of Δ_{s} and Δ_{t}.

To obtain the one-loop corrections to the flow, we treat $S' = S_\Delta + S_{\mathrm{int}}$ as a perturbation to S_0 and apply the cumulant expansion. Integrating over the fast modes, one has

$$\delta S = \frac{1}{2}\left(\langle S'\rangle^2_{0,>} - \langle S'^2\rangle_{0,>}\right), \tag{2.74}$$

where $\langle\ \rangle_{0,>}$ stands for averaging over the fast modes with respect to the unperturbed action S_0. This results in the following corrections

$$(\delta u^{\mathrm{BSC}})^{s_1s_2}_{s_3s_4} = -\sum_{s_5s_6} u^{s_1s_2}_{s_6s_5} u^{s_5s_6}_{s_3s_4} \int_{k^>,\omega} G^{\mathrm{R}}_{k,\omega,s_5} G^{\mathrm{L}}_{-k,-\omega,s_6}, \tag{2.75a}$$

$$(\delta u^{\mathrm{ZS}})^{s_1s_2}_{s_3s_4} = -\sum_{s_5s_6} u^{s_1s_6}_{s_3s_5} u^{s_5s_2}_{s_6s_4} \int_{k^>,\omega} G^{\mathrm{R}}_{k,\omega,s_5} G^{\mathrm{L}}_{k,\omega,s_6}, \tag{2.75b}$$

$$\delta\Delta_{s_1s_2} = -\sum_{s_3s_4} u^{s_1s_2}_{s_4s_3} \Delta_{s_3s_4} \int_{k^>,\omega} G^{\mathrm{R}}_{k,\omega,s_3} G^{\mathrm{L}}_{-k,-\omega,s_4}, \tag{2.75c}$$

which are described diagrammatically in Fig. 2.13. In obtaining Eqs. (2.75a,2.75b) we have set the momenta and frequencies of the outer (slow) legs [see Fig. 2.13(a,b)] to zero [72].

Finally, one can perform the frequency and momentum integration in Eq. (2.75)

and arrive at

$$\dot{g}_1^{\perp} = \frac{1}{\pi}\left(\frac{2}{v_+ + v_-}g_2^{\parallel} - \frac{1}{2v_+}g_2^{+} - \frac{1}{2v_-}g_2^{-}\right)g_1^{\perp}, \tag{2.76a}$$

$$\dot{g}_2^{\parallel} = \frac{1}{\pi(v_+ + v_-)}{g_1^{\perp}}^2, \tag{2.76b}$$

$$\dot{g}_2^{+} = -\frac{1}{2\pi v_-}{g_1^{\perp}}^2, \tag{2.76c}$$

$$\dot{g}_2^{-} = -\frac{1}{2\pi v_+}{g_1^{\perp}}^2, \tag{2.76d}$$

$$\dot{\Delta}_+ = \Delta_+ - \frac{1}{2\pi v_+}g_2^{+}\Delta_+ - \frac{1}{2\pi v_-}g_1^{\perp}\Delta_-, \tag{2.76e}$$

$$\dot{\Delta}_- = \Delta_- - \frac{1}{2\pi v_-}g_2^{-}\Delta_- - \frac{1}{2\pi v_+}g_1^{\perp}\Delta_+. \tag{2.76f}$$

Defining the average velocity, $\bar{v} = (v_+ + v_-)/2$, and the dimensionless couplings, $y_1^{\perp} = g_1^{\perp}/\pi\bar{v}$, $y_2^{+} = g_2^{+}/\pi v_+$, $y_2^{-} = g_2^{-}/\pi v_-$, and $y_2 = g_2^{+}/2\pi v_+ + g_2^{-}/2\pi v_- - g_2^{\parallel}/\pi\bar{v}$, one immediately arrives at Eq. (2.30).

As noted in the Sec. 2.3.2, we solve the flow equations up to an RG time ℓ^*, defined as the time at which one of the pairing potentials flows to strong coupling (meaning it becomes of the order of the energy cutoff). Let us assume, for example, that Δ_+ flows to strong coupling first, namely that $|\Delta_+(\ell^*)| = v_+\Lambda$. The positive-helicity degrees of freedom, $R_{k\omega\uparrow}$ and $L_{k\omega\downarrow}$ are therefore gapped and we can integrate them out. We are then left with an action containing only the negative-helicity fields $R_{k\omega\downarrow}$ and $L_{k\omega\uparrow}$,

$$\begin{aligned} S_- = \int_{k,\omega}\Big\{&-\left[(G^{\mathrm{R}}_{k\omega\downarrow})^{-1}\bar{R}_{k\omega\downarrow}R_{k\omega\downarrow} + (G^{\mathrm{L}}_{k\omega\uparrow})^{-1}\bar{L}_{k\omega\uparrow}L_{k\omega\uparrow}\right] \\ &+\Delta'_-(\ell^*)\left(\bar{L}_{k\omega\uparrow}\bar{R}_{-k-\omega\downarrow} + R_{-k-\omega\downarrow}L_{k\omega\uparrow}\right)\Big\} + g_2^{-}(\ell^*)\int_{1234}\bar{R}_{k_1\omega_1\downarrow}\bar{L}_{k_2\omega_2\uparrow}\bar{L}_{k_3\omega_3\uparrow}R_{k_4\omega_4\downarrow}, \end{aligned} \tag{2.77}$$

where to leading order in the interaction couplings

$$\begin{aligned} \Delta'_-(\ell^*) &= \Delta_-(\ell^*) + g_1^{\perp}(\ell^*)\int_{k\omega}\int_{k',\omega'}\langle L_{k\omega\downarrow}R_{k'\omega'\uparrow}\rangle_+ = \\ &= \Delta_-(\ell^*) - \frac{g_1^{\perp}(\ell^*)}{2\pi v_+}\Delta_+(\ell^*)\sinh\left[\frac{v_+\Lambda}{|\Delta_+(\ell^*)|}\right], \end{aligned} \tag{2.78}$$

and where $\langle\,\rangle_+$ stands for averaging with respect to the action containing only the positive-helicity fields. We can now continue with the RG procedure, applied to S_-,

which results in the following flow equations

$$\dot{g}_2^- = 0, \tag{2.79a}$$

$$\dot{\Delta}'_- = \left(1 - \frac{g_2^-}{2\pi v_-}\right)\Delta'_-. \tag{2.79b}$$

The flow is again stopped when Δ'_- reaches strong coupling. Importantly, the sign of the gap is determined by the sign of $\Delta'_-(\ell^*)$. The topological invariant is then given by $\nu = \mathrm{sgn}[\Delta_+(\ell^*)]\mathrm{sgn}[\Delta'_-(\ell^*)]$.

Finally, let us consider the possible interaction terms which were not included in Eq. (2.22). To this end, we first turn back attention to Eq. (2.75). We note that since the frequency integrals of Eq. (2.75) contain one right-moving green-function and one left-moving Green function, there exists poles in both the lower and upper halves of the complex frequency plane. Had the two Green functions been of the same chirality, the two poles would have been in the same half plane, resulting in a vanishing integral. We can now easily consider additional interaction terms which are also allowed by time-reversal symmetry,

$$\begin{aligned} H'_{\mathrm{int}} = \int \mathrm{d}x \big\{ & g_4^\perp \left[\rho_{\mathrm{R}\uparrow}(x)\rho_{\mathrm{R}\downarrow}(x) + \rho_{\mathrm{L}\downarrow}(x)\rho_{\mathrm{L}\uparrow}(x)\right] + g_4^+ \left[\rho_{\mathrm{R}\uparrow}(x)\rho_{\mathrm{R}\uparrow}(x) + \rho_{\mathrm{L}\downarrow}(x)\rho_{\mathrm{L}\downarrow}(x)\right] \\ & + g_4^- \left[\rho_{\mathrm{R}\downarrow}(x)\rho_{\mathrm{R}\downarrow}(x) + \rho_{\mathrm{L}\uparrow}(x)\rho_{\mathrm{L}\uparrow}(x)\right]\big\}. \end{aligned} \tag{2.80}$$

The couplings $g_4^\perp$, g_4^+, and g_4^- are marginal at tree level. Considering the above argument, any one-loop correction involving these couplings will necessarily contain a loop with two Green functions of the same chirality, and would therefore vanish. As a result, these couplings do not affect the flow of $\Delta_\pm$, $g_1^\perp$, $g_2^\pm$, and $g_2^\parallel$, nor do they flow by themselves. This is the reason for not considering H'_{int} to begin with.

2.D Nanowire Effective Hamiltonian

In this appendix we derive the low-energy Hamiltonian for a Rashba spin-orbit coupled wire in proximity to a three-dimensional s-wave SC as considered in Sec. 2.4.2. We show that it has the form of Eq. (2.48) with a momentum-dependent pairing potential $\Delta(k)$. This results in a nonvanishing triplet pairing term which, as explained in Sec. 2.3, makes the system susceptible to being driven into a topological phase in the presence of strong enough repulsive interactions.

We consider an infinite quasi one-dimensional wire with lateral dimensions $w_y \gg w_z$. As depicted in Fig. 2.7(a), the wire is placed on the surface of a conventional

s-wave SC along the x axis in the plane defined by $y = -w_y/2$. The Hamiltonian for the wire in first quantization is given by

$$\mathcal{H}_{\rm sm} = -\frac{\hat{\nabla}^2}{2m_{\rm sm}} - i\boldsymbol{\lambda}(y,z)\cdot(\boldsymbol{\sigma}\times\nabla) + V_{\rm c}(y,z) \tag{2.81}$$

where $m_{\rm sm}$ is the effective mass of electrons in the semiconductor wire, $V_{\rm c}(y,z)$ is the confining potential to be described below, and $\boldsymbol{\lambda}(y,z)$ is a spin-orbit coupling field which stems from the internal effective electric field felt by the conduction electrons in the wire. Here, $\boldsymbol{\sigma}$ is a vector of Pauli matrices in spin space. The SC is described by the Hamiltonian

$$\begin{aligned} H_{\rm sc} &= H_{\rm N} + H_{\Delta}, \\ H_{\rm N} &= \sum_{s=\uparrow,\downarrow}\int {\rm d}^3\boldsymbol{r}\,\psi_s^\dagger(\boldsymbol{r})\left[\frac{-\nabla^2}{2m_{\rm sc}} - \mu_{\rm sc}\right]\psi_s(\boldsymbol{r}), \\ H_{\Delta} &= \int {\rm d}^3\boldsymbol{r}\,\Delta_{\rm sc}\psi_\uparrow^\dagger(\boldsymbol{r})\psi_\downarrow^\dagger(\boldsymbol{r}) + {\rm h.c.}, \end{aligned} \tag{2.82}$$

where $\mu_{\rm sc}$ is the chemical potential, $m_{\rm sc}$ is the effective mass of electrons in the normal state of the SC, $\Delta_{\rm sc}$ is the superconducting gap, and $\psi_s^\dagger$ is a creation operator of electrons with spin $s =\uparrow,\downarrow$ in the SC.

Our goal is to derive an effective low-energy Hamiltonian for the semiconductor nanowire. To this end we first construct a tunneling Hamiltonian by following Bardeen's transfer Hamiltonian approach [87], and then integrate out the superconductor's degrees of freedom. As we show below, the spin-orbit coupling term in Eq. (2.81) modifies the form of the induced pair potential in the wire. Specifically, it is responsible for the emergence of a triplet pairing term in addition to the usual induced singlet pairing term. As explained in Sec. 2.3, the system is therefore more susceptible to being driven into the TRITOPS phase by repulsive interactions.

In principle, to quantitatively account for the effect of the spin-orbit coupling term, one needs to have knowledge of the functional form of $\boldsymbol{\lambda}(y,z)$. Deriving $\boldsymbol{\lambda}(y,z)$ from a microscopic theory, however, is a formidable task which we do not attempt here. Instead we shall rely on symmetry considerations, while treating $\boldsymbol{\lambda}(y,z)$ perturbatively, in order to infer its main effect on the low-energy theory.

To construct a tunneling Hamiltonian we introduce an insulating layer between the SC and the nanowire. The width of the layer is w_b and the hight of the potential barrier is V_b. The nanowire occupies the space defined by $y \in [-w_y/2, w_y/2]$, $z \in [-w_z/2, w_z/2]$, and is infinite along the x direction. The SC occupies the half space defined by $y < -(w_{\rm b} + w_y/2)$ as depicted in Fig. 2.14.

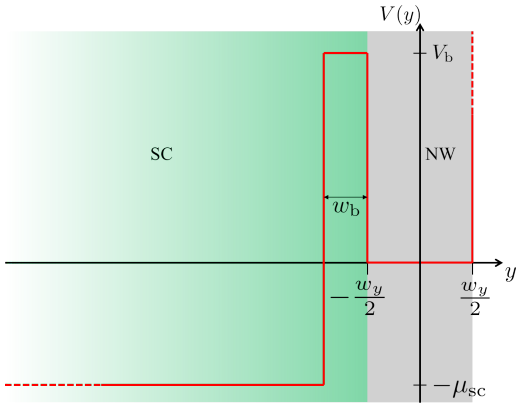

Figure 2.14: The profile of the electronic confining potential (red line) projected along the y direction for the system depicted in Fig. 2.7(a). In order to construct a tunneling Hamiltonian we consider a thin insulating layer between the nanowire and the superconductor. This is described by a potential barrier of height $V_{\rm b}$ and width $w_{\rm b}$.

Following Bardeen [87], we solve for the eigenfunctions in the nanowire $\phi_{k_x}(\boldsymbol{r})$ of the Hamiltonian $\mathcal{H}_{\rm sm}$ but with the potential barrier extended to $y \to -\infty$, and for the eigenfunctions in the normal state of the SC $\chi_{\mathbf{k}}(\boldsymbol{r})$ with the potential barrier extended to $y \to \infty$. The tunneling matrix elements are then given by

$$T_{\boldsymbol{k},k_x'} = \int \mathrm{d}^3\boldsymbol{r}\, \chi_{\boldsymbol{k}}^* \left[\mathcal{H} - E_{k_x'}\right] \phi_{k_x'}, \tag{2.83}$$

where $E_{k_x'}$ is the corresponding eigenenergy of $\phi_{k_x'}$, and $\mathcal{H}$ is the Hamiltonian with the true confining potential as depicted in Fig. 2.14.

We solve $\mathcal{H}_{\rm sm}$ in the limit of a high barrier, $\eta_{\rm b} \equiv 1/\sqrt{2m_{\rm sm}V_{\rm b}}w_y \ll 1$, and we concentrate on energies much smaller than $V_{\rm b}$. To first order in $\eta_{\rm b}$, and to zeroth order in $\boldsymbol{\lambda}(y,z)$ one has

$$\begin{aligned}\phi^{(0)}_{m,n,k_x}(\boldsymbol{r}) = &\sqrt{\frac{2}{\pi w_y w_z}} e^{ik_x x} \sin[\frac{\pi m}{w_z}(z+\frac{w_z}{2})]\times \\ &\times \begin{cases} \sin[\frac{\pi(1-\eta_{\rm b})n}{w_y}(y+\frac{w_y}{2})], & -\frac{w_y}{2} < y \le \frac{w_y}{2} \\ (-1)^n \pi n \eta_{\rm b} e^{\gamma_{\rm b}(y+w_y/2)}, & y \le -\frac{w_y}{2} \end{cases},\end{aligned} \tag{2.84}$$

with $\gamma_{\rm b} \equiv \sqrt{2m_{\rm sm}V_{\rm b}}$, and where $m, n \in \mathbb{N}$. The eigenenergies are

$$E^{(0)}_{m,n,k_x} = \frac{k_x^2}{2m_{\rm sm}} + \frac{(\pi m)^2}{2m_{\rm sm}w_z^2} + \frac{(\pi n)^2}{2m_{\rm sm}w_y^2}(1-\eta_{\rm b}). \tag{2.85}$$

The eigenfunctions of the SC in the normal state are

$$\chi_{\mathbf{k}} = \frac{1}{\sqrt{2\pi^3}} e^{i(k_x x + k_z z)} \times \begin{cases} e^{ik_y(y+\frac{w_y}{2}+w_{\rm b})} + \frac{ik_y+\gamma_{\rm b}}{ik_y-\gamma_{\rm b}} e^{-ik_y(y+\frac{w_y}{2}+w_{\rm b})}, & y < -\frac{w_y}{2} \\ \frac{2ik_y}{ik_y-\gamma_{\rm b}} e^{-\gamma_{\rm b}(y+\frac{w_y}{2}+w_{\rm b})}, & y \geq -\frac{w_y}{2} \end{cases} . \quad (2.86)$$

We now turn to the first-order corrections of both the energies and the wave functions in the nanowire due to spin-orbit coupling. From symmetry considerations we can infer that $\lambda_x = 0$. To see this we first note that the vector field $\boldsymbol{\lambda}$ stems from the electric field in the wire. Since the system is translationally invariant and symmetric under mirror reflection $x \to -x$, the field component λ_x must be zero. Moreover, since the system is symmetric under $z \to -z$, we must have $\lambda_z(y,-z) = -\lambda_z(y,z)$. Taking into account the fact that the wave functions $\phi^{(0)}_{m,n,k_x}$ have a definite parity under $z \to -z$, the first-order correction to the energies is given by

$$E^{(1)}_{m,n,k_x,s} = \langle \phi^{(0)}_{m,n,k_x} | -i\boldsymbol{\lambda}\cdot(\boldsymbol{\sigma}_{ss}\times\nabla) | \phi^{(0)}_{m,n,k_x} \rangle = \langle \phi^{(0)}_{m,n,k_x} | \lambda_y | \phi^{(0)}_{m,n,k_x} \rangle k_x s \equiv \alpha k_x s. \quad (2.87)$$

where $s = 1$ for spin $\uparrow$, and $s = -1$ for spin $\downarrow$. We note that this term vanishes for a system with a symmetry $y \to -y$. It is the breaking of this symmetry by the SC which allows for a nonzero α. This is the usual term considered in one-dimensional Rashba systems [15, 16].

We now wish to obtain a correction to the wave functions. We concentrate on the lowest transverse band, namely $m, n = 1$, which is justified for a thin wire. We make use of the limit $w_z \ll w_y$, and accordingly consider only the correction due to the second lowest transverse band $|\phi_{1,2,k_x}\rangle$,

$$|\phi^{(1)}_{1,1,k_x}\rangle = \frac{\langle \phi^{(0)}_{1,2,k_x}| - i\boldsymbol{\lambda}\cdot(\boldsymbol{\sigma}\times\nabla)|\phi^{(0)}_{1,1,k_x}\rangle}{E^{(0)}_{1,1,k_x} - E^{(0)}_{1,2,k_x}} |\phi^{(0)}_{1,2,k_x}\rangle. \quad (2.88)$$

Invoking once more the symmetry $\lambda_z(y,-z) = -\lambda_z(y,z)$, one obtains to first order

$$|\phi_{1,1,k_x}\rangle = |\phi^{(0)}_{1,1,k_x}\rangle + \frac{1}{2}\beta k_x \sigma^z |\phi^{(0)}_{1,2,k_x}\rangle, \quad (2.89)$$

where for the sake of brevity we have defined

$$\beta = \frac{8 m_{\rm sm} w_y^2 \langle \phi^{(0)}_{1,1,k_x} | \lambda_y | \phi^{(0)}_{1,2,k_x} \rangle}{3\pi^2}. \quad (2.90)$$

This term survives even if the system is symmetric under $y \to -y$, i.e. its existence does not rely on a substrate which breaks inversion symmetry. Its main effect is to

push the wave functions either towards or away from the SC, depending on the sign of $k_x\sigma^z$ [75].

We now plug Eq. (2.89) and Eq. (2.87) into Eq. (2.83) to obtain the matrix elements between modes in the SC and modes in the nanowire. We invoke the limit of a high barrier in which the energies of all the modes are smaller than $V_{\rm b}$, and further assume $k_z w_z \ll 1$. This yields

$$T_{\boldsymbol{k},k_x'} = t_{\boldsymbol{k}}\delta(k_x - k_x') \quad ; \quad t_{\boldsymbol{k}} = t_0 \cos\Theta_{\boldsymbol{k}}(1 + \frac{1}{2}\beta k_x'\sigma^z), \tag{2.91}$$

with

$$t_0 = \frac{4i|k|}{m_{\rm sm}^2 w_y V_{\rm b}}\sqrt{\frac{w_z}{w_y}}e^{-\gamma_{\rm b} w_b}, \tag{2.92}$$

and with $\cos\Theta_{\boldsymbol{k}} \equiv k_y/|k|$. Apparently the effect of the inversion-symmetric part of λ_y (which is the source of β) is to introduce a term $k_x\sigma^z$ in the coupling between the wire and the SC. The presence of the factor $\cos\Theta_{\boldsymbol{k}}$ stems simply from the fact that modes which approach the surface of the SC at small angles have a higher probability to tunnel into the wire.

We can now write the full tunneling Hamiltonian of the system as

$$\begin{aligned}
&H = H_{\rm sm} + H_{\rm sc} + H_{\rm T},\\
&H_{\rm sm} = \frac{1}{2}\int {\rm d}k_x \Phi_{k_x}^\dagger \mathcal{H}_{\rm sm}^{\rm BdG}(k_x)\Phi_{k_x},\\
&H_{\rm sc} = \frac{1}{2}\int {\rm d}^3\boldsymbol{k} \Psi_{\boldsymbol{k}}^\dagger \mathcal{H}_{\rm sc}^{\rm BdG}(\boldsymbol{k})\Psi_{\boldsymbol{k}},\\
&H_{\rm T} = \frac{1}{2}\int {\rm d}^3\boldsymbol{k}\, t_{\boldsymbol{k}} \Psi_{\boldsymbol{k},s}^\dagger \Phi_{k_x},\\
&\mathcal{H}_{\rm sm}^{\rm BdG}(k_x) = (\varepsilon_{k_x} - \mu_{\rm sm} + \alpha k_x\sigma^z)\tau^z,\\
&\mathcal{H}_{\rm sc}^{\rm BdG}(\boldsymbol{k}) = \xi_{\boldsymbol{k}}\tau^z + \Delta_{\rm sc}\tau^x,
\end{aligned} \tag{2.93}$$

where $\xi_{\boldsymbol{k}} = \boldsymbol{k}^2/2m_{\rm sc} - \mu_{\rm sc}$, $\varepsilon_{k_x} = k_x^2/2m_{\rm sm} - \mu_{\rm sm}$, and with $\Phi_{k_x'} = (c_{k_x\uparrow}^\dagger, c_{k_x\downarrow}^\dagger, c_{-k_x\downarrow}, -c_{-k_x\uparrow})$, $\Psi_{\boldsymbol{k}} = (f_{\boldsymbol{k}\uparrow}^\dagger, f_{\boldsymbol{k}\downarrow}^\dagger, f_{-\boldsymbol{k}\downarrow}, -f_{-\boldsymbol{k}\uparrow})$. Here, $c_{k_x s}^\dagger$ create a spin-s electron in the state $\phi_{1,1,k_x}$ of the wire, and $f_{\boldsymbol{k}s}^\dagger$ creates a spin-s electron in the state $\chi_{\boldsymbol{k}}$ of the SC. $\{\tau^i\}_{i=x,y,z}$ is a set of Pauli matrices in particle-hole space.

To obtain an effective Hamiltonian for the wire we integrate out the superconductor's degrees of freedom. [34, 51, 88, 89]. The self-energy term which adds to $\mathcal{H}_{\rm sm}^{\rm BdG}(k_x)$ is given by

$$\Sigma(\omega, k_x) = \int {\rm d}k_y {\rm d}k_z\, t_{\boldsymbol{k}} G_{\rm sc}(\omega, \boldsymbol{k}) t_{\boldsymbol{k}}^*, \tag{2.94}$$

where $G_{\rm sc}(\omega,\boldsymbol{k})$ is the Green function of the bare SC, given by

$$G_{\rm sc}(\omega,\boldsymbol{k})=\frac{\omega+\xi_{\boldsymbol{k}}\tau^z-\Delta_{\rm sc}\tau^x}{\omega^2-\xi_{\boldsymbol{k}}^2-\Delta_{\rm sc}^2}. \tag{2.95}$$

To perform the integral in (2.94) we use the fact that $\mu_{\rm sc}$ is typically much bigger than the relevant energy scale in the semiconductor wire, so we can neglect $k_x^2/2m_{\rm sc}$ with compare to $\mu_{\rm sc}$. For the same reason we also have $\mu_{\rm sc}\gg\omega$ which means that the main contribution to the integral comes from momenta satisfying $(k_y^2+k_z^2)/2m_{\rm sc}\simeq\mu_{\rm sc}$. With the help of these simplifications one obtains to first order in β

$$\Sigma(\omega,k_x)=\frac{\nu_{2d}|t_0|^2(-\omega+\Delta_{\rm sc}\tau^x)}{\sqrt{\Delta_{\rm sc}^2-\omega^2}}(1+\beta k_x\sigma^z), \tag{2.96}$$

where ν_{2d} is the density of states of a two-dimensional system with an effective mass $m_{\rm sc}$ at a chemical potential $\mu_{\rm sc}$.

Finally, in case one concentrates on energies much smaller than the bare superconducting gap (namely $\omega\ll\Delta_{\rm sc}$), the self-energy becomes independent of ω and the effective low-energy Hamiltonian is given by

$$\mathcal{H}_{\rm sm}^{\rm eff}=(\varepsilon_{k_x}+\alpha k_x\sigma^z)\tau^z+\Delta_{\rm ind}(1+\beta k_x\sigma^z)\tau^x, \tag{2.97}$$

with $\Delta_{\rm ind}=\nu_{2d}|t_0|^2$.

2.E Local Stability to Spin-Density Waves

As mentioned in Sec. 2.5.1, one wishes to examine the stability of the topological phase to other competing phases, which were not accounted for in the Hartree-Fock treatment. Specifically, until now we did not allow for the possibility that the system spontaneously breaks the lattice translational symmetry, and develops spin-density waves. To examine this possibility, one should consider the following more general Hartree-Fock Hamiltonian:

$$H^{\rm HF}(\phi)=H^{\rm HF}(0)-\sum_{\nu,q,s}\phi_{\nu-qs}\hat{\rho}_{\nu qs}, \tag{2.98}$$

where $\hat{\rho}_{\nu qs}$ is the Fourier transform of $\hat{n}_{\nu is}=c^\dagger_{\nu is}c_{\nu is}$, given by $\hat{\rho}_{\nu qs}=\frac{1}{\sqrt{L}}\sum_k c^\dagger_{\nu k+qs}c_{\nu ks}$, $\phi_{\nu qs}$ are fields which in general should be determined by the Hartree-Fock procedure, and $H^{\rm HF}(0)$ is the same as the Hamiltonian of Eq. (2.54). We now ask whether having nonvanishing fields, $\phi_{\nu qs}$, can cause the expectation value of the full Hamiltonian

$\langle H\rangle_{\rm HF,\phi} \equiv \langle \Psi_{\rm HF}(\phi)\,|H|\,\Psi_{\rm HF}(\phi)\rangle$ to decrease, assuming that these fields are small. If this is the case then our previous Hartree-Fock solution is locally unstable to the formation of spin-density waves. In other words, for the solution to be locally stable, $\langle H\rangle_{\rm HF,\phi}$ must have a minimum at $\phi_{\nu,q,s}=0$. This is the case if the Hessian matrix $\partial^2\langle H\rangle_{\rm HF,\phi}/\partial\phi_{\nu',q,s'}\partial\phi_{\nu,-q,s}|_{\phi=0}$ is positive definite.

We start by rewriting the expression for $\langle H\rangle_{\rm HF,\phi}$,

$$\langle H\rangle_{\rm HF,\phi} = \langle H_0\rangle_{\rm HF,\phi} + \frac{1}{L}\sum_\nu U_\nu\left(N_{\nu,\uparrow}N_{\nu,\downarrow}+|P_\nu|^2\right)+\sum_\nu U_\nu\sum_{q\neq 0}\rho_{\nu,q\uparrow}\rho_{\nu,-q\downarrow}, \quad (2.99)$$

where $\rho_{\nu,qs}\equiv\langle\hat\rho_{\nu,qs}\rangle_{\rm HF,\phi}$. We now write H_0 as

$$H_0 = H^{\rm HF}(\phi)+\sum_\nu\delta\mu_\nu\sum_{k,s}c^\dagger_{\nu,k,s}c_{\nu,k,s}-\sum_\nu\delta\Delta_\nu\sum_k\left(c^\dagger_{\nu,k\uparrow}c^\dagger_{\nu,-k\downarrow}+h.c.\right)+\sum_{\nu,q\neq0,s}\phi_{\nu-qs}\hat\rho_{\nu qs}, \quad (2.100)$$

where we have defined $\delta\mu_\nu\equiv\tilde\mu_\nu-\mu_\nu$, $\delta\Delta_{\rm a}\equiv\tilde\Delta_{\rm ind}-\Delta_{\rm ind}$, and $\delta\Delta_{\rm b}\equiv\tilde\Delta_{\rm b}-\Delta_{\rm b}$. Inserting this into Eq. (2.99), one has

$$\langle H\rangle_{\rm HF,\phi} = \langle H^{\rm HF}(\phi)\rangle_{\rm HF,\phi}+\sum_\nu N_\nu\left(\frac{U_\nu}{L}N_\nu+2\delta\mu_\nu\right)+\sum_\nu P_\nu\left(\frac{U_\nu}{L}P_\nu-2\delta\Delta_\nu\right)+$$
$$+\sum_{\nu,q\neq0}\left(U_\nu\rho_{\nu,-q\downarrow}\rho_{\nu,q\uparrow}+\sum_s\phi_{\nu-qs}\rho_{\nu qs}\right). \quad (2.101)$$

In the last step we have used the fact that due to TRS, $N_{\nu,\uparrow}=N_{\nu,\downarrow}\equiv N_\nu$ and $P^*_\nu=P_\nu$. To perform the derivative of the first term, we exploit the Hellmann-Feynman theorem

$$\frac{\partial\langle H^{\rm HF}(\phi)\rangle_{\rm HF,\phi}}{\partial\phi_{\nu,q,s}}=\left\langle\frac{\partial H^{\rm HF}(\phi)}{\partial\phi_{\nu,q,s}}\right\rangle_{\rm HF,\phi}=-\rho_{\nu,-q,s} \quad (2.102)$$

We now invoke linear response theory:

$$\rho_{\nu,q,s}=\sum_{\nu'}\chi^{\nu'}_{q,\nu,s}\phi_{q,\nu',s}. \quad (2.103)$$

Note that due to s^z conservation, there is no response of $\rho_{\nu,q,\uparrow}$ to $\phi_{q,\nu',\downarrow}$ and vice versa. We next perform the second derivative of $\langle H\rangle_{\rm HF,\phi}$, and we note that the

second and third terms in Eq. (2.101) then vanish as a result of the self-consistent equations for $\delta\mu_\nu$ and $\delta\Delta_\nu$. One then obtains $\langle H\rangle_{\mathrm{HF},\phi}$ to second order in ϕ

$$\langle H\rangle_{\mathrm{HF},\phi} = \tfrac{1}{2}\sum_{q\neq 0} \vec{\phi}^T_{-q} h_q \vec{\phi}_q \quad , \quad \vec{\phi}^T_q = \begin{pmatrix}\phi_{qa\uparrow} & \phi_{qb\uparrow} & \phi_{qa\downarrow} & \phi_{qb\downarrow}\end{pmatrix}, \tag{2.104}$$

where h_q is Hessian matrix, given by

$$\begin{aligned} h_q &= \begin{pmatrix} A_q & B_q \\ B_q & A_q \end{pmatrix} \quad ; \quad A_q = \begin{pmatrix} \chi_{\mathrm{aa},q} & \chi^*_{\mathrm{ab},q} \\ \chi_{\mathrm{ab},q} & \chi_{\mathrm{bb},q} \end{pmatrix} \\ B_q &= \begin{pmatrix} U_{\mathrm{a}}\chi^2_{\mathrm{aa},q} + U_{\mathrm{b}}|\chi_{\mathrm{ab},q}|^2 & \chi^*_{\mathrm{ab},q}\left(U_{\mathrm{a}}\chi_{\mathrm{aa},q} + U_{\mathrm{b}}\chi_{\mathrm{bb},q}\right) \\ \chi_{\mathrm{ab},q}\left(U_{\mathrm{a}}\chi_{\mathrm{aa},q} + U_{\mathrm{b}}\chi_{\mathrm{bb},q}\right) & U_{\mathrm{a}}|\chi_{\mathrm{ab},q}|^2 + U_{\mathrm{b}}\chi^2_{\mathrm{bb},q} \end{pmatrix}. \end{aligned} \tag{2.105}$$

In writing Eq. (2.104) and Eq. (2.105), we made use of the fact that due to TRS $\chi^{\nu'}_{\nu,q,\uparrow} = \chi^{\nu}_{\nu',-q,\downarrow} \equiv \chi_{\nu,\nu',q}$, as well as of $\chi^*_{\nu,\nu',-q} = \chi_{\nu,\nu',q}$.

We calculate the susceptibilities using the Kubo Formula:

$$\chi^{\nu'}_{\nu,q,s} = -i\int_{-\infty}^{\infty} \theta(t)\left\langle[\hat{\rho}_{-q,\nu,s}(0), \hat{\rho}_{q,\nu',s}(t)]\right\rangle_{\mathrm{HF}} dt, \tag{2.106}$$

and obtain

$$\begin{aligned} \chi_{\mathrm{aa},q} &= \frac{1}{L}\sum_k \sum_{i,j=1}^{2} \frac{|u_{1i}(k)|^2|v_{1j}(k+q)|^2 + |u_{1j}(k+q)|^2|v_{1i}(k)|^2}{\epsilon_{k,i} + \epsilon_{k+q,j}}, \\ \chi_{\mathrm{bb},q} &= \frac{1}{L}\sum_k \sum_{i,j=1}^{2} \frac{|u_{2i}(k)|^2|v_{2j}(k+q)|^2 + |u_{2j}(k+q)|^2|v_{2i}(k)|^2}{\epsilon_{k,i} + \epsilon_{k+q,j}}, \\ \chi_{\mathrm{ab},q} &= \frac{1}{L}\sum_k \sum_{i,j=1}^{2} \frac{u_{1i}(k)u^*_{2i}(k)v^*_{1j}(k+q)v_{2j}(k+q) + u^*_{1j}(k+q)u_{2j}(k+q)v_{1i}(k)v^*_{2i}(k)}{\epsilon_{k,i} + \epsilon_{k+q,j}}. \end{aligned} \tag{2.107}$$

Finally, we use Eqs. (2.107) to numerically check that h_q in Eq. (2.105) is positive definite (i.e. that all its eignevalues-values are positive) for all q's as a condition for local stability. The unstable region can be seen in the phase diagram, Fig. 2.9

Chapter 3

Signatures of Majorana Zero Modes

3.1 Introduction

The interest in phases which host zero-energy Majorana bound states (MBSs) stems largely from their topological nature; such a state stores information nonlocally. Stated otherwise, one cannot make a local measurement which would reveal whether the MBS is occupied or empty. A consequence of this property is that such systems are insensitive to local perturbations [11]. As a result, if we treat the filled and empty states as a quantum bit (Qbit), then this Qbit is immune to decoherence by the environment, as the latter interacts *locally* with the system[†]. Realizing MBSs in topological superconductor is therefore appealing, not only from a theoretical point of view, but also from the point of view of applications to quantum information processing.

Experimentally realizing MBSs would of course be meaningless in the absence of a physical signature that could reveal their presence. In particular, it is important to be able to discern between MBSs and other low-energy resonances which can give rise to similar phenomenology. From a more fundamental point of view, an important measure of our understanding of a physical system is our ability to make predictions of its behavior under controlled conditions. In the context of MBSs, it is especially interesting to be able to probe and witness its nonlocal nature in order to better understand this exotic feature.

Much emphasis has been put on signatures of MBSs in transport studies, involving a normal lead coupled to an MBS. It is predicted that the differential conduc-

[†]So-called classical errors, in which the occupation flips from 0 to 1 are protected by conservation of fermion-number parity.

tance will exhibit a zero-bias conductance peak (ZBCP) which, at zero temperature, is quantized to $2e^2/h$ [18–21]. Recently, several experimental studies have reported the observation of such a ZBCP, in both semiconductor nanowires [25–29] and in Ferromagnetic atomic chains [42–44]*. While these experiments are promising, it has been suggested that the ZBCP can also appear in the absence of a MBS as a result of other mechanisms [91–96]. Moreover, the quantization of the ZBCP to $2e^2/h$ has proved difficult to observe, as it requires the temperature to be much lower than the width of the peak. It is therefore crucial to have a physical signature beyond the ZBCP, in particular one which would survive at finite temperatures.

In this chapter we investigate signatures of MBSs which are related to their nonlocal nature. This has the advantage of both being unique to MBSs, as well as probing one of their fundamental properties. In Secs. 3.2 and 3.3 we examine a setup which we term *Majorana beam splitter*. In this setup a single MBS is coupled to multiple normal leads which are biased at a voltage V with respect to the topological superconductor hosting the MBS. We study the cross correlations of the currents in the leads, showing that it has universal features which stems from the Majorana nonlocality and it self-hermitian nature. The cross correlation is negative and decays as $-1/V$ at high voltages. This effect survives, to a large extent, at finite temperatures. We begin in Sec. 3.2 by concentrating on the special case of spin-resolved current, where the physical idea is most intuitive and where the distinction between MBSs and low-energy Andreev bound states (ABSs) is most pronounced. We then generalize in Sec. 3.3 to the case of a general Majorana beam splitter in which the current does not have to be resolved into its spin components. Finally, in Sec. 3.4 we examine the case of a finite-size topological superconductor. As the two MBSs at each end become (weakly) coupled, local observable, such as charge and spin density, can distinguish between the two states of the Majorana Qbit. We show that the behavior of the charge density as a function of magnetic field or gate potential can serve as a signature of the two weakly-coupled MBSs.

3.2 Spin-Resolved Current Cross Correlations

In this section, we discuss the signatures of MBSs in spin-resolved current correlations. Consider a normal metallic lead coupled to a topological superconductor with a MBS at its end. A bias voltage is applied between the lead and the superconductor, driving a current from the lead. We are interested in the spin-resolved current

*Very recently signatures of topological superconductivity have been observed in Coulomb-blockade oscillations experiments on semiconductor nanowires [90].

correlations in the lead, defined as

$$P_{ss'} = \int_{-\infty}^{\infty} dt \langle \delta\hat{I}_s(0)\delta\hat{I}_{s'}(t)\rangle, \quad \delta\hat{I}_s = \hat{I}_s - \langle\hat{I}_s\rangle, \tag{3.1}$$

where $\hat{I}_s$ is the spin-s current operator ($s =\uparrow,\downarrow$), and the angle brackets stand for thermal quantum averaging*. We concentrate on the cross correlation term $P_{\uparrow\downarrow}$ and compare between two cases: with a MBS present, and with an "accidental" low-energy Andreev bound state (ABS) but without a MBS. Both cases lead to a similar ZBCP.

As we will show, in the presence of a MBS, the cross term $P_{\uparrow\downarrow}$ carries unique signatures, that are strikingly different from the case of an ABS: In the MBS case, $P_{\uparrow\downarrow}$ is negative in sign, and approaches zero as $P_{\uparrow\downarrow} \propto -1/V$ with increasing bias voltage V. In contrast, an ABS generically gives rise to a positive $P_{\uparrow\downarrow}$, that approaches a nonzero constant at high voltages. These distinctive features survive, to a large extent, at finite temperatures. As long as the temperature T is smaller than eV, $P_{\uparrow\downarrow}$ is only weakly temperature dependent, even if $T > \Gamma$, Γ being the width of the low-energy resonance (either an ABS or a MBS). This is in contrast to the zero-bias peak in the differential conductance spectrum which is only quantized to $2e^2/h$ for $T \ll \Gamma$. Notice that a low-energy ABS can be viewed as a pair of overlapping MBSs. Crucially, however, unlike the case of two spatially separated MBSs, in this case both MBSs are coupled to the lead with comparable strengths. This is essentially the source of the difference in the phenomenology of the two cases.

As a prototypical setup for measuring this effect, we consider a long semiconductor nanowire proximity coupled to a conventional bulk s-wave superconductor (see Fig. 3.1). Under the right conditions, a MBS is formed at the end of the wire [15, 16]. The wire is tunnel coupled to a normal lead forming a T junction; a bias voltage is applied between the lead and the superconductor. To allow for the measurement of spin-resolved currents, at each arm of the T junction there is a "spin filter" that transmit only electrons of a certain spin polarization. There are several physical ways in which one can think of implementing such spin filters. By locating gates underneath each of the two normal legs of the junction two quantum dots can be defined. By varying the gate potential under the dot, one can tune a level of a certain spin to be at resonance, thereby filtering the spin-resolved current through that leg†. If the two dots are tuned to opposite spin resonances, $P_{\uparrow\downarrow}$ can be obtained

*We note that the zero-frequency correlation matrix is symmetric, namely $P_{\uparrow\downarrow} = P_{\downarrow\uparrow}$. A proof can be found in Appendix B of Anantram *et al.* [97].

†The width of the resonance has to be comparable with the voltage range of interest. Since B is commonly larger than the excitation gap, this can be achieved without allowing transmission of opposite spins.

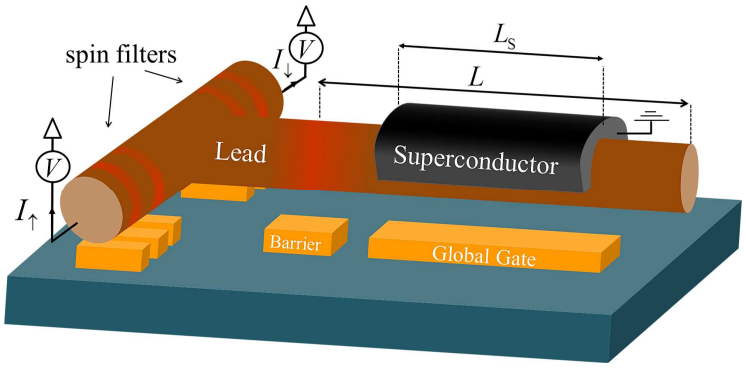

Figure 3.1: A semiconductor nanowire proximity coupled to an s-wave superconductor. Under certain conditions the system hosts Majorana bound states at its ends. The system is tunnel coupled on the left to a normal lead which is biased at a voltage V. The correlations between the spin-resolved currents ($I_\uparrow$ and $I_\downarrow$) in the normal lead have features which are unique to the Majorana bound state. The correlation is negative and approaches zero as $-1/V$ for eV larger than the Majorana resonance width (but still smaller then the superconducting gap). To measure these correlations we suggest implementing the system in a T-shaped junction and placing a "spin filter" at each of the arms of the T. This may be done by defining quantum dots using gate voltages. In the presence of a magnetic field the resonance level of each dot can be tuned by back gates to have opposite spins. In sec. 3.3 we generalize our result to the case of a general beam splitter where the spin filter are absent.

by measuring correlations between the currents through the two normal legs. Alternatively, spin filters can be constructed by coupling the normal legs to oppositely polarized ferromagnets [21] or to a quantum spin Hall insulator [5, 31, 32, 98].

3.2.1 Intuitive analysis

The behavior of $P_{\uparrow\downarrow}$ can be understood from qualitative considerations. We assume that the bias voltage is smaller than the gap of the superconductor, such that only Andreev reflection [17] in the lead contributes to the conductance. Consider first the case $eV \gg \Gamma$. In this limit one can discuss sequential single-particle tunneling events. As Cooper pairs are transported from the superconductor to the lead, they split such that one electron goes to the lead while the other electron changes the

occupation of the low-energy resonance*.

A change in the occupation number of an ordinary ABS is generically accompanied by a change in local physical observables near the edge, e.g., the local spin and charge densities. As a result, the spin density near the edge changes each time an electron is transmitted and the spin of the transmitted electron tends to be antialigned with the spin of the preceding transmitted electron. (If the z component of the spin is conserved, this correlation is perfect.) Such a correlation corresponds to $P_{\uparrow\downarrow} > 0$.

On the other hand, a change in the occupation number of a MBS cannot be detected in *any* local observable near a single edge. In particular, the local spin densities of the two degenerate ground states (associated with the occupation number of the fermion formed by the MBSs at the two ends) are identical†. It follows that the spins of consecutive electrons are uncorrelated; hence $P_{\uparrow\downarrow} \to 0$.

The low-voltage behavior of the result in Eq. (3.24) can also be understood from simple considerations based on the properties of MBSs. For $eV \ll \Gamma$ and at zero temperature the conductance through the MBS is quantized to $2e^2/h$, resulting in an overall *noiseless* current‡. Upon splitting the current into the two parts $I_\uparrow$ and $I_\downarrow$, the total noise P is related to the cross correlation via $P = P_\uparrow + P_\downarrow + 2P_{\uparrow\downarrow}$, where $P_\uparrow$ and $P_\downarrow$ are the current noises of electrons with spin-$\uparrow$ and spin-$\downarrow$, respectively. Since $P \to 0$ at low voltage, while $P_\uparrow$ and $P_\downarrow$ are non-negative by definition, one must have $P_{\uparrow\downarrow} \leq 0$. More specifically, at zero voltage the total noise obeys [99] $dP/dV|_{V=0} = 0$. In addition, since (for zero temperature) $P_\uparrow(0) = P_\downarrow(0) = 0$, one has $dP_\uparrow/dV|_{V=0}, dP_\downarrow/dV|_{V=0} \geq 0$. It therefore follows that $dP_{\uparrow\downarrow}/dV|_{V=0} \leq 0$. The cross correlation $P_{\uparrow\downarrow}$ is thus negative at low voltage.

3.2.2 Low-energy models

With this qualitative picture in mind, we calculate $P_{\uparrow\downarrow}$ for a general low-energy model $H = H_{\rm L} + H_{\rm T}$ of a normal lead coupled to a MBS, where§

$$H_{\rm L} = \sum_{k,s} \epsilon_k \psi^\dagger_{ks} \psi_{ks} \quad ; \quad H_{\rm T} = i\gamma \cdot \sum_{k,s} (t_s \psi_{ks} + \text{h.c.}). \tag{3.2}$$

*Note that this process can happen more than once since charge is not conserved in the superconductor.

†Formally this reads $\langle 0|\mathbf{s}(x)|0\rangle = \langle 1|\mathbf{s}(x)|1\rangle$, where $\mathbf{s}(x)$ is the spin density and $|0\rangle, |1\rangle$ are the two degenerate ground states.

‡More specifically, the reflection matrix contains one channel which perfectly Andreev reflects, while the rest of the channels have perfect normal reflection in the weak coupling limit, $\Gamma \ll \Delta$, where Δ is the energy gap to the next excitation.

§Although we consider here a single-channel lead, our conclusions extend to a multichannel lead (see Sec. 3.3).

Here ψ_{ks} describes the lead modes with spin s, ϵ_k are the energy levels in the lead, and t_s is the coupling constant of these modes to the Majorana state described by γ. The form of H is quite general and stems solely from the Hermitian nature of γ.

At energies below the superconducting gap only reflection processes are possible, and the reflection matrix is given by [100, 101]

$$r_{\rm tot} = \begin{pmatrix} r^{\rm ee} & r^{\rm eh} \\ r^{\rm he} & r^{\rm hh} \end{pmatrix} = 1 - 2\pi i W^\dagger \left(\varepsilon + i\pi W W^\dagger\right)^{-1} W, \tag{3.3}$$

with $W = \sqrt{\nu_0}(t_\uparrow, t_\downarrow, t_\uparrow^*, t_\downarrow^*)$, and where ν_0 is the density of states in the lead. This yields

$$r^{\rm ee}_{ss'} = \delta_{ss'} + \frac{2\pi\nu_0 t_s^* t_{s'}}{i\varepsilon - \Gamma} \quad , \quad r^{\rm he}_{ss'} = \frac{2\pi\nu_0 t_s t_{s'}}{i\varepsilon - \Gamma} \tag{3.4}$$

where $r^{\rm hh}(\varepsilon) = [r^{\rm ee}(-\varepsilon)]^*$, $r^{\rm eh}(\varepsilon) = [r^{\rm he}(-\varepsilon)]^*$ as dictated by particle-hole symmetry, and $\Gamma = 2\pi\nu_0(|t_\uparrow|^2 + |t_\downarrow|^2)$.

The spin-resolved currents and their correlation functions are given by [97]

$$\begin{aligned}
\langle \hat{I}_s \rangle &= \frac{e}{h} \sum_{\substack{s'\in\uparrow,\downarrow \\ \alpha,\beta\in e,h}} {\rm sgn}(\alpha) \int_0^\infty dE A^{\beta\beta}_{s's'}(s,\alpha;\varepsilon) f_\beta(\varepsilon), \\
P_{ss'} &= \frac{e^2}{h} \sum_{\substack{\sigma,\sigma'\in\uparrow,\downarrow \\ \alpha,\beta,\gamma,\delta\in e,h}} {\rm sgn}(\alpha){\rm sgn}(\beta) \int_0^\infty dE A^{\gamma\delta}_{\sigma\sigma'}(s,\alpha;\varepsilon) A^{\delta\gamma}_{\sigma'\sigma}(s',\beta;\varepsilon) f_\gamma(\varepsilon)[1 - f_\delta(\varepsilon)], \\
A^{\gamma\delta}_{\sigma\sigma'}(s,\alpha;\varepsilon) &= \delta_{s\sigma}\delta_{s\sigma'}\delta_{\alpha\gamma}\delta_{\alpha\delta} - [r^{\alpha\gamma}_{s\sigma}]^* r^{\alpha\delta}_{s\sigma'},
\end{aligned} \tag{3.5}$$

with $f_{\rm e}(\varepsilon) = 1 - f_{\rm h}(-\varepsilon) = 1/\{1 + \exp[(\varepsilon - eV)/k_B T]\}$ being the distribution of incoming electrons in the lead. Here ${\rm sgn}(\alpha) = +1$ for $\alpha = e$ and ${\rm sgn}(\alpha) = -1$ for $\alpha = h$. Inserting the reflection matrices of Eq. (3.4), one obtains at zero temperature

$$P_{\uparrow\downarrow} = -\frac{2e^2}{h}\Gamma_\uparrow\Gamma_\downarrow \frac{eV}{(eV)^2 + \Gamma^2}, \tag{3.6}$$

where $\Gamma_s = 2\pi\nu_0|t_s|^2$. As anticipated, $P_{\uparrow\downarrow}$ is negative and goes to zero at high voltages as $-1/V$ (assuming eV remains smaller than the superconducting gap).

The result of Eq. (3.6) does not depend on details such as the particular system hosting the MBS, the nature of the coupling to the lead, or the particular spin polarization axis. One can change the spin axis by transforming the coupling constants according to

$$\left(t'_\uparrow,\ \ t'_\downarrow\right) = \left(t_\uparrow,\ \ t_\downarrow\right) \cdot \exp(-i\theta\hat{\mathbf{n}}\cdot\boldsymbol{\sigma}/2), \tag{3.7}$$

where $\boldsymbol{\sigma}$ is a vector of Pauli matrices, $\hat{\mathbf{n}}$ is a unit vector and θ is a rotation angle. We note in passing that by varying both $\hat{\mathbf{n}}$ and θ one can always find a spin axis such that $t'_\downarrow = 0$ [102], resulting in a spin-polarized current [21].

Next, we consider an accidental low-energy ABS. For simplicity we shall temporarily assume that spin in the z direction is conserved*. Under these assumptions the most general tunneling Hamiltonian is given by†

$$\tilde{H}_T = a^\dagger \sum_k \left(\tilde{t}_\uparrow \psi_{k\uparrow} + \tilde{t}_\downarrow \psi^\dagger_{k\downarrow} \right) + \text{h.c.}, \tag{3.8}$$

where a is the annihilation operator for the ABS. (Notice that if one writes a in terms of two Majorana operators, then both of them are coupled to the lead with equal strength.) One can now use Eq. (3.3) with

$$W = \sqrt{\nu_0} \begin{pmatrix} \tilde{t}_\uparrow & 0 & 0 & \tilde{t}^*_\downarrow \\ 0 & \tilde{t}_\downarrow & \tilde{t}^*_\uparrow & 0 \end{pmatrix}, \tag{3.9}$$

to obtain the reflection matrices

$$r^{\text{ee}} = \frac{iE}{iE - \tilde{\Gamma}/2} + \frac{(\tilde{\Gamma}_\uparrow - \tilde{\Gamma}_\downarrow)/2}{iE - \tilde{\Gamma}/2}\sigma^z \quad ; \quad r^{\text{he}} = \frac{2\pi\nu_0 \tilde{t}_\uparrow \tilde{t}_\downarrow}{iE - \tilde{\Gamma}/2}\sigma^x \tag{3.10}$$

These reflection matrices are written in the basis of the spin in the z direction. To obtain them for a general spin direction, we perform a transformation on r^{ee}, r^{he} which rotates the spin axis by an angle θ away from the z axis. Upon doing so, and then using Eq. (3.5) one has

$$\begin{aligned} P_{\uparrow\downarrow} = \frac{2e^2}{h} \frac{\tilde{\Gamma}_\uparrow \tilde{\Gamma}_\downarrow}{\tilde{\Gamma}} \Bigg\{ & \left[\frac{(\tilde{\Gamma}_\uparrow - \tilde{\Gamma}_\downarrow)^2}{\tilde{\Gamma}^2} + \cos^2\theta \right] \cdot \arctan \frac{2eV}{\tilde{\Gamma}} \\ & + \left[\frac{(\tilde{\Gamma}_\uparrow - \tilde{\Gamma}_\downarrow)^2}{\tilde{\Gamma}^2} - \cos^2\theta \right] \cdot \frac{2eV/\tilde{\Gamma}}{1 + (2eV/\tilde{\Gamma})^2} \Bigg\}. \end{aligned} \tag{3.11}$$

This should be compared to Eq. (3.6). Unlike the MBS scenario, $P_{\uparrow\downarrow}$ is now positive for all V and monotonically approaches a finite value at $eV \gg \tilde{\Gamma}$.

*We shall demonstrate below, using numerical simulations of a system with spin-orbit coupling, that our conclusions apply also for an ABS with a non-well-defined spin.

†An example of a model for an ABS which yields Eq. (3.8) is presented in Appendix 3.B.

3.2.3 Microscopic model

Next we verify our conclusions using a numerical simulation of an experimentally realizable microscopic model [25–28]. We consider a nanowire having Rashba spin-orbit coupling, proximity coupled to an s-wave superconductor, with an applied Zeeman field. The wire is tunnel coupled to a normal lead from the left, as depicted in Fig. 3.1. The BdG Hamiltonian describing the proximitized nanowire (not including the lead and the spin filters) is given, in the basis $\Psi(x) = [\psi_\uparrow^\dagger(x), \psi_\downarrow^\dagger(x), \psi_\downarrow(x), -\psi_\uparrow(x)]$, by

$$\mathcal{H}_{\rm nw} = \left[\frac{-\nabla^2}{2m_{\rm e}} + V(x,y)\right]\tau^z + i\lambda_{\rm R}(\sigma^y\partial_x - \sigma^x\partial_y)\tau^z - \frac{\mu_{\rm B}g}{2}\mathbf{B}\cdot\boldsymbol{\sigma} + \Delta_{\rm ind}(x)\tau^x, \quad (3.12)$$

where $m_{\rm e}$ is the effective mass of the electron, $V(x,y)$ includes both the chemical potential and a disordered potential, $\lambda_{\rm R}$ is the Rashba spin-orbit coupling strength, $\mathbf{B}$ is the magnetic field, $\mu_{\rm B}$ is the Bohr magneton, g is the Landé g-factor, $\Delta_{\rm ind}(x) = \Delta_0\theta(L_{\rm s}/2 - |x|)$ is the proximity-induced pair potential, and $\boldsymbol{\sigma}$ and $\boldsymbol{\tau}$ are vectors of Pauli matrices in spin and particle-hole space, respectively*.

We approximate the continuum model of Eq. (3.12) by a tight-binding Hamiltonian

$$\begin{aligned} H = &\sum_{\mathbf{r}}\sum_{s,s'}\Bigg\{\left[V_{\mathbf{r}}\delta_{ss'} - \frac{\mu_{\rm B}g}{2}\mathbf{B}\cdot\boldsymbol{\sigma}_{ss'}\right]c^\dagger_{\mathbf{r},s}c_{\mathbf{r},s'} \\ &\qquad - \sum_{\mathbf{d}=\hat{x},\hat{y}}\left[(t_{\rm tb}\delta_{ss'} + iu(\boldsymbol{\sigma}_{ss'}\times\mathbf{d})\cdot\hat{z})c^\dagger_{\mathbf{r},s}c_{\mathbf{r}+a_0\mathbf{d},s'} + \text{h.c.}\right]\Bigg\} \\ &+ \sum_{|\mathbf{r}\cdot\hat{x}|<L_{\rm s}/2}\left[\Delta_0 c^\dagger_{\mathbf{r},\uparrow}c^\dagger_{\mathbf{r},\downarrow} + \text{h.c.}\right], \end{aligned} \quad (3.13)$$

where $\mathbf{r}$ runs over the sites of an N_x by N_y square lattice with spacing a_0. Here $t_{\rm tb} = 1/2m_{\rm e}a_0^2$, $u = \lambda_{\rm R}/2a_0$, $V_{\mathbf{r}} = -\mu + 4t_{\rm tb} + V^{\rm dis}_{\mathbf{r}}$, μ is the chemical potential, and $V^{\rm dis}_{\mathbf{r}}$ is a Gaussian-distributed disorder potential with zero average and correlations $\overline{V^{\rm dis}_{\mathbf{r}}V^{\rm dis}_{\mathbf{r}'}} = v^2_{\rm dis}\delta_{\mathbf{r}\mathbf{r}'}$†. As we now show, this system can exhibit either a zero-energy ABS or a zero-energy MBS at the end of the wire, depending on the value of $\mathbf{B}$. The differential conductance spectra in the two cases are similar. The spin-resolved current correlations, however, are qualitatively different.

*We assume the transverse dimensions of the wire are small enough, such that we can ignore the orbital effect of the magnetic field.

†In this section we concentrate on the strictly one-dimensional case, and on zero disorder. The effects of multiple transverse channels and of having nonzero disorder potential will be examined below, in Sec. 3.3.2.

We express H in a first quantized form as a $4N_xN_y \times 4N_xN_y$ matrix $\mathcal{H}_{\rm TB}$, from which one extracts the retarded Green function

$$G^R(\varepsilon) = \left(\varepsilon - \mathcal{H}_{\rm TB} + i\pi W_{\rm TB} W_{\rm TB}^\dagger\right)^{-1}, \tag{3.14}$$

and subsequently the reflection matrix [100, 101]

$$r_{\rm tot}(\varepsilon) = 1 - 2\pi i W_{\rm TB}^\dagger G^R(\varepsilon) W_{\rm TB}. \tag{3.15}$$

Here, $W_{\rm TB}$ is a matrix describing the coupling of the eigenmodes in the leads to the end of the nanowire, and it contains the information regarding the spin filtering. The construction of $W_{\rm TB}$ and $\mathcal{H}_{\rm TB}$, along with further details of the tight-binding simulation are presented in Appendix 3.A. The metallic leads are described in the wide band limit by an energy independent $W_{\rm TB}$. With the help of Eqs. (3.15) and (3.5) we then obtain the currents through the leads and their cross correlation.

In Fig. 3.2(a) the differential conductance $d\langle\hat{I}\rangle/dV$ is presented as a function of bias voltage V and Zeeman energy $E_{\rm Z} = \mu_{\rm B} g|\mathbf{B}|/2$, for a value of $\mu = 125\mu eV$ and at a temperature of $T = 30mK$. The magnetic field $\mathbf{B}$ is applied at an angle of 60° from the y axis in the xy plane. The dashed white line signifies the critical Zeeman energy $E_{\rm Z}^{\rm c} = \sqrt{\mu^2 + \Delta_0^2}$ above which the system is in the topological phase in the thermodynamic limit [15, 16]. Beyond this a zero-energy MBS appears, and one observes a ZBCP. At even higher magnetic fields the conductance begins to oscillate due to the overlap between the MBSs at the two ends of the wire [27, 103–105].

Importantly, a ZBCP is also present at a magnetic field which is *below* the critical line, at about $E_{\rm Z} \sim 0.1meV$, even though the system is in the topologically trivial phase. This ZBCP is due to a trivial ABS which is localized at the left end of the wire*. In Fig. 3.2(b) the local density of states (LDOS) at zero energy $\mathcal{N}(x, 0)$ is presented for two different Zeeman energies $E_{\rm Z} = 350\mu eV$ and $E_{\rm Z} = 90\mu eV$, corresponding to the MBS and ABS, respectively. We note that in both cases the LDOS is peaked at the two ends of the wire, making it difficult to distinguish between the ABS and the MBS via a scanning tunneling microscopy measurement.

The spin-resolved current correlation $P_{\uparrow\downarrow}$, on the other hand, is qualitatively different for the two cases. Figure 3.2(c) and Fig. 3.2(d) show $P_{\uparrow\downarrow}$ as a function of bias for the MBS ($E_{\rm Z} = 350\mu eV$) and for the ABS ($E_{\rm Z} = 90\mu eV$), respectively. As anticipated, in the case of a MBS the correlations are negative and approach zero at high voltages. In the case of an ABS, the correlations are positive and approach a finite value at large V. This is in agreement with the analytical low-energy treatment which resulted in Eq. (3.6) and Eq. (3.11).

*An additional ABS is formed at the right end the wire in the normal region (see Fig. 3.1).

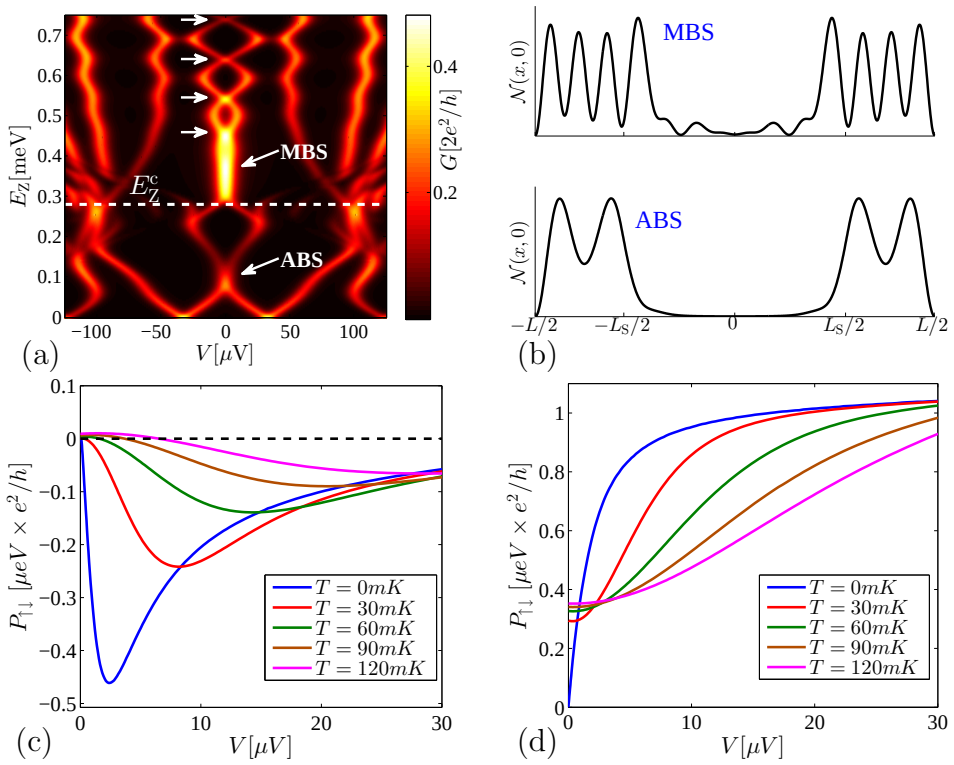

Figure 3.2: Numerical simulation of the system depicted in Fig. 3.1. The parameters of the system are taken to be in accordance with a recent experiment [25], namely $E_{\rm so} = m_{\rm e}\lambda_{\rm R}^2/2 = 50\mu eV$, $\Delta_0 = 250\mu eV$, and $l_{\rm so} = 1/(m_{\rm e}\lambda_{\rm R}) = 200nm$. We take the length of the wire to be $L = 2.5\mu m$ with $L_{\rm S} = 1.4\mu m$. Similar results are obtained for parameters taken from a different experiment [27] (see also Appendix 3.C). The magnetic field $\mathbf{B}$ is applied at an angle of 60° from the y axis in the xy plane. (a) Differential conductance as a function of bias V and Zeeman energy $E_{\rm Z} = \mu_{\rm B} g|\mathbf{B}|/2$ for $\mu = 125\mu eV$ and at $T = 30mK$, in units of $G_0 = e^2/h$. A zero-bias conductance peak appears both as a result of a Majorana bound state (MBS) at $B > B_c$, and as a result of a trivial Andreev bound state (ABS) at $E_{\rm Z} < E_{\rm Z}^{\rm c}$. (b) Local density of state at zero energy for $E_{\rm Z} = 350\mu eV$ and for $E_{\rm Z} = 90\mu eV$, where the system hosts a localized MBS and an ABS, respectively. In both cases the density of states is significant only near the ends of the wire. (c),(d) Spin-resolved currents correlation $P_{\uparrow\downarrow}$ vs V at different temperatures for (c) the MBS and (d) the ABS. For the Majorana case, $P_{\uparrow\downarrow}$ is negative and goes to zero at large V. This is in striking contrast to the case of an ABS, where $P_{\uparrow\downarrow}$ is positive and approaches a finite constant value at large V. Here, the spin polarization axis is in the y direction (the direction of spin-orbit coupling). The effect of choosing a different polarization axis is shown in Fig. 3.3(a).

Interestingly, the main features distinguishing a MBS from an ABS survive even at finite temperatures, as apparent in Figs. 3.2(c,d). At a finite temperature, $P_{\uparrow\downarrow} \neq 0$ at zero voltage. $P_{\uparrow\downarrow}$ recovers its low-T behavior at voltage $eV \gtrsim T$. In particular, one can witness these distinctive features even for $T > \Gamma$. We note that Figs. 3.2(c), 3.2(d) present results for voltages that are smaller than the excitation gap in the system (roughly $50\mu eV$). At higher voltages the features of $P_{\uparrow\downarrow}$ are no longer universal as $P_{\uparrow\downarrow}$ picks up contributions from higher-energy resonances.

The spin-resolved currents whose correlation is presented in Figs. 3.2(c,d) are all defined with respect to the y spin axis (the direction of the spin-orbit coupling). In Fig. 3.3(a) we present $P_{\uparrow\downarrow}$ for spin-resolved currents defined with a spin axis rotated by an angle θ from the y axis in the xy plane. The results for the MBS (solid lines) and for the ABS (dashed lines) are obtained at zero temperature and for the same parameters as those of Fig. 3.2(c) and Fig. 3.2(d), respectively. It is apparent that the same distinctive features persist upon rotating the spin axis. We point out the suppression of $P_{\uparrow\downarrow}$ in the MBS case for $\theta = 60^\circ$, which is the direction of $\mathbf{B}$. This is caused due to polarization of the Majorana wave function [106, 107] in the $\mathbf{B}$ direction, giving rise to a nearly perfect polarization of the spin-resolved current through the MBS.

It is interesting to examine the crossover between the MBS case and the ABS case. This can be done by increasing E_{Z} to the point where there is a large overlap between the MBSs at the two ends of the wire. At this point, the two Majorana states are equivalent to a single ordinary ABS. In particular, they are both coupled to the lead with comparable strengths. In Fig. 3.3(b) we present $P_{\uparrow\downarrow}$ vs V for various Zeeman energies E_{Z}, corresponding to two MBSs with increasing spatial overlap. As the overlap increases, $P_{\uparrow\downarrow}$ turns from being negative to being positive for all V. We note that for all these values of E_{Z} a ZBCP is present in the differential conductance spectra [cf. Fig. 3.2(a)].

3.3 Cross Correlations in a General Majorana Beam Splitter

In Sec. 3.2 we have examined the cross correlation between currents of opposite spin emitted from an MBS, showing that it is negative in sign and approaches zero at high bias voltage. In the present section we show that this result holds much more generally: The cross correlation of *any* two channels in the beam splitter has the same universal characteristics, i.e., it is negative and approaches zero at voltages larger than the width of the Majorana resonance, independently of whether the different channels are spin resolved or not. An immediate experimental consequence

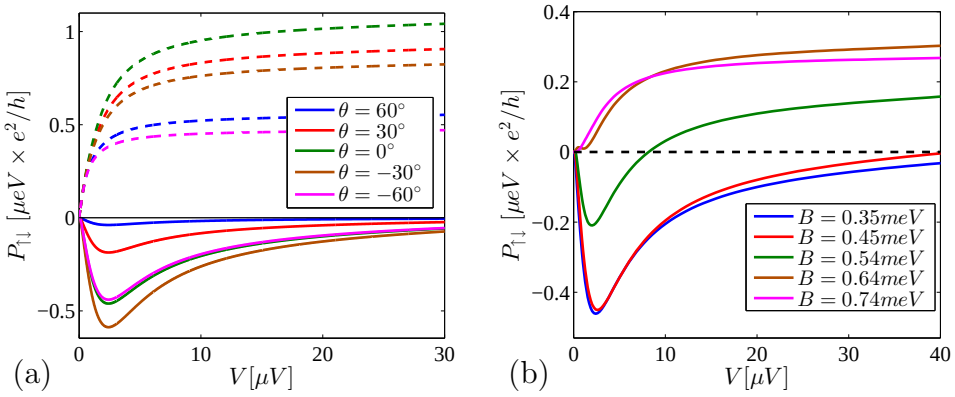

Figure 3.3: Spin-resolved current correlations $P_{\uparrow\downarrow}$ as a function of bias voltage V, at $T = 0$. (a) The spin-resolved currents are defined with respect to an axis which is rotated by an angle θ from the y axis in the xy plane. The direction of $\mathbf{B}$ remains fixed at an angle of 60° from the y axis. The characteristic features seem to be angle independent for both the Majorana bound state (MBS) $E_{\mathrm{Z}} = 350\mu eV$ (solid lines), and the trivial Andreev bound state (ABS), $E_{\mathrm{Z}} = 90\mu eV$ (dashed lines). (b) Crossover between a MBS and an ABS. As E_{Z} is increased the spatial overlap of the pair of Majorana end states increases until they are indistinguishable from an ordinary ABS [cf. marked points in Fig. 3.2(a)].

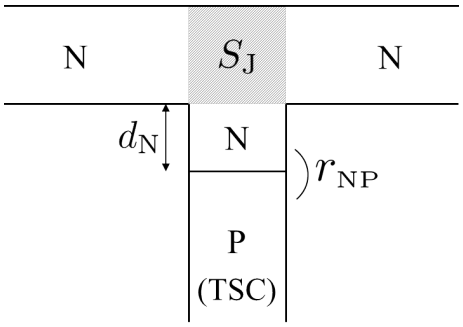

Figure 3.4: A schematic description of the experimental setup, a T-junction between a topological superconductor (TSC) and two metallic leads. We model the TSC by a spinless p-wave superconductor. It is coupled to the leads through a normal-metal section N, whose length $d_{\rm N}$ is taken to zero. Scattering at the NP interface is described by the reflection matrix $r_{\rm NP}$ [see Eq. (3.18)], while scattering at the T-junction is described by the matrix $S_{\rm J}$ [see Eq. (3.19)].

is that this effect can be observed in a much less challenging setup, which does not require spin filters to resolve the current into its spin components.

Let us consider again a T-junction between a topological superconductor (TSC) and two normal-metal leads as depicted in Fig. 3.1, but this time without the spin filters. We study the low-frequency cross correlation of the currents through the two arms of the junction, namely

$$P_{\rm RL} = \int_{-\infty}^{\infty} dt \langle \delta\hat{I}_{\rm R}(0)\delta\hat{I}_{\rm L}(t)\rangle, \tag{3.16}$$

where $\delta\hat{I}_\eta = \hat{I}_\eta - \langle\hat{I}_\eta\rangle$, and $\hat{I}_{\eta={\rm R,L}}$ are the current operators in the right and left arm of the junction respectively*. As before, we apply a voltage V between the two arms and the superconductor, and we denote by Γ and Δ the width of the Majorana resonance and the excitation gap†, respectively. Below we show that in the regime $eV \lesssim \Delta$, $P_{\rm RL}$ has a simple, universal behavior, given by Eq. (3.24). In particular, $P_{\rm RL}$ is negative and approaches zero when $eV \gg \Gamma$, like in the spin-resolved case. For $eV \gtrsim \Delta$ the behavior is nonuniversal.

*As in the spin-resolved case, the zero-frequency correlation matrix is symmetric, namely $P_{\rm LR} = P_{\rm RL}$. For a proof see Appendix B of Anantram *et al.* [97].

†The excitation gap Δ is either the superconducting gap, or the energy gap to the next subgap state (if such are present) above the Majorana zero-energy bound state.

Unlike studies which have focused on the cross correlation between currents through *two* MBSs at the two ends of a TSC [108–112], here the effect is due to a *single* MBS. In Ref. [108–112] it was crucial that the MBSs at the two ends of the TSC were coupled*. Here, on the other hand, the effect is most pronounced when the two MBSs are spatially separated such that only a single MBS is coupled to the leads.

3.3.1 Scattering-matrix approach

To calculate analytically P_{RL} we can use the low-energy Hamiltonian approach used in Sec. 3.2.2 for the spin-resolved case. Instead, let us use a scattering matrix approach; this allows one to include more easily direct scattering between the arms of the T junction. In this approach, the system is described by a combination of two scattering matrices, one for the T junction, and one for the interface between the TSC and the normal metal region of the middle leg (see Fig. 3.4). We are interested in bias voltages smaller than the gap of the TSC, Δ. An electron incident from one of the normal leads is therefore necessarily reflected from the middle (superconducting) leg. It can be reflected to the right or the left lead, either as an electron or as a hole. Since there is no transmission into the superconductor, scattering is described solely by a reflection matrix.

Each normal lead contains $2M$ transverse channels, including both spin species. The overall reflection matrix which we wish to obtain reads

$$r_{\mathrm{tot}} = \begin{pmatrix} r^{\mathrm{ee}} & r^{\mathrm{eh}} \\ r^{\mathrm{he}} & r^{\mathrm{hh}} \end{pmatrix}, \tag{3.17}$$

where each block is a $4M \times 4M$ matrix. The matrix element $r_{ij}^{\alpha\beta}$, where $\alpha, \beta = \{e, h\}$, is the amplitude for a particle of type β coming from the channel j to be reflected into the channel i as a particle of type α. Here, $i = 1, \ldots, 2M$ enumerates the channels in the right lead while $i = 2M+1, \ldots, 4M$ enumerates the channels in the left lead.

We model the TSC as a spinless p-wave superconductor which is a valid description close to the Fermi energy [113, 114]. It is convenient to insert a (spinless) normal-metal section between the TSC and the junction. In this way, we separate the scattering in the T-junction itself from the scattering at the normal–p-wave interface (cf. Fig. 3.4). The length of the normal-metal section d_{N} is then taken to zero.

*The coupling between the Majorana bound states is established either through a tunneling term, or through a nonlocal charging-energy term.

Andreev reflection at the normal–p-wave superconductor interface is described by

$$r_{\mathrm{NP}}(\varepsilon) = \begin{pmatrix} 0 & -a(\varepsilon) \\ a(\varepsilon) & 0 \end{pmatrix}, \tag{3.18}$$

where $a(\varepsilon) = \exp\left[-i \arccos(\varepsilon/\Delta)\right]$ is the Andreev reflection amplitude for $|\varepsilon| \leq \Delta$ [17, 86], with ε being the energy as measured from the Fermi level. The information about the topological nature of the system is encoded in $r_{\mathrm{NP}}(\varepsilon)$. The relative minus sign between the off-diagonal elements of $r_{\mathrm{NP}}(\varepsilon)$ signals that the pairing potential of the superconductor has a p-wave symmetry. Moreover, the nontrivial topological invariant [76, 115] $\nu = \det[r_{\mathrm{NP}}(0)] = -1$ dictates the existence of an MBS at each end of the superconductor.

Scattering at the T-junction (which connects the added normal section to the two leads) is described by

$$S_{\mathrm{J}} = \begin{pmatrix} S_{\mathrm{e}} & 0 \\ 0 & S_{\mathrm{e}}^{*} \end{pmatrix} \quad ; \quad S_{\mathrm{e}} = \begin{pmatrix} r & t' \\ t & r' \end{pmatrix}, \tag{3.19}$$

where S_{e} describes scattering of electrons and S_{e}^{*} describes scattering of holes. Here, r is a $4M \times 4M$ matrix describing the reflection of electrons coming from the left and right leads (each having $2M$ transverse channels), r' is a reflection amplitude for electrons coming from the middle leg (having a single channel), t is a $1 \times 4M$ transmission matrix of electrons from the right and left leads into the middle leg, and t' is a $4M \times 1$ transmission matrix of electrons from the middle leg into the right and left leads. The matrix S_{e} is assumed to be energy-independent in the relevant energy range, but is otherwise a completely general unitary matrix.

We can now concatenate S_{J} with r_{NP} to obtain the overall reflection matrix r_{tot} of Eq. (3.17). The block r^{ee} is obtained by summing the contributions from all the various trajectories in which an electron is reflected back as an electron, while the block r^{he} is obtained by summing those trajectories in which an electron is reflected as a hole. This yields

$$r^{\mathrm{ee}} = r + t'(-a)r'^{*}at + t'(-a)r'^{*}ar'(-a)r'^{*}at + \cdots = r - \frac{a(\varepsilon)^2 t' r'^{*} t}{1 + |r'|^2 a(\varepsilon)^2}, \tag{3.20a}$$

$$r^{\mathrm{he}} = t'^{*}at + t'^{*}ar'(-a)r'^{*}at + \cdots = \frac{a(\varepsilon)t'^{*}t}{1 + |r'|^2 a(\varepsilon)^2}, \tag{3.20b}$$

The two other blocks are given by $r^{\mathrm{eh}}(\varepsilon) = [r^{\mathrm{he}}(-\varepsilon)]^{*}$ and $r^{\mathrm{hh}}(\varepsilon) = [r^{\mathrm{ee}}(-\varepsilon)]^{*}$ in compliance with particle-hole symmetry [116].

Given the blocks of the reflection matrix, the sum of currents in the leads and their cross correlation are obtained by [97]

$$
\begin{aligned}
I &= \frac{e}{h} \sum_{\substack{k,l=1,\ldots,4M \\ \alpha,\beta\in\{e,h\}}} \mathrm{sgn}(\alpha) \int_0^\infty d\varepsilon A^{\beta\beta}_{kk}(l,\alpha;\varepsilon) f_\beta(\varepsilon), \\
P_{\mathrm{RL}} &= \frac{e^2}{h} \sum_{i\in\mathrm{R},j\in\mathrm{L}} \sum_{\substack{k,l=1,\ldots,4M \\ \alpha,\beta,\gamma,\delta\in\{e,h\}}} \mathrm{sgn}(\alpha)\mathrm{sgn}(\beta) \int_0^\infty d\varepsilon A^{\gamma\delta}_{kl}(i,\alpha;\varepsilon) A^{\delta\gamma}_{lk}(j,\beta;\varepsilon) f_\gamma(\varepsilon)[1-f_\delta(\varepsilon)], \\
A^{\gamma\delta}_{kl}(i,\alpha;\varepsilon) &= \delta_{ik}\delta_{il}\delta_{\alpha\gamma}\delta_{\alpha\delta} - (r^{\alpha\gamma}_{ik})^* r^{\alpha\delta}_{il},
\end{aligned}
\tag{3.21}
$$

where $I = \langle \hat{I}_{\mathrm{R}} \rangle + \langle \hat{I}_{\mathrm{L}} \rangle$ is the total current in the leads. Equation (3.21) is similar to Eq. 3.5, only now each arm includes a general number of channels, labeled by the indices i, j, k, and l (which include also spin channels). The index $i = 1, \ldots, 2M$ runs only over the channels of the right lead, while the index $j = 2M+1, \ldots, 4M$ runs only over those of the left lead. At zero temperature Eq. (3.21) reduces to [108]

$$
\begin{aligned}
I &= \frac{2e}{h} \int_0^{eV} d\varepsilon \mathrm{Tr}(r^{\mathrm{he}} r^{\mathrm{he}\dagger}), \\
P_{\mathrm{RL}} &= \frac{e^2}{h} \sum_{i\in\mathrm{R},j\in\mathrm{L}} \int_0^{eV} d\varepsilon \mathcal{P}_{ij}(\varepsilon)\,, \\
\mathcal{P}_{ij} &= |\mathcal{R}^{\mathrm{he}}_{ij}|^2 + |\mathcal{R}^{\mathrm{eh}}_{ij}|^2 - |\mathcal{R}^{\mathrm{ee}}_{ij}|^2 - |\mathcal{R}^{\mathrm{hh}}_{ij}|^2\,,
\end{aligned}
\tag{3.22}
$$

where $\mathcal{R}^{\alpha\beta} = r^{\alpha\mathrm{e}} r^{\beta\mathrm{e}\dagger}$.

Let us introduce the parameter $D = \sum_{i=1}^{4M} |t_i|^2$ representing total normal transmission from the two leads into the middle leg of the T-junction. Inserting Eq. (3.20) into Eq. (3.22) and using the unitarity of S_{e}, we first obtain the differential conductance

$$
\frac{dI}{dV} = \frac{2e^2}{h} \frac{\Gamma^2}{(eV)^2 + \Gamma^2},
\tag{3.23}
$$

where $\Gamma = \Delta D/2\sqrt{1-D}$. As expected dI/dV has a peak at $V = 0$ which is quantized to $2e^2/h$. Similarly, we obtain for the cross correlation

$$
P_{\mathrm{RL}}(V) = -\frac{2e^2}{h} \Gamma_{\mathrm{R}} \Gamma_{\mathrm{L}} \frac{eV}{(eV)^2 + \Gamma^2},
\tag{3.24}
$$

where $\Gamma_\eta = \Delta \sum_{i\in\eta} |t_i'|^2/2\sqrt{1-D}$ (note that $\Gamma = \Gamma_R + \Gamma_L$). The cross correlation $P_{\rm RL}$ is negative for all V and approaches zero as $-1/V$ for $eV \gg \Gamma$. This result is valid for $eV \leq \Delta$. It is valid even in the presence of strong disorder in the junction region, as we did not assume a particular form of $S_{\rm e}$. Moreover, it does not depend on a specific realization of the TSC hosting the MBS.

The high-voltage limit of Eq. (3.24) can be derived in a semiclassical picture of transport in a way which generalizes the intuitive analysis of Sec. 3.2.1. In particular, it shows that the high-voltage behavior stems from the fact that no local probe can determine the occupation of the MBS. This is explained in details in Sec. 3.3.3 below. The-low voltage limit can be understood from the perfect transmission of the MBS at zero energy, in exactly the same way as in the spin-resolved case. Namely, at zero voltage the total current noise, $P = P_{\rm R} + P_{\rm L} + 2P_{\rm RL}$, goes to zero, where $P_{\rm R}$ ($P_{\rm L}$) is the noise in the right (left) lead. Since, by definition, $P_{\rm R}, P_{\rm L} \geq 0$, this means that $P_{\rm RL}$ must be negative at low voltage.

3.3.2 Numerical analysis

We now turn to illustrate the above results using numerical simulations. As in Sec. 3.3.2, we consider the system depicted in Fig. 3.1, a semiconductor nanowire proximity coupled to a conventional s-wave superconductor and placed in a magnetic field. We use the same model given in Eqs. (3.12) and (3.13). In the this section we use parameters consistent with an InAs nanowire, namely $E_{\rm so} = m_{\rm e}\lambda_{\rm R}^2/2 = 75\mu$eV, $l_{\rm so} = 1/(m_{\rm e}\lambda_{\rm R}) = 130$nm, and $g = 20$ [27]. The induced pair potential is taken to be $\Delta_0 = 150\mu$eV. The length of the wire is $L = 2\mu$m, with the section not covered by the superconductor being $x_0 = 200$nm in length (see inset in Fig. 3.5(a)], and the width of the wire is taken to be $W_y = 130$nm*.

In Fig. 3.5 we present the cross correlation $P_{\rm RL}(V)$ and the differential conductance dI/dV at various temperatures for $\mu = 0$ and $B = 520$mT. For these values of μ and B the system is in the topological phase [15, 16, 117]. $P_{\rm RL}$ is negative and approaches zero at high voltages, in agreement with the analytic expression of Eq. (3.24). Interestingly, this behavior persists even at nonzero temperatures. The main effect of temperature is to increase the voltage above which $P_{\rm RL}$ starts approaching zero. Since the gap in the system is about 100μeV, the effect can be seen even at the relatively high temperature of $T = 100$mK, a temperature for which the zero-bias conductance peak is much lower than $2e^2/h$†.

*One immaterial difference between the present simulation and the one of Sec. 3.2.3 is that the SC-covered region extends all the way in the direction opposite to the junction, unlike in the drawing of Fig. 3.1.

†Notice in Fig. 3.5(b) that at zero temperature and at zero bias voltage the differential con-

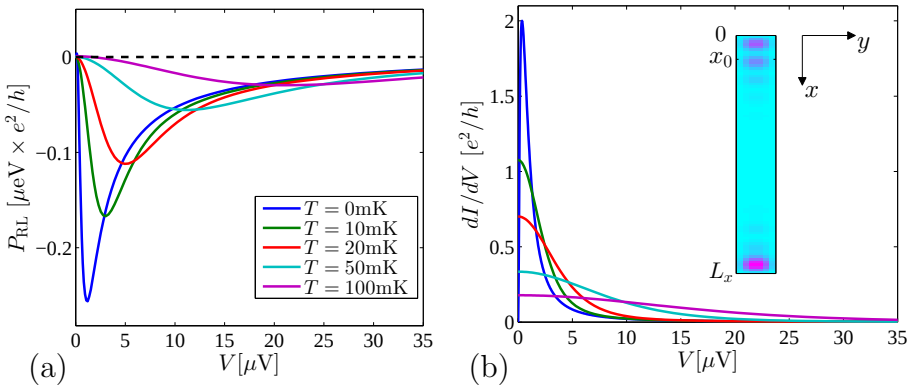

Figure 3.5: (a) Zero-frequency cross correlations $P_{\rm RL}$ [defined in Eq. (3.16)] of the currents through the left and right leads as a function of bias voltage V at various temperatures. $P_{\rm RL}$ is negative for all V and approaches zero at voltages which are larger than both the resonance width and the temperature. (b) Total differential conductance, dI/dV, where $I = I_{\rm R} + I_{\rm L}$. At zero temperature dI/dV exhibits a zero-bias conductance peak quantized to $2e^2/h$. A nonzero temperature widens the peak and reduces its height to a nonuniversal value. The inset shows the zero-temperature local density of states at zero energy in the wire in the absence of coupling to the leads in arbitrary units. The section of the wire not covered by the superconductor is $x \in [0, x_0]$.

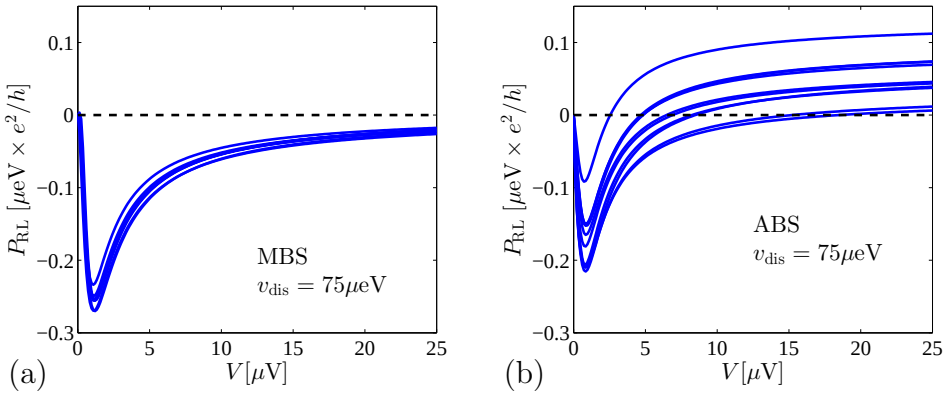

Figure 3.6: Current cross correlation $P_{\rm RL}$ vs. bias voltage V at $\mu = 0$ and $T = 0$ for different realization of short-range Gaussian disorder. (a) $B = 520mT > B_{\rm c}$, the system is in the topological phase with a zero-energy Majorana bound state (MBS) at each end of the wire. The universal behavior of $P_{\rm RL}(V)$, (being negative and approaching zero at high voltage) is not affected by the presence of disorder. (b) For each realization of disorder the magnetic field is tuned to have an Andreev bound state (ABS) with zero energy at the end of the wire, while keeping the system in the topologically trivial phase, $B = 170 - 200{\rm mT} < B_{\rm c}$ (see the text for more details). The behavior of $P_{\rm RL}(V)$ varies significantly for different realizations of disorder. In all cases $P_{\rm RL} > 0$ for large V in contrast to the topological case where it goes to zero.

Next, we study the effect of disorder on $P_{\rm RL}$. Figure 3.6(a) presents $P_{\rm RL}$ for 10 different realizations of random disorder with $v_{\rm dis} = 75\mu$eV. As expected, the behavior of $P_{\rm RL}$ does not change significantly. We can compare this to the case of an ordinary Andreev state which is tuned to zero energy. The end of the wire which is not covered by a superconductor ($x < x_0$ in Fig. 3.4) hosts Andreev bound states which are coupled to the leads. For each realization of disorder, we tune the magnetic field to bring one of them to zero energy, and calculate $P_{\rm RL}$. In all the realizations, the resulting tuned magnetic field was below the critical field $B_{\rm c} = 260mT$, i.e., the system is in the trivial phase. As shown in Fig. 3.6(b), the behavior of $P_{\rm RL}$ is nonuniversal and varies significantly from one realization of disorder to another. Importantly, in all cases $P_{\rm RL}$ is positive at large V.

In our simulations we have chosen the length of the wire $L_x = 2\mu$m to be suf-

ductance drops to zero. This is due to a finite-size effect, coming from the exponentially small energy splitting, E_M, between the two Majorana end states. For weak overlap of the Majoranas, the conductance approaches $2e^2/h$ at a voltage E_M/e.

ficiently bigger than the localization length of the Majorana wave function (which here is about $\xi \sim 300$nm), so that the leads are only coupled to a single MBS. If ξ becomes of the order of L_x, say by increasing the magnetic field B, then the leads become coupled also to the MBS at the other end of the wire. At this point it is as if the leads are coupled to a single ABS. Increasing the magnetic field therefore induces a *crossover* between the MBS case and the ABS case, in exactly the same way which was in Fig. 3.3(b).

It is interesting to examine the case when more than a single transverse channel is occupied in the wire. For weak pairing*, the system is in the topological phase whenever an odd number of channels is occupied. Figure 3.7 presents $P_{\rm RL}$ and dI/dV for various values of μ, each corresponding to a different odd number of occupied channels between 1 and 7. When more than a single channel is occupied we can have subgap Andreev bound states which coexist with the MBS. One such state can be seen in Fig. 3.7(b) as a peak at $V \simeq 80\mu$eV. It is only below this voltage that the behavior of $P_{\rm RL}(V)$ remains qualitatively the same as in the single channel case. In this respect, the existence of subgap states reduces the effective energy gap below which $P_{\rm RL}(V)$ exhibits its universal features. Another effect of introducing higher transverse channels is the stronger coupling of the middle leg of the T-junction to the two leads†.

3.3.3 Semiclassical picture

The behavior of the current cross-correlation, as given in Eq. (3.24), at high voltages can be derived based on simple semiclassical considerations. We reconsider the setup shown in Fig. 3.4, and examine the limit $eV \gg \Gamma$, where Γ is the width of the zero-energy resonance (which can be either an MBS or an ABS).

In this limit, the transport of current from the superconductor to the leads can be described in terms of a sequence of tunneling events. In each tunneling event, a Cooper pair in the superconductor dissociates; one electron is emitted into the right or left lead, and the other is absorbed into the zero mode localized at the edge of the superconductor. In the presence of such a zero mode, the many–body ground state of the superconductor is doubly degenerate. We denote the two ground states by $|0\rangle$ and $|1\rangle$, corresponding to an even and odd number of electrons in the superconducting wire, respectively. Each time an electron is emitted into the leads, the superconductor flips its state from $|0\rangle$ to $|1\rangle$ or vice versa.

*Weak pairing here means that the pairing potential Δ_0 is smaller than the Zeeman splitting and the energy spacing between transverse channels.

†This can be seen from the fact that the width of the zero-bias resonance in Fig. 3.7(b) becomes larger for higher numbers of transverse channels.

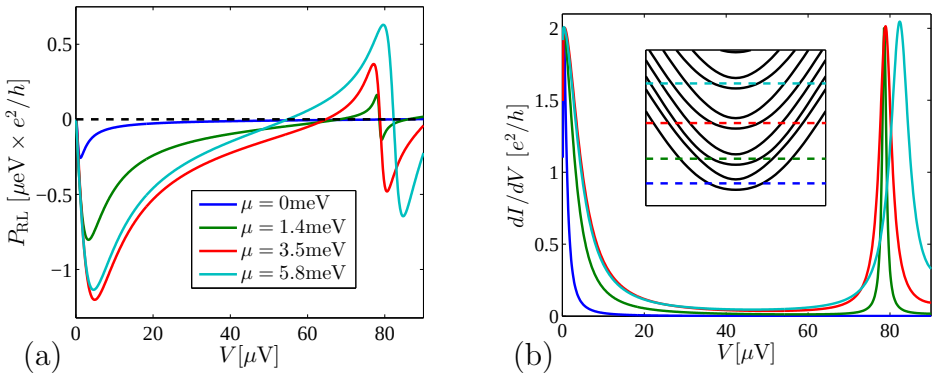

Figure 3.7: (a) Cross correlation and (b) differential conductance at various chemical potentials μ, corresponding to a different odd number of occupied transverse channels. The calculations are performed at $T = 0$, $v_{\rm dis} = 0$, and $B = 520$mT. The addition of occupied channels introduces extra subgap states which coexist with the Majorana bound state. These appears as peaks in the differential conductance spectra at finite V [see (b) at $V \simeq 80\mu$eV]. Above this voltage the behavior of $P_{\rm RL}$ is no longer universal.

Let us denote by $\Gamma^0_{\rm R}/h$ and $\Gamma^0_{\rm L}/h$ the probability per unit time to emit an electron into the right or left lead, respectively, given that the superconductor is in state $|0\rangle$. Similarly, $\Gamma^1_{\rm R,L}/h$ are the corresponding rates when the system is in the $|1\rangle$ state.

After a time τ, there are $N_{\rm R}$ and $N_{\rm L}$ electrons emitted to the right and left leads respectively. The average currents in the leads are given by

$$\langle I_R\rangle = \frac{e\langle N_{\rm R}\rangle}{\tau} \quad ; \quad \langle I_L\rangle = \frac{e\langle N_{\rm L}\rangle}{\tau}, \tag{3.25}$$

and the current cross correlation is given by

$$P_{\rm RL} = \lim_{\tau\to\infty}\frac{1}{\tau}\int_0^\tau dt_1\int_0^\tau dt_2\langle\delta I_{\rm R}(t_1)\delta I_{\rm L}(t_2)\rangle = \frac{e^2}{\tau}(\langle N_{\rm R}N_{\rm L}\rangle - \langle N_{\rm R}\rangle\langle N_{\rm L}\rangle). \tag{3.26}$$

In the case of a Majorana zero mode, all the local properties of the states $|0\rangle$ and $|1\rangle$ are identical. This is usually stated as the fact that one cannot make a local measurement which would reveal in which of the two ground states the system is in. In particular, this implies that $\Gamma^0_{\rm R} = \Gamma^1_{\rm R} \equiv \tilde{\Gamma}_{\rm R}$ and $\Gamma^0_{\rm L} = \Gamma^1_{\rm L} \equiv \tilde{\Gamma}_{\rm L}$. Let us divide the time τ into short time intervals $\Delta t \sim \frac{h}{eV}$; Δt is the minimal time between consecutive emission events (set by the minimal temporal width of an electron wave packet whose energy spread is $\sim eV$). At each time step Δt, either an electron is

emitted to the right lead, an electron is emitted to the left lead, or no electron is emitted at all. The transport process is thus described by a trinomial distribution. The probabilities of being emitted to the right and left lead are $p_R = \tilde{\Gamma}_R \Delta t/h$ and $p_L = \tilde{\Gamma}_L \Delta t/h$, respectively, and there are overall $N = \tau/\Delta t$ time steps. One thus obtains [118]

$$\begin{aligned} &\langle N_{\rm R}\rangle = N p_{\rm R} = \tilde{\Gamma}_{\rm R}\tau/h, \\ &\langle N_{\rm L}\rangle = N p_{\rm L} = \tilde{\Gamma}_{\rm L}\tau/h, \\ &\langle N_{\rm R}N_{\rm L}\rangle - \langle N_{\rm R}\rangle\langle N_{\rm L}\rangle = -N p_{\rm R} p_{\rm L} = -\frac{\tilde{\Gamma}_{\rm R}\tilde{\Gamma}_{\rm L}\tau\Delta t}{h^2}. \end{aligned} \tag{3.27}$$

Finally, inserting Eq. (3.27) into Eqs. (3.25) and (3.26) one has

$$\langle I_R\rangle = \frac{e}{h}\tilde{\Gamma}_{\rm R} \quad ; \quad \langle I_L\rangle = \frac{e}{h}\tilde{\Gamma}_{\rm L}, \tag{3.28}$$

and

$$P_{\rm RL} \sim -\frac{e}{h}\frac{\tilde{\Gamma}_{\rm R}\tilde{\Gamma}_{\rm L}}{V}. \tag{3.29}$$

$P_{\rm RL}$ is negative and approaches zero as $-1/V$. We have therefore reproduced the high-voltage limit of Eq. (3.24).

Unlike the case of an MBS, for an ABS the probabilities to emit an electron to the right or the left lead can depend on the state of the system, $|0\rangle$ or $|1\rangle$. To illustrate the effect this dependence has on the cross correlations, we consider the case

$$\Gamma^0_{\rm L} = 0 \quad ; \quad \Gamma^1_{\rm R} = 0 \tag{3.30}$$

where the electron can only go right if the system is in $|0\rangle$, and it can only go left if the system is in $|1\rangle$*. Because each time an electron is transmitted the state of the system changes (either from $|0\rangle$ to $|1\rangle$ or vice versa), it is clear that $N_{\rm R} = N_{\rm L} = N/2$. For simplicity we assume $\Gamma^0_{\rm R} = \Gamma^1_{\rm L} \equiv \tilde{\Gamma}$. In this case, the distribution for the total number of emitted electrons is binomial; in each time step we only ask whether an electron has been emitted to one of the leads or not. The probability for an electron to be emitted is $p = \tilde{\Gamma}\Delta t/h$. Remembering that half of the times the electron is emitted to the right and half of the times to the left, one obtains

$$\langle N_{\rm R}N_{\rm L}\rangle - \langle N_{\rm R}\rangle\langle N_{\rm L}\rangle = \frac{1}{4}Np(1-p) = \frac{\tau\tilde{\Gamma}}{4h}\left(1 - \frac{\tilde{\Gamma}\Delta t}{h}\right). \tag{3.31}$$

*This resembles the case studied in 3.2 of spin-resolved transport through an ABS in a system which conserves the z-component of the spin. There, the emitted electron can only have spin up (down) if the superconductor is in the state $|0\rangle$ ($|1\rangle$), respectively.

Inserting this into Eq. (3.26) one has

$$P_{\mathrm{RL}} = \frac{1}{4}\frac{e^2}{h}\tilde{\Gamma}\left(1 - C\frac{\tilde{\Gamma}}{eV}\right), \tag{3.32}$$

where C is a constant of order unity. P_{RL} is monotonically increasing, asymptotically approaching a positive constat. This is in agreement with Fig. 3.6(b) and with Fig. 3.2(d).

3.4 Detecting Coupled Majoranas by Charge Sensing

It Secs. 3.2 and 3.3 we witnessed the consequences of an isolated MBS being nonlocal in nature. The meaning of this nonlocality is that the two degenerate many-body states defined by the Majorana, $|\,0\,\rangle$ and $|\,1\,\rangle$, do not differ in any local observable*. This in particular means that the average charge density is the same in both states, namely $\langle 0|\hat{\rho}(x)|0\rangle = \langle 1|\hat{\rho}(x)|1\rangle$, where $\hat{\rho}(x)$ is the charge density operator. This situation changes when two MBSs have a spatial overlap, as is the case in a long but finite topological superconducting wire. In this case, the two states $|\,0\,\rangle$ and $|\,1\,\rangle$ will generally not be perfectly degenerate, but will be split by a small amount, which decreases exponentially as the wire becomes long [11]. Similarly, the charge density in the two states will differ by a small amount.

In this section we explore the signatures of topological superconductivity in finite systems, in the limit where the MBSs at the two ends have a finite spatial overlap [119]. The spatial overlap can be varied by varying parameters such as chemical potential and magnetic field, which causes the energy difference between the two nearly degenerate ground states to oscillate [103–105]. In thermal equilibrium, as the energy difference crosses zero the system switch between the odd and even many-body states†, causing the charge density to jump. Between these jumps, the average number of electrons will vary continuously with the system parameters.

We examine the spatial distribution of the jumps in charge density. We find that, although the Majorana wave functions (and hence the tunneling density of states) are peaked at the *ends* of the wire, the discontinuity in charge density arising from

*The two states, $|\,0\,\rangle$ and $|\,1\,\rangle$, differ only in their fermion number parity. This, however, is a nonlocal observable which can only be revealed in a global measurement.

†We note that although the system's Hamiltonian conserves fermion parity, the fermion parity can still change when a parameter is varied on laboratory time scales. This is due to the presence of a small number of thermally activated quasiparticles in the bulk superconductor.

the overlap of the Majoranas is *spread* along the wire. We suggest that these jumps in the charge can be measured, for example, using a single-electron transistor.

Whereas existing experimental signatures, such as the ZBCP, require direct contact to the wire for tunneling measurements, charge sensing avoids this issue and provides an orthogonal measurement to confirm recent experimental developments. Furthermore, by comparing density of states measurements, which is expected to exhibit Majorana features at the wire ends, with a uniformly-distributed charge measurements, one can rule out alternative explanations for the ZBCP, such as the Kondo effect [94].

We start by considering, as a toy model for a TSC, the spinless p-wave superconductor. In a finite system it is described by the BdG Hamiltonian

$$\begin{aligned} H_{\mathrm{p}} &= \int_0^L \mathrm{d}x \Psi^\dagger(x) \mathcal{H}_{\mathrm{p}}(x) \Psi(x) \quad ; \quad \Psi^\dagger(x) = [\psi^\dagger(x), \psi(x)] \\ \mathcal{H}_{\mathrm{p}}(x) &= \left(\frac{-\partial_x^2}{2m} - \mu \right) \tau^z - i\Delta' \partial_x \tau^y, \end{aligned} \tag{3.33}$$

where L is the length of the system, μ is the chemical potential, and Δ' is the amplitude of the p-wave pairing potential. Upon analyzing the jumps in charge density in the case of H_{p}, we would be able to relate the results to the case of a proximity-coupled semiconductor wire, as the two models are equivalent in certain limits.

Let the eigenfunctions of $\mathcal{H}_{\mathrm{p}}(x)$ be denoted by the vectors, $\phi_\nu(x) = [u_\nu(x), v_\nu(x)]^{\mathrm{T}}$, and their respective eigenenergies, ϵ_ν. The expectation value of the charge density is given by

$$\langle \rho(x) \rangle_T = \sum_\nu |u_\nu(x)|^2 f(\varepsilon_\nu) + |v_\nu(x)|^2 f(-\varepsilon_\nu), \tag{3.34}$$

where the sum is only over the positive energies, $\varepsilon_\nu > 0$, and $f(\varepsilon)$ is the Fermi-Dirac distribution. At zero temperature, the change in the average charge density due to the occupation of the ν^{th} state is*

$$\delta\rho_\nu(x) = |u_\nu(x)|^2 - |v_\nu(x)|^2. \tag{3.35}$$

When the system is in the topological regime, $\mu > 0$, the Hamiltonian has a pair of eigenstates, $\phi_0(x)$ and $\tau^x \phi_0^*(x)$, related by particle-hole symmetry, with energies

*Notice Eqs. (3.35) and (3.34) are general and are not specific to the case of a spinless p-wave superconductor.

$\pm\varepsilon_0$ which goes to zero in the limit $L \to \infty$. These eigenstates define a fermionic excitation

$$f^\dagger = \int \mathrm{d}x \Psi^\dagger(x) \cdot \phi_0(x) \quad ; \quad f = \int \mathrm{d}x \Psi^\dagger(x) \cdot [\tau^x \phi_0^*(x)] \,. \tag{3.36}$$

We can write f and $f^\dagger$ in terms of two Majorana operators*,

$$f = (\gamma_\mathrm{R} + i\gamma_\mathrm{L})/2 \quad ; \quad f^\dagger = (\gamma_\mathrm{R} - i\gamma_\mathrm{L})/2, \tag{3.37}$$

which results in

$$\gamma_\mathrm{R} = \int \mathrm{d}x \left[u_\mathrm{R}(x)\psi^\dagger(x) + u_\mathrm{R}^*(x)\psi(x)\right], \tag{3.38a}$$

$$\gamma_\mathrm{L} = \int \mathrm{d}x \left[u_\mathrm{L}(x)\psi^\dagger(x) + u_\mathrm{L}^*(x)\psi(x)\right], \tag{3.38b}$$

where $u_\mathrm{R} = u_0 + v_0^*$, and $u_\mathrm{L} = (u_0 - v_0^*)/i$. The functions u_R and u_L are localized at the two ends of the system. Without loss of generality we take u_R to be localized near the right end, and u_L near the left end. Using Eq. (3.35) for the Majorana case ($\nu = 0$), one has in terms of the Majorana wave functions, $u_\mathrm{R}(x)$ and $u_\mathrm{L}(x)$,

$$\delta\rho_0(x) = \mathrm{Im}\left[u_\mathrm{R}(x)u_\mathrm{L}^*(x)\right]. \tag{3.39}$$

Namely, the jump in charge density as the Majorana changes its occupation goes to zero in the limit $L \to \infty$, since in this case the overlap between u_R and u_L vanishes. This is a manifestation of the nonlocality of the Majorana bound state; a measurement of a local observable such as the charge density cannot reveal its occupation.

We are interested with the distribution of $\delta\rho_0(x)$ for a system with a long but finite length, L. The Majorana wave function can be approximated by

$$\begin{aligned} u_\mathrm{L}(x) &= \frac{2}{\sqrt{\xi}} e^{-x/\xi} \sin(k_\mathrm{F} x), \\ u_\mathrm{R}(x) &= \frac{2}{\sqrt{\xi}} e^{(x-L)/\xi} \sin[k_\mathrm{F}(x-L)], \end{aligned} \tag{3.40}$$

which is valid in the limit, $L \gg \xi \gg 1/k_\mathrm{F}$, with $k_\mathrm{F} = \sqrt{2m\mu}$ and $\xi = 1/m\Delta'$ being the Fermi momentum and the coherence length, respectively. Inserting this into Eq. (3.39), results in

$$\delta\rho_0(x) = \frac{4e^{-L/\xi}}{\xi} \sin(k_\mathrm{F} x) \sin[k_\mathrm{F}(x-L)]. \tag{3.41}$$

*The Majorana operators, γ_R and γ_L describe excitations of the H_p only in the case $\varepsilon_0 = 0$. This is because each of them is a superposition of two excitations with energies ε_0 and $-\varepsilon_0$.

Notice that while the wave function of each of the Majorana bound states is peaked near one of the ends of the wire, the charge density difference oscillates with a uniform amplitude along the wire. This effect can be measured using a scanning SET, or with multiple SETs at several positions along the wire. It can then serve as a signature of topological superconductivity. The total charge difference associated with the state is given by $\delta N_0 = \int \mathrm{d}x \delta\rho_0(x) \approx e^{-L/\xi} L/\xi$.

In Fig. 3.8 we present numerical tight-binding simulations of the system described in Eq. (3.12) in the strictly 1d case. Figure 3.8(a-b) show the ground-state fermion parity and the compressibility, respectively, as a function of chemical potential and magnetic field. Figure 3.8(c) shows the single-particle excitation spectrum as function of Zeeman field E_{Z}, for $\mu = 0$. The energy oscillations of the overlapping Majorana mode is emphasized in red. These oscillations are the source of the fermion parity switches and the compressibility peaks in Fig. 3.8(a-b). Finally, Fig. 3.8(d) presents the Majorana wave function (top panel) and the distribution of the charge density jumps (bottom panel).

3.5 Discussion

When current from a topological superconductor is split into two metallic leads, the current cross correlation, P_{RL}, exhibit a universal behavior as a function of bias voltage V. The cross correlation is negative for all V and approaches zero at high voltage as $-1/V$. This behavior is robust and does not rely on a specific realization of the topological superconductor hosting the Majorana, or on a specific form of coupling to the leads. It can be observed even in disordered multichannel systems at finite temperatures. For the effect to be observed the width of the Majorana resonance, Γ, has to be smaller than the energy of the first subgap state. Importantly, the temperature T does not have to be smaller than Γ.

These results for the current cross correlation have their roots in the defining properties of MBSs. The high-voltage behavior can be shown to stem from the nonlocal nature of MBS; the fact that the occupation of the Majorana mode cannot be revealed by any local probe. The low-voltage behavior stems from the fact that the MBS induces perfect Andreev reflection at zero bias.

It is interesting to compare the situation of a MBS with the case of an accidental low-energy Andreev bound state (ABS). When the normal-metal leads are coupled to an ABS, the cross correlation P_{RL} has a nonuniversal behavior. In particular, the observed behavior is sensitive to details of the system, such as the realization of disorder [see Fig. 3.6(b)]. The cross correlation can be either positive or negative at low voltage ($eV \leq \Gamma$). At high voltage it will generally approach a positive constant,

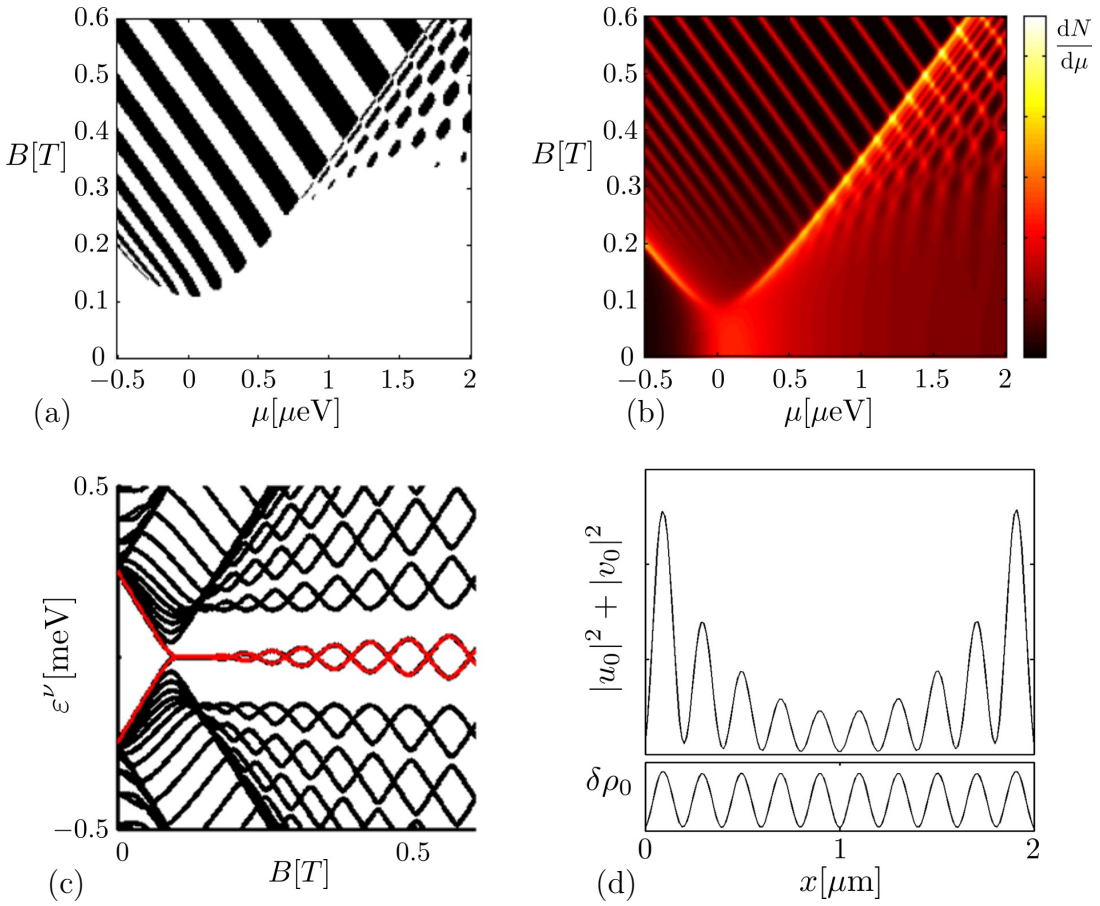

Figure 3.8: (a) Ground state Fermion parity of a finite wire as a function of chemical potential μ and magnetic field B for $\Delta_{\text{ind}} = 0.25meV$, $\lambda_{\text{R}} = 0.2eV\mathring{A}$, $g = 50$, $m^* = 0.013m_0$ and wire length $L = 2\mu m$. Once in the topological regime $E_{\text{Z}} > \sqrt{\mu^2 + \Delta_{\text{ind}}^2}$, one can observe switches of parity due to the oscillating splitting of the overlapping Majorana states. (b) The compressibility $\partial N/\partial\mu$, with N the total electron number, as a function of chemical potential and magnetic field. This quantity can in principle be measured using a single electron transistor (SET) placed in proximity to the wire. (c) Quasiparticle energy spectrum as function of Zeeman field E_{Z} with length $L = 2\mu m$, and for $\mu = 0$. Once in the topological regime, we see the mid-gap degenerate Majorana states, which then split and oscillate. (d) Top: Intensity of the wave function (a.u.) for a Majorana-pair state whose energy crosses zero at a degeneracy point in the spectrum ($B \sim 0.24T$). As expected, the wave function is concentrated at edges, and decays toward the centre. Bottom: The change in charge density (a.u.) when this state becomes occupied. The charge difference is spread along the wire length.

however, this constant can in principle be very small. Namely, there can be cases where the ABS will mask itself as an MBS in both differential conductance and current cross correlation. In fact, this is a generally true statement when discussing experimental signatures of MBSs versus ABSs. This is because a zero-energy ABS can always be resolved into two MBSs. If one then couples the experimental probe to only *one* of them, one is bounded to witness the behavior of a MBS. It should be noted, however, that this would generally require a lot of fine tuning. First, the ABS has to be tuned to zero energy which is not the generic case, and then the probe, which can have many degrees of freedom*, has to be decoupled from one of the MBSs composing the ABS.

By implementing oppositely-polarized spin filters on the two arms of the T junction, one can in principle measure the spin-resolved current cross correlation which was discussed in Sec. 3.2. This obviously involves an additional experimental challenge, however, it has the advantage of resulting in a sharper distinction between the MBS and the ABS. When probing the MBS, the result would be qualitatively the same as in the non spin-resolved case. The ABS, on the other hand, induces cross correlations which are much more universal in the spin-resolved case, compared with the general case. In the spin-resolved case, the cross correlation are positive and approach a constant at high voltages, $eV \gg \Gamma$, in sharp distinction to the MBS. This can be understood from the fact that the high-voltage spin-resolved correlation probes the spin density carried by the bound state. In the MBS it is necessarily zero, while in the ABS it is generally nonvanishing, especially as one uses magnetic filed to tune the ABS to zero energy. To summarize, this means that the spin-resolved cross correlation can serve as a more distinctive signature of MBSs.

While we have concentrated in this chapter on topological superconductors (TSCs) in class D, the results for the cross correlations holds also for TSCs in class DIII, namely for time-reversal invariant TSCs (or TRITOPS). In the TRITOPS phase there are *two* MBSs at each end of the system, as dictated by Kramers' theorem. This pair of MBSs, however, is different than a trivial ABS. To see that this Kramers' pair of MBSs should yield the same behavior in cross correlation as a single MBS, let us resolved each of the leads in the T junction to pairs of channels related by time-reversal symmetry†. We assume each such channel contains both a right-moving and a left-moving mode‡. We can then perform a unitary transformation on each

*In the case of current correlation measurements, for example, these would be the coupling constants of the channels in the leads to one of the MBSs, or the parameters in the scattering matrix of the T junction [see Fig. 3.4 and Eq. (3.19)]

†Notice such a pair of channels necessarily belong to the same lead.

‡This is the usual case in normal-metal leads. The exception is when using as leads an anomalous 1D system, such as an edge of a topological insulator [81].

such pair of channels such that each of them is coupled to a different MBS of the Kramers' pair. It is then clear that the overall cross correlation will be a sum of correlations from two independent setups of a T junction having a single MBS.

In Sec. 3.4 we have examine the case of a long but finite TSC where the two MBSs at each end of the system begin to overlap. Strictly speaking, the low-energy excitations of the system are not MBS anymore. In particular, local observables now have different expectation values in the filled and empty states of the fermionic resonance. Namely, the MBSs are loosing their nonlocal property as they become coupled. We have examine the consequences of this fact in the charge density. By varying parameters such as the chemical potential or magnetic filed, one can obtain a signature of the weakly-coupled MBSs by measuring the jumps in charge density (say by using a single-electron transistor), which occur as the energy splitting of the MBSs oscillates.

A similar effect should exists in other local observables, for example the spin density. Like the charge density, the expectation value of spin-density is generally different in the two many-body states, when the MBSs are coupled. This difference in spin is considerably smaller than the spin of a single electron, and therefore very difficult to detect using available experimental techniques. However, recent advances suggest that such measurements might not be so far off [120, 121]. With an extremely sensitive magnetometer, one can hope to measure the jumps in the magnetization of the system as a function of chemical potential and magnetic filed, as discussed for the case of charge.

Appendices for Chapter 3

3.A Details of Tight-Binding Simulation

To obtain the scattering matrix using Eqs. (3.13-3.15) we express the Hamiltonian H in first quantized form using a $4N_xN_y \times 4N_xN_y$ matrix, $\mathcal{H}_{\rm TB}$, defined by

$$H = \textstyle\sum_{mn} \Psi^\dagger_m \mathcal{H}_{\rm TB} \Psi_n \quad ; \quad \Psi^\dagger = (\Phi^\dagger, \Phi) \ , \tag{3.42}$$

where $\Phi^\dagger_{m=2N_y(n_x-1)+2(n_y-1)+s} = c^\dagger_{\mathbf{r}=(n_xa,n_ya),s}$ creates an electron with spin s on site (n_x, n_y) of an $N_x \times N_y$ square lattice. Here, $s = 1$ for spin $=\uparrow$ and $s = 2$ for spin $\downarrow$. In the simulations of Sec. 3.2 we used $N_x = 90$, $N_y = 1$, while in those of Sec. 3.3 we used $N_x = 90$, $N_y = 6$.

The matrix $W_{\rm TB}$ in Eq. (3.14) describes the coupling between the extended modes of the leads and the sites of the lattice. In each lead there are M spinful transverse channels. Including both leads, both spin species, and the particle-hole degree of freedom, $W_{\rm TB}$ is a $4N_xN_y \times 8M$ matrix of the following form

$$W_{\rm TB} = \begin{pmatrix} W_{\rm e} & \mathbf{0} \\ \mathbf{0} & -W^*_{\rm e} \end{pmatrix} \quad ; \quad W_{\rm e} = \begin{pmatrix} W_{\rm L} & W_{\rm R} \end{pmatrix} , \tag{3.43}$$

where $W_{\rm L}$ and $W_{\rm R}$ described the coupling to the left and right lead, respectively. As depicted in Fig. 3.9, each lead is coupled only to those lattice sites which are adjacent to it. Moreover, the coupling to each site is modulated according to the transverse profile of the particular channel. This is described by

$$\begin{aligned} W_{\rm L} &= W^0 \otimes \begin{pmatrix} 1 \\ 0 \\ \vdots \\ 0 \end{pmatrix}^{\begin{matrix} 1 \\ 2 \end{matrix}}_{N_y} \otimes S_{\rm L} \quad ; \quad W_{\rm R} = W^0 \otimes \begin{pmatrix} 0 \\ \vdots \\ 0 \\ 1 \end{pmatrix}^{\begin{matrix} 1 \\ N_y-1 \end{matrix}}_{N_y} \otimes S_{\rm R} \ , \\ W^0_{nm} &= \begin{cases} w_m \sin \frac{\pi nm}{M+1} & , \quad 1 \le n \le M \\ 0 & , \quad M < n \le N_x \end{cases} , \ m = 1, \ldots, M. \end{aligned} \tag{3.44}$$

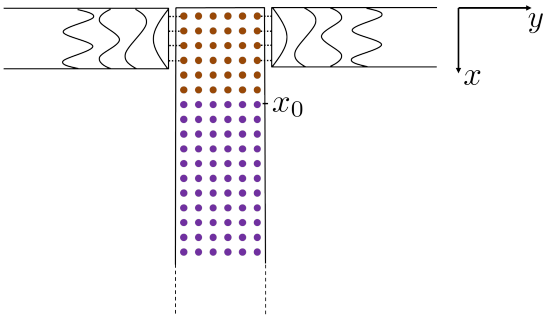

Figure 3.9: Illustration of the tight-binding model for the T junction studied in Secs. 3.2 and 3.3. Each lead is tunnel-coupled to the sites adjacent to it. The purple sites are ones in which there is a nonvanishing induced pair potential [cf. Eq. (3.13)]. The drawing demonstrates the case of Sec. 3.3 where the wire is modeled by $N_y = 6$ parallel chains, and each lead contains $M = 4$ spinful channels.

Here, $S_{\rm L}$ and $S_{\rm R}$ are 2×2 matrices describing the spin-dependent transmission of each of the two leads. In Sec. 3.2 which discusses spin-resolved correlations they are taken to be $S_{\rm R,L} = (\sigma^0 \pm \hat{\mathbf{n}} \cdot \boldsymbol{\sigma})/2$, where σ^0 is the 2×2 identity matrix and $\hat{\mathbf{n}}$ is the spin-polarization axis. In Sec. 3.3, on the other hand, we take $S_{\rm L} = S_{\rm R} = \sigma^0$. The parameters w_m describe the coupling of each transverse channel to the leads. In Sec. 3.2 we have simulated single-channel leads with $w_{m=1}^2 = 0.25\Delta_0$, while in Sec. 3.3 we have taken the leads to have four channels each, with $w_m^2 = 0.03\Delta_0, \forall m \in \{1, 2, 3, 4\}$. Given the coupling matrix, $W_{\rm TB}$, and the first-quantized Hamiltonian, $\mathcal{H}_{\rm TB}$, the reflection matrix is calculated using Eqs. (3.14) and (3.15).

3.B Model for an Andreev Bound State

In Eq. (3.8) we introduced a general form of a tunneling Hamiltonian describing a normal lead coupled to a zero-energy Andreev bound state under the assumption of conservation of the z component of the spin. For concreteness, we shall now derive this Hamiltonian starting from a model of a single-level quantum dot coupled to a superconductor and to a normal lead, in the presence of external magnetic field. The superconductor's degrees of freedom can be integrated out, resulting in an effective

low-energy Hamiltonian

$$
\begin{aligned}
H &= H_{\mathrm{L}} + H_{\mathrm{D}} + H_{\mathrm{T}}, \\
H_{\mathrm{L}} &= \sum_{ks} \epsilon_k \psi_{ks}^\dagger \psi_{ks}, \\
H_{\mathrm{D}} &= \sum_{ss'} (\epsilon_0 \delta_{ss'} - E_{\mathrm{Z}} \sigma^z_{ss'}) d_s^\dagger d_{s'} + (\bar{\Delta} d_\uparrow^\dagger d_\downarrow^\dagger + \mathrm{h.c.}), \\
H_{\mathrm{T}} &= \sum_{ks} w_s \psi_{ks}^\dagger d_s + \mathrm{h.c.},
\end{aligned}
\tag{3.45}
$$

where $d_s^\dagger$ creates a spin-s electron in the dot, ϵ_0 is the energy of the quantum dot level, E_{Z} is the Zeeman splitting, and $\bar{\Delta}$ is the induced pair potential in the dot. We assume that the charging energy is much smaller than $\bar{\Delta}$ and is therefore neglected. Diagonalizing H_{D}, one has (up to a constant)

$$
H_{\mathrm{D}} = \left(\sqrt{\epsilon_0^2 + \bar{\Delta}^2} - E_{\mathrm{Z}} \right) a^\dagger a + \left(\sqrt{\epsilon_0^2 + \bar{\Delta}^2} + E_{\mathrm{Z}} \right) b^\dagger b, \tag{3.46}
$$

where $a = \cos(\alpha) d_\uparrow + \sin(\alpha) d_\downarrow^\dagger$, $b = \sin(\alpha) d_\uparrow^\dagger - \cos(\alpha) d_\downarrow$, and where $\cos(2\alpha) = \epsilon_0 / \sqrt{\epsilon_0^2 + \bar{\Delta}^2}$, $\sin(2\alpha) = \bar{\Delta} / \sqrt{\epsilon_0^2 + \bar{\Delta}^2}$. To have a single Andreev bound state at zero energy we can now tune the magnetic field to have $E_{\mathrm{Z}} = \sqrt{\epsilon_0^2 + \bar{\Delta}^2}$. Finally, projecting H_{T} onto the low-energy subspace described by a and $a^\dagger$ results in

$$
H_{\mathrm{T}} \simeq a^\dagger \sum_k \left(w_\uparrow^* \cos(\alpha) \psi_{k\uparrow} - w_\downarrow \sin(\alpha) \psi_{k\downarrow}^\dagger \right) + \mathrm{h.c.}, \tag{3.47}
$$

which is of exactly the same form as Eq. 3.8 with $\tilde{t}_\uparrow = w_\uparrow^* \cos(\alpha)$ and $\tilde{t}_\downarrow = -w_\downarrow \sin(\alpha)$.

3.C Finite-Size Effects

As mentioned in Secs. 3.2 and 3.3, an isolated MBS gives rise to a negative correlation P_{RL} (or $P_{\uparrow\downarrow}$ in the spin-resolved case). In a long but finite wire there can be a small overlap of the wave-functions of the MBSs at the two ends of the wire. It is instructive to examine the effect of this overlap on the spin-resolved current correlations.

In Fig. 3.C we concentrate on the spin-resolved case and present $P_{\uparrow\downarrow}$ as a function of bias voltage V for different lengths of the superconducting section L_{S}. The system parameters are otherwise the same as those in Fig. 3.2(c). Due to the finite overlap of the Majorana end states there is a small region at very low voltages where $P_{\uparrow\downarrow}$

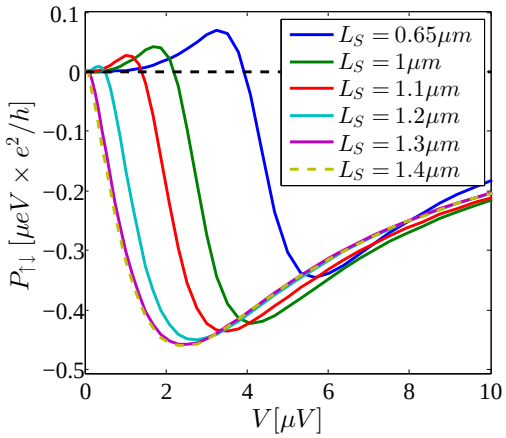

Figure 3.10: Spin-resolved current correlation $P_{\uparrow\downarrow}$ vs bias voltage V at $T = 0$ for different lengths of the superconducting section $L_{\rm S}$ for the case of a Majorana bound state. The region of positive $P_{\uparrow\downarrow}$ at small voltages is due to the overlap between the two Majorana bound states at the wire ends. As $L_{\rm S}$ increases the overlap becomes smaller. As a result the positive region becomes shorter and its maximum value becomes smaller.

becomes positive. As $L_{\rm S}$ increases, and the overlap between the MBSs decreases, the positive-$P_{\uparrow\downarrow}$ region becomes shorter and its maximum value becomes smaller.

This finite-size effect is related to the one described in Fig. 3.3(b). There we vary the overlap between the MBSs by changing the coherence length (increasing $E_{\rm Z}$) until reaching the limit where the overlap is maximal. Here, on the other hand, we vary the overlap by elongating the wire until reaching the limit where the overlap vanishes. Notice that in Fig. 3.3(b) we concentrate on values of B for which a zero-energy states is present in spite of the spatial overlap of the MBSs [cf. Fig. 3.2(a)]. Here, on the other hand, the overlap is accompanied by an energy splitting of the MBSs.

Chapter 4

Tuning Majorana Modes in a Quantum Dot Chain

4.1 Introduction

As was discussed in previous chapters, one of the most promising platforms for realizing and manipulating isolated Majorana Bound States (MBSs) is a proximity-coupled semiconductor wire under magnetic field [15, 16]. Indeed, recent experiments in semiconductor nanowires have observed transport signatures which are consistent with the presence of MBSs [25–28, 90, 122]. We also pointed out that uniquely associating these signatures with MBSs is not trivial as they can be the results of other physical mechanisms [91, 93, 94, 123–125] such as the Kondo effect or weak anti-localization. furthermore, even as evidences for MBSs in semiconductor wires are mounting, controlling and manipulating MBSs for the future purpose of braiding them is still a far away goal.

Indeed, several obstacles still exist in the way towards creating and manipulating robust MBSs. Disorder, for example, can have a detrimental effect on the robustness of the topological phase, since in the absence of time-reversal symmetry it may cause the induced superconducting gap to close [126]. This requires experiments to be performed in very clean systems. Additionally, the presence of multiple transmitting modes reduces the amount of control one has over such systems [71, 89, 114, 127], and the contribution of extra modes to conductance hinders the observation of MBSs [128]. Thus, nanowire experiments need setups in which only few modes contribute to conductance.

In this work we approach the problem of realizing systems in a non-trivial topological phase from a different angle. We wish to emulate the Kitaev chain model [11] which is the simplest model exhibiting unpaired Majorana bound states. The pro-

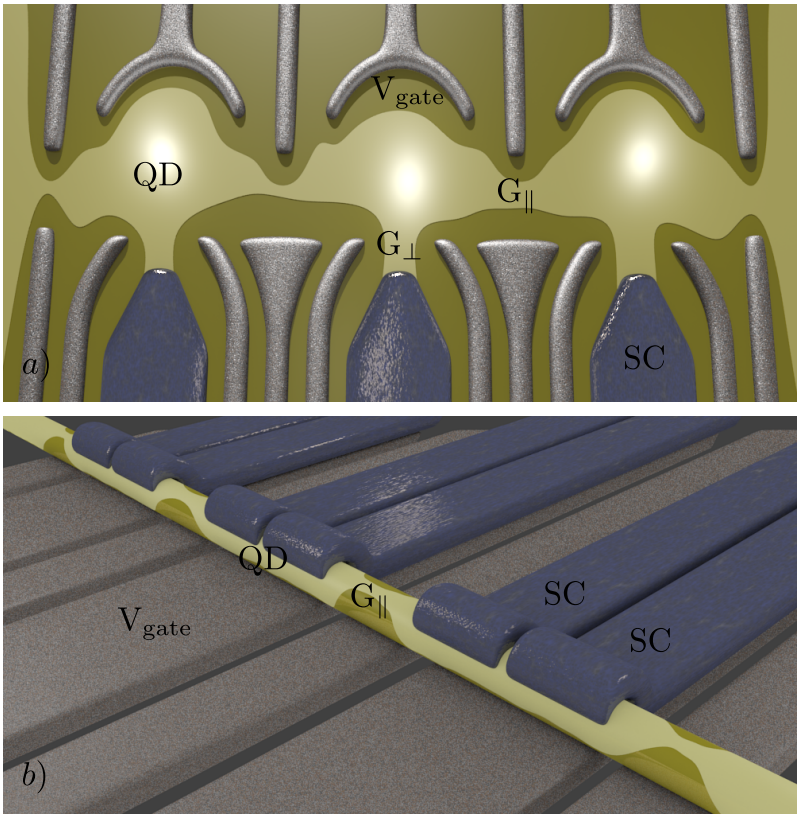

Figure 4.1: Examples of systems allowing implementation of a Kitaev chain. Panel (a): a chain of quantum dots in a 2DEG. The QDs are connected to each other, and to superconductors (labeled SC), by means of quantum point contacts. The first and the last dots are also coupled to external leads. The normal state conductance of quantum point contacts (QPCs) between adjacent dots or between the end dots and the leads is $G_{\parallel}$, and of the QPCs linking a dot to a superconductor is $G_{\perp}$. The confinement energy inside each QD can be controlled by varying the potential V_{gate}. Panel (b): Realization of the same setup using a nanowire, with the difference that each dot is coupled to two superconductors in order to control the strength of the superconducting proximity effect without the use of QPCs.

posed system consists of a chain of quantum dots (QDs) defined in a two-dimensional electron gas (2DEG) with spin orbit coupling, in proximity to superconductors and subjected to an external magnetic field. Our geometry enables us to control the parameters of the system to a great extent by varying gate potentials and superconducting phases. We will show how to fine tune the system to the so-called "sweet spot" in parameter space, where the MBSs are well-localized at the ends of the system, making the topological phase maximally robust. A sketch of our proposed setup is presented in Fig. 4.1(a).

The setup we propose and the tuning algorithm are not restricted to systems created in a two-dimensional electron gas. The essential components are the ability to form a chain of quantum dots and tune each dot separately. In semiconducting nanowires the dots can be formed from wire segments separated by gate-controlled tunnel barriers, and all the tuning can be done by gates, except for the coupling to a superconductor. This coupling, in turn, can be controlled by coupling two superconductors to each dot and applying a phase difference to these superconductors. The layout of a nanowire implementation of our proposal is shown in Fig. 4.1(b).

The geometry we propose has the advantage of eliminating many of the problems mentioned above. By using single level quantum dots, and also quantum point contacts (QPC) in the tunneling regime, we solve issues related to multiple transmitting modes. Additional problems, such as accidental closings of the induced superconducting gap due to disorder, are solved because our setup allows us to tune the system to a point where the topological phase is most robust, as we will show. We present a step-by-step tuning procedure which follows the behavior of the system in parallel to that expected for the Kitaev chain. As feedback required to control every step we use the resonant Andreev conductance, which allows to track the evolution of the system's energy levels. We expect that the step-by-step structure of the tuning algorithm should eliminate the large number of non-Majorana explanations of the zero bias peaks.

A related layout together with the idea of simulating a Kitaev chain was proposed recently by Sau and Das Sarma [129]. Although similar in nature, the geometry which we consider has several advantages. First of all, coupling the superconductors to the quantum dots in parallel, allows us to not rely on crossed Andreev reflection. More importantly, being able to control inter-dot coupling separately from all the other properties allows to address each dot or each segment of the chain electrically. This in turn makes it possible to perform the tuning of the system to the sweet spot regime in a scalable manner. This can be achieved by opening all the QPCs except for the ones that contact the desired dots.

We begin in Sec. 4.2 by briefly reviewing a generalized model of Kitaev chain, and identify the "sweet spot" in parameter space in which the MBSs are the most

localized. The system of coupled quantum dots is described in Sec. 4.3. For the purpose of making apparent the resemblance of the system to the Kitaev chain, we present a simple model which treats each dot as having a single spinful level. We then come up with a detailed tuning procedure describing how one can control the parameters of the simple model, in order to bring it to the desired point in parameter space. In Sec. 4.4 our tuning prescription is applied to the suggested system of a chain of QDs defined in a 2DEG, and it is shown using numerical simulations that at the end of the process the system is indeed in a robust topological phase. Finally, we conclude in Sec. 4.5.

4.2 Generalized Kitaev Chain

In order to realize unpaired Majorana bound states, we start from the Kitaev chain [11] generalized to the case where the on-site energies as well as the hopping terms are not uniform and can vary from site to site. The generalized Kitaev chain Hamiltonian is defined as

$$H_{\mathrm{K}} = \sum_{n=1}^{L-1} \left[\left(t_n e^{i\theta_n} a_{n+1}^\dagger a_n + \Delta_n e^{i\phi_n} a_{n+1}^\dagger a_n^\dagger + \mathrm{h.c.} \right) + \varepsilon_n a_n^\dagger a_n \right], \tag{4.1}$$

where a_n are fermion annihilation operators, ε_n are the on-site energies of these fermions, $t_n \exp(i\theta_n)$ are the hopping terms, and $\Delta_n \exp(i\phi_n)$ are the p-wave pairing terms.

The chain supports two Majorana bound states localized entirely on the first and the last sites, when (i): $\varepsilon_n = 0$, (ii): $\Delta_n = t_n$, and (iii) $\phi_{n+1} - \phi_n - \theta_{n+1} - \theta_n = 0$. The larger values of t_n lead to a larger excitation gap. The condition (iii) is equivalent, up to a gauge transformation, to the case where the hopping terms are all real, and the phases of the p-wave terms are uniform. The energy gap separating the Majorana modes from the first excited state then equals

$$E_{\mathrm{gap}} = 2 \min \left\{ t_n \right\}_n . \tag{4.2}$$

The above conditions (i)–(iii), constitute the "sweet spot" in parameter space to which we would like to tune our system. Since all of these conditions are local and only involve one or two sites, our tuning procedure includes isolating different parts of the system and monitoring their energy levels. For that future purpose we will use the expression for excitation energies of a chain of only two sites with $\varepsilon_1 = \varepsilon_2 = 0$:

$$E_{12} = \pm(t_1 \pm \Delta_1). \tag{4.3}$$

Exactly at the sweet spot, in order to couple MBSs formed at the ends of the chain, one needs to change at least L Hamiltonian parameters, where L is the length of the chain. This happens because any local perturbation would only delocalize Majorana between the dots on which it acts. Hence if a typical imperfection of the tuning due to presence of noise or the imperfection of tuning itself is of an order δ, then the residual coupling between Majoranas will be of order of $(\delta/t)^L$. Quadratic protection from noise for two such dots in the sweet spot regime was reported in Ref. [130]. While for quantum computation applications the length of chains required for sufficient noise tolerance may be relatively large, as we show in Sec. 4.4, in order to detect robust signatures of MBSs, three dots may be sufficient.

4.3 System Description and the Tuning Algorithm

The most straightforward way to emulate the Kitaev chain is to create an array of spinful quantum dots, and apply a sufficiently strong Zeeman field such that only one spin state stays close to the Fermi level. Then the operators of these spin states span the basis of the Hilbert space of the Kitaev chain. If we require normal hopping between the dots and do not utilize crossed Andreev reflection, then in order to have both t_n and Δ_n nonzero we need to break the particle number conservation and spin conservation. The former is achieved by coupling each dot to a superconductor, the latter can be achieved by spatially varying Zeeman coupling [131, 132], or more conventionally by using a material with a sufficiently strong spin-orbit coupling. Examples of implementation of such a chain of quantum dots in a two dimensional electron gas and in semiconducting nanowires are shown in Fig. 4.1.

We neglect all the levels in the dots except for the one closest to the Fermi level, which is justified if the level spacing in the dot is larger than all the other Hamiltonian terms. We neglect the Coulomb blockade, since we assume that the conductance from the dot to the superconductor is larger than the conductance quantum [133]. We consider a single Kramers doublet per dot with creation and annihilation operators $c^\dagger_{n,s}$ and $c_{n,s}$, with n the dot number and s the spin degree of freedom. Since we consider dots with spin-orbit interaction, $c_{n,s}$ is not an eigenstate of spin. Despite that, only singlet superconducting pairing is possible between $c_{n,s}$ and $c_{n,s'}$ as long as the time reversal symmetry breaking in a single dot is weak. By applying a proper SU(2) rotation in the s-s' space we may choose the Zeeman field to point in z-direction in each dot. As long as the Zeeman field does not change the wave functions of the spin states the superconducting coupling stays s-wave. The general form of the BdG Hamiltonian describing such a chain of spinful single-level

dots is thus given by:

$$H_{\mathrm{S}} = \sum_{n,s,s'} \Big\{ \left(\mu_n \delta_{s,s'} + E_{\mathrm{Z}} \sigma^z_{s,s'}\right) c^\dagger_{n,s} c_{n,s'} + \frac{1}{2}\left(\Delta_{\mathrm{ind},n} e^{i\Phi_n} i\sigma^y_{s,s'} c^\dagger_{n,s} c^\dagger_{n,s'} + \mathrm{h.c.}\right) + \left[w_n \left(e^{i\boldsymbol{\lambda}_n \boldsymbol{\sigma}}\right)_{s,s'} c^\dagger_{n,s} c_{n+1,s'} + \mathrm{h.c.}\right] \Big\}, \tag{4.4}$$

where σ_i are Pauli matrices in spin space. The physical quantities entering this Hamiltonian are the chemical potential μ_n, the Zeeman energy E_{Z}, the proximity-induced pairing $\Delta_{\mathrm{ind},n}\exp(i\Phi_n)$, and the inter-dot hopping w_n. The vector $\boldsymbol{\lambda}_n$ characterizes the amount of spin rotation happening during a hopping between the two neighboring dots (the spin rotates by a $2|\lambda|$ angle). This term may be generated either by a spin-orbit coupling, or by a position-dependent spin rotation, required to make the Zeeman field point in the local z-direction [131, 132, 134]. The induced pairing in each dot $\Delta_{\mathrm{ind},n}\exp(i\Phi_n)$ is not to be confused with the p-wave pairing term $\Delta_n \exp(i\phi_n)$ appearing in the Kitaev chain Hamiltonian (4.1).

In order for the dot chain to mimic the behavior of the Kitaev chain in the sweet spot, each dot should have a single fermion level with zero energy, so that $\varepsilon_n = 0$. Diagonalizing a single dot Hamiltonian yields the condition for this to happen:

$$\mu_n = \sqrt{E_{\mathrm{Z}}^2 - \Delta_{\mathrm{ind},n}^2}. \tag{4.5}$$

When this condition is fulfilled, each dot has two fermionic excitations

$$a_n = \frac{e^{i\frac{\Phi_n}{2}}}{\sqrt{2E_{\mathrm{Z}}}}\left(\sqrt{E_{\mathrm{Z}} - \mu_n}\; c^\dagger_{n\uparrow} - e^{-i\Phi_n}\sqrt{E_{\mathrm{Z}} + \mu_n}\; c_{n\downarrow}\right) \tag{4.6}$$

$$b_n = \frac{e^{i\frac{\Phi_n}{2}}}{\sqrt{2E_{\mathrm{Z}}}}\left(\sqrt{E_{\mathrm{Z}} - \mu_n}\; c^\dagger_{n\downarrow} + e^{-i\Phi_n}\sqrt{E_{\mathrm{Z}} + \mu_n}\; c_{n\uparrow}\right). \tag{4.7}$$

The energy of a_n is zero, the energy of b_n is $2E_{\mathrm{Z}}$. If the hopping is much smaller than the energy of the excited state, $w_n \ll E_{\mathrm{Z}}$, we may project the Hamiltonian (4.4) onto the Hilbert space spanned by a_n. The resulting projected Hamiltonian is identical to the Kitaev chain Hamiltonian of Eq. (4.1), with the following effective parameters:

$$\begin{aligned}
&\varepsilon_n = 0,\\
&t_n e^{i\theta_n} = w_n\left(\cos\lambda_n + i\sin\lambda_n\cos\rho_n\right)\times\\
&\qquad\left[\sin\left(\alpha_{n+1}+\alpha_n\right)\cos(\delta\Phi_n/2) + i\cos\left(\alpha_{n+1}-\alpha_n\right)\sin(\delta\Phi_n/2)\right],\\
&\Delta_n e^{i\phi_n} = i w_n \sin\lambda_n \sin\rho_n e^{i\xi_n}\times\\
&\qquad\left[\cos\left(\alpha_{n+1}+\alpha_n\right)\cos\left(\delta\Phi_n/2\right) + i\,\sin\left(\alpha_{n+1}-\alpha_n\right)\sin\left(\delta\Phi_n/2\right)\right],
\end{aligned} \tag{4.8}$$

where

$$\mu_n = E_{\mathrm{Z}} \sin(2\alpha_n),\ \Delta_{\mathrm{ind},n} = E_{\mathrm{Z}} \cos(2\alpha_n), \tag{4.9}$$

$$\boldsymbol{\lambda}_n = \lambda_n \left(\sin\rho_n \cos\xi_n,\ \sin\rho_n \sin\xi_n,\ \cos\rho_n\right)^T, \tag{4.10}$$

and $\delta\Phi_n = \Phi_n - \Phi_{n+1}$.

It is possible to extract most of the parameters of the dot Hamiltonian from level spectroscopy, and then tune the effective Kitaev chain Hamiltonian to the sweet spot. The tuning, however, becomes much simpler if two out of three of the dot linear dimensions are much smaller than the spin-orbit coupling length. Then the direction of spin-orbit coupling does not depend on the dot number, and as long as the magnetic field is perpendicular to the spin-orbit field, the phase of the prefactors in Eq. (4.8) becomes position-independent. Additionally, if the dot size is not significantly larger than the spin-orbit length, the signs of these prefactors are constant. This ensures that if $\delta\Phi_n = 0$, the phase matching condition of the Kitaev chain is fulfilled. Since $\delta\Phi_n = 0$ leads to both t_n and Δ_n having a minimum or maximum as a function of $\delta\Phi_n$, this point is straightforward to find. The only remaining condition, $t_n = \Delta_n$ at $\delta\Phi = 0$, requires that $\alpha_n + \alpha_{n+1} = \lambda_n$.

The above calculation leads to the following tuning algorithm:

1. Open all the QPCs, except for two contacting a single dot. By measuring conductance while tuning the gate voltage of a nearby gate, ensure that there is a resonant level at zero bias. After repeating for each dot the condition $\varepsilon_n = 0$ is fulfilled.

2. Open all the QPCs except the ones near a pair of neighboring dots. Keeping the gate voltages tuned such that $\varepsilon_n = 0$, vary the phase difference between the neighboring superconductors until the lowest resonant level is at its minimum as a function of phase difference, and the next excited level at a maximum. This ensures that the phase tuning condition $\phi_{n+1} - \phi_n - \theta_{n+1} - \theta_n = 0$ is fulfilled. Repeat for every pair of neighboring dots.

3. Start from one end of the chain, and isolate pairs of dots like in the previous step. In the pair of n-th and $n+1$-st dots tune simultaneously the coupling of the $n+1$-st dot to the superconductor and the chemical potential in this dot, such that ε_{n+1} stays equal to 0. Find the values of these parameters such that a level at zero appears in two dots when they are coupled. After that proceed to the following pair.

Having performed the above procedures, the coupling between all of the dots in the chain is resumed, at which point we expect the system to be in a robust

topological phase, with two MBSs located on the first and last dots. In practice one can also resume the coupling gradually by, for instance, isolating triplets of adjacent dots, making sure they contain a zero-energy state, and making fine-tuning corrections if necessary, and so on.

4.4 Testing the Tuning Procedure by Numerical Simulations

We now test the tuning procedure by applying it to a numerical simulation of a chain of three QDs in a 2DEG. The two-dimensional BdG Hamiltonian describing the entire system of the QD chain reads:

$$\begin{aligned}\mathcal{H}_{\mathrm{QDC}} = &\left[\frac{\mathbf{p}^2}{2m} + V(x,y)\right]\tau^z + \lambda_{\mathrm{R}}(\sigma^x p_y - \tau_z\sigma^y p_x) + E_{\mathrm{Z}}\tau^z\sigma^z \\ &+ \Delta_{\mathrm{ind}}\left[\cos(\Phi)\tau_y + \sin(\Phi)\tau^x\right]\sigma^y.\end{aligned} \tag{4.11}$$

Here, σ_i and τ_i are Pauli matrices acting on the spin and particle-hole degrees of freedom respectively. The term $V(x,y)$ describes both potential fluctuations due to disorder, and the confinement potential introduced by the gates. The second term represents Rashba spin-orbit coupling, $\Delta_{\mathrm{ind}}(x,y)\cdot\exp\left[\Phi(x,y)\right]$ is the s-wave superconductivity induced by the coupled superconductors, and E_{Z} is the Zeeman splitting due to the magnetic field. Full description of the tight-binding equations used in the simulation is presented in Appendix 4.A.

The chemical potential of the dot levels μ_n is tuned by changing the potential $V(x,y)$. For simplicity we used a constant potential V_n added to the disorder potential, such that $V(x,y) = V_n + V_0(x,y)$ in each dot. Varying the magnitude of $\Delta_{\mathrm{ind},n}$ is done by changing conductance $G_\perp$ of the quantum point contacts, which control the coupling between the dots and the superconductors. Finally, varying the superconducting phase $\Phi(x,y)$ directly controls the parameter Φ_n of the dot to which the superconductor is coupled, although they need not be the same.

The tuning algorithm required monitoring the energy levels of different parts of the system. This can be achieved by measuring the resonant Andreev conductance from one of the leads. The Andreev conductance is given by [23, 24]

$$G = G_0\left[N - \mathrm{Tr}(r_{\mathrm{ee}}r_{\mathrm{ee}}^\dagger) + \mathrm{Tr}(r_{\mathrm{he}}r_{\mathrm{he}}^\dagger)\right], \tag{4.12}$$

where $G_0 = e^2/h$, N is the number of modes in a given lead, r_{ee} is the normal reflection matrices, and r_{he} is the Andreev reflection matrices. Accessing parts of

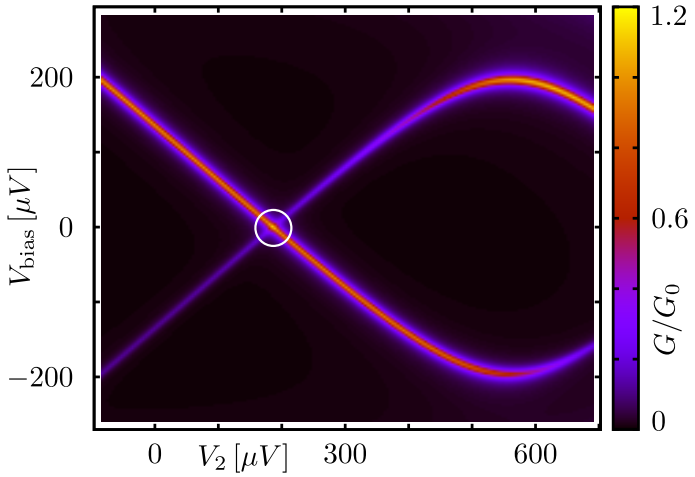

Figure 4.2: Andreev conductance measured from the left lead as a function of bias voltage and QD potential (measured relative to quarter filling) for the second dot. Changing the chemical potential allows to tune quasi-bound states to zero energy (white circle).

the chain (such as a single dot or a pair of dots) can be done by opening all inter-dot QPCs, and closing all the ones between dots and superconductors, except for part of the system that is of interest.

We begin by finding such widths of QPCs that $G_{\parallel} \approx 0.02$ and $G_{\perp} \approx 4G_0$. This ensures that conductance between adjacent dots, is in tunneling regime and that the dots are strongly coupled to the superconductors such that the effect of Coulomb blockade is reduced [133]. The detailed properties of QPCs are described in Appendix 4.A and their conductance is shown in Fig. 4.8.

First step: tuning chemical potential. We sequentially isolate each dot, and change the dot potential V_n. The Andreev conductance as a function of V_n and bias voltage for the second dot is shown in Fig. 4.2. We tune V_n to the value where a conductance resonance exists at zero bias. This is repeated for each of the dots and ensures that $\mu_n = 0$.

Second step: tuning the superconducting phases. We now set the phases of the induced pairing potentials Φ_n to constant. As explained in the previous section, this occurs when Δ_n and t_n experience their maximal and minimal values. According to Eq. (4.3) this happens when the separation between the energy levels of the pair of dots subsection is maximal. Fig. 4.3 shows the evolution of these levels as a function of the phase difference between the two superconductors. The condition $\delta\Phi_1 = 0$ is then satisfied at the point where their separation is maximal.

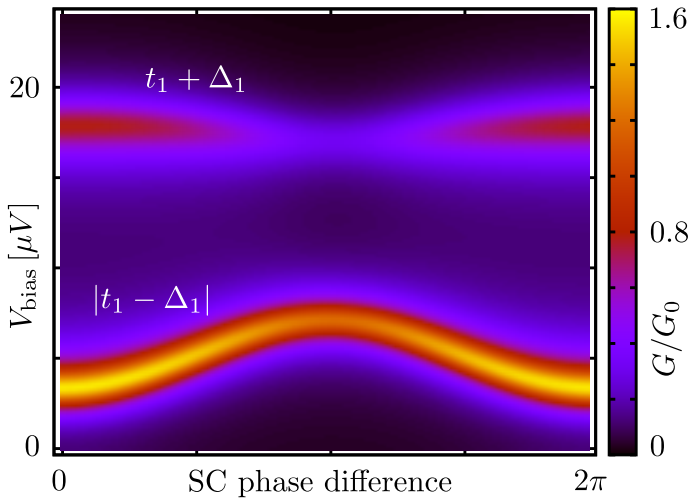

Figure 4.3: Conductance as a function of bias voltage and superconducting phase difference for a two-dot system. The two lowest energy levels are given by Eq. (4.3) of a two site Kitaev chain, as indicated. At the point where their separation is maximal (SC phase difference 0 in the plot), the phase difference $\delta\Phi_n$ of the induced superconducting gaps vanishes.

Third step: tuning the couplings. Finally we tune $t_n = \Delta_n$. This is achieved by varying $G_\perp$, while tracking the Andreev conductance peak corresponding to the $t_n - \Delta_n$ eigenvalue of the Kitaev chain we are emulating. After every change of $G_\perp$ we readjust V_n in order to make sure that the condition $\varepsilon_n = 0$ (or equivalently $E_{\rm Z}^2 = \mu_n^2 + \Delta_n^2$) is maintained. This is necessary because not just Δ_n, but also μ_n depend on $G_\perp$. Therefore, successive changes of $G_\perp$ and V_n are performed until the smallest bias peak is located at zero bias. The tuning steps of the first two dots are shown in Fig. 4.4. We repeat steps 2 and 3 for each pair of dots in the system.

Finally, having full all three conditions required for a robust topologically non-trivial phase, we probe the presence of localized Majorana bound state in the full three-dot system by measuring Andreev conductance (see Fig. 4.5). In this specific case, the height of the zero bias peak is approximately $1.85\,G_0$, signaling that the end states are well but not completely decoupled. Increasing the transparency of the QPC connecting the first dot to the lead brings this value to $G = 1.98\,G_0$.

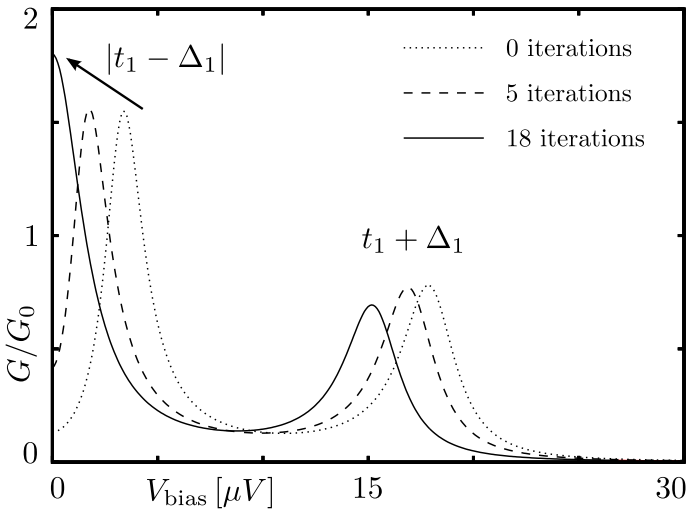

Figure 4.4: Conductance as a function of bias voltage during simultaneous tuning of $G_\perp$ and V_n for the first pair of dots. The three different plots represent the situation before (dotted line), at an intermediate stage (dashed line), and after (solid line) the tuning. The arrow indicates the evolution of the first peak upon tuning, and the number of successive changes of $G_\perp$ and V_n are shown for each curve. By bringing the first peak to zero, the third tuning step is achieved.

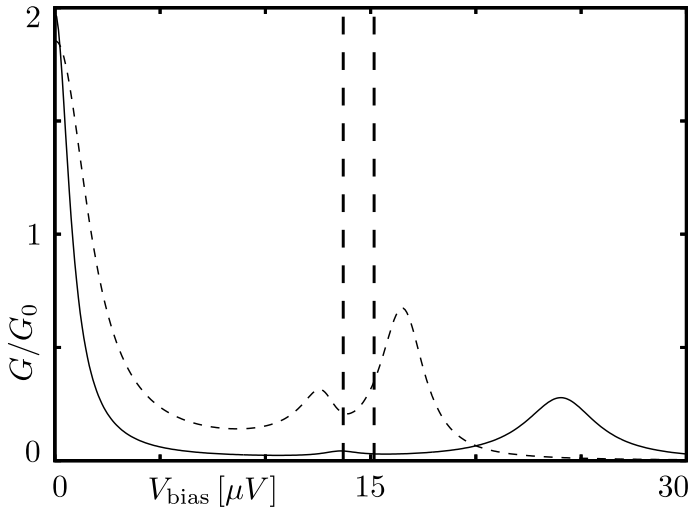

Figure 4.5: Conductance as a function of bias voltage for a system composed of three tuned quantum dots (dashed line). The zero bias peak signals the presence of Majorana bound states at the ends of the chain. The first and second excited states are consistent with those expected for a three-site Kitaev chain, namely $E_1 = 2t_1$ and $E_2 = 2t_2$ (vertical dashed lines), given the measured values of $t_1 = \Delta_1$ and $t_2 = \Delta_2$, obtained after finalizing the two dot tuning process. As described in the text, after increasing the transparency of the lead QPC leads to a zero bias peak having a height $G = 1.98G_0$ (solid line).

4.5 Discussion

In conclusion, we have demonstrated how to tune a linear array of quantum dots coupled to superconductors in presence of Zeeman field and spin-orbit coupling to resemble the Kitaev chain that hosts Majorana bound states at its ends. Furthermore, we have presented a detailed procedure by which the system is brought to the so-called "sweet spot" in parameter space, where the Majorana bound states are the most localized. This procedure involves varying the gates potentials and superconducting phases, as well as monitoring of the excitation spectrum of the system by means of resonant Andreev conductance.

We have tested our procedure using numerical simulations of a system of three QDs, defined in a 2DEG, and found that it works in systems with experimentally reachable parameters. It can be also applied to systems where quantum dots are defined by other means, for example formed in a one-dimensional InAs or InSb wire.

The setup we propose can also be extended to more complicated geometries which include T-junctions of such chains. Benefiting from the high tunability of the system and the localization of the MBSs, it might then be possible to implement braiding [113, 135] and demonstrate their non-Abelian nature.

Appendices for Chapter 4

4.A System Parameters in Numerical Simulations

In this section, we describe the parameters used throughout the numerical simulations. The quantum dots and quantum point contacts are modeled using a tight-binding model defined on a square lattice, with leads and superconductors taken as semi-infinite.

The characteristic length and energy scales of this system are the spin-orbit length $l_{\mathrm{SO}} = 1/m\lambda_{\mathrm{R}}$, and the spin-orbit energy $E_{\mathrm{SO}} = m\lambda_{\mathrm{R}}^2/2$. We simulate an InAs system in which the effective electron mass is $m = 0.015m_{\mathrm{e}}$, where m_{e} is the bare electron mass, taking values of $E_{\mathrm{SO}} = 0.5\,\mathrm{K} = 43\,\mu\mathrm{eV}$ and $l_{\mathrm{SO}} = 250\,\mathrm{nm}$.

We consider a setup composed of three quantum dots, like the one shown in Fig. 4.6. Each of the three dots has a length of $L_{\mathrm{DOT}} = 208\,\mathrm{nm}$ and a width $W_{\mathrm{DOT}} = 104\,\mathrm{nm}$. Quantum point contacts have a longitudinal dimension of $L_{\mathrm{QPC}} = 42\,\mathrm{nm}$, which is the same as the Fermi wavelength at quarter filling.

The value of the hopping integral becomes $t = 1/(2ma^2) = 55.8\,\mathrm{meV}$, with $a = 7\,\mathrm{nm}$. Disorder is introduced in the form of random uncorrelated onsite potential fluctuations, leading to a mean free path $l_{\mathrm{mfp}} = 218.8\,\mathrm{nm}$. The system is placed in a perpendicular magnetic field characterized by a Zeeman splitting $E_{\mathrm{Z}} = 336\,\mu\mathrm{eV}$, which, given a g-factor of $35K/T$, corresponds to a magnetic field $B_z = 111\,\mathrm{mT}$. Each dot is additionally connected to a superconductor characterized by a pairing potential $|\Delta_{\mathrm{SC}}| = 0.86\,\mathrm{meV}$.

The potential profile across a quantum point contact is given by

$$V_{\mathrm{QPC}}(x) = \frac{\widetilde{h}}{2}\left\{2 - \tanh\left[\frac{\widetilde{s}}{\widetilde{L}}\left(x + \frac{\widetilde{w}}{2}\right)\right] + \tanh\left[\frac{\widetilde{s}}{\widetilde{L}}\left(x - \frac{\widetilde{w}}{2}\right)\right]\right\}, \tag{4.13}$$

where $x \in [-\widetilde{L}/2, \widetilde{L}/2]$ is the transverse coordinate across the quantum point contact, $\widetilde{h}$ is the maximum height of V_{QPC}, $\widetilde{s}$ fixes the slope at which the potential changes, and $\widetilde{w}$ is used to tune the QPC transparency. Two examples of potential profiles are shown in Fig. 4.7.

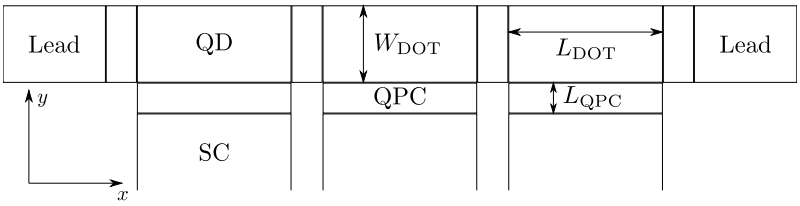

Figure 4.6: Geometry of the quantum dot chain. The quantum dots have a width W_{DOT} and length equal to L_{DOT}. Quantum point contacts have a longitudinal size L_{QPC} and a transverse dimension equal to either L_{DOT} or W_{DOT}. Leads are semi-infinite in the x direction, and superconductors are modeled as semi-infinite systems in the y direction.

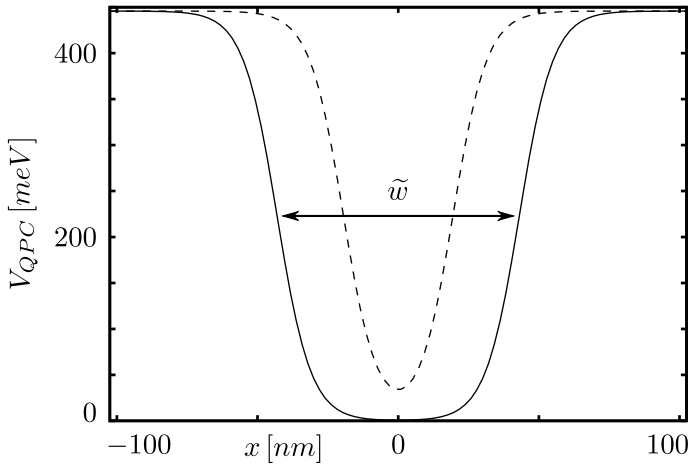

Figure 4.7: Potential profile $V_{\mathrm{QPC}}(x)$ across the transverse direction of a quantum point contact. For the maximum value of this potential, no states are available for quasiparticles in the 2DEG. The two curves show potential profiles for two different QPC transparencies, corresponding to $\widetilde{s} = 17$ and $\widetilde{w} = 87.4$, 39.5 nm for the solid and dashed curves respectively.

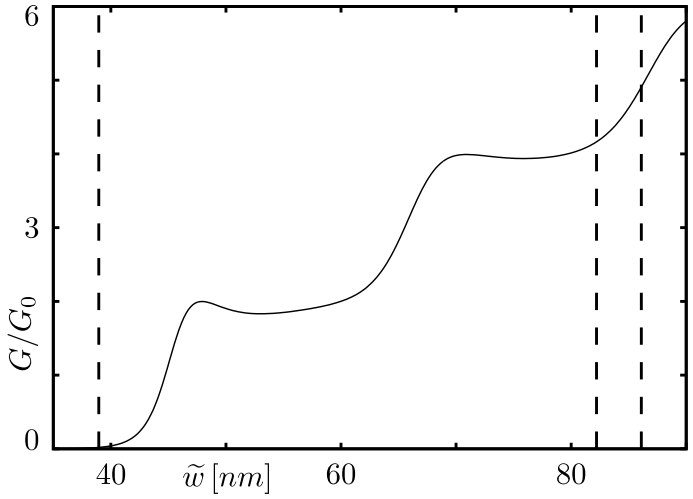

Figure 4.8: Conductance of a quantum point contact as a function of $\widetilde{w}$ of Eq. (4.13), for a single QPC. The vertical lines indicate the values at which QPCs are set after tuning. The inter-dot QPCs are all set to the tunneling regime while the ones connecting the dots to the superconductors are set to higher transparencies.

Bibliography

[1] K. v. Klitzing, G. Dorda, and M. Pepper, Phys. Rev. Lett. **45**, 494 (1980).

[2] D. J. Thouless, M. Kohmoto, M. P. Nightingale, and M. den Nijs, Phys. Rev. Lett. **49**, 405 (1982).

[3] R. B. Laughlin, Phys. Rev. B **23**, 5632 (1981).

[4] F. D. M. Haldane, Phys. Rev. Lett. **61**, 2015 (1988).

[5] C. L. Kane and E. J. Mele, Phys. Rev. Lett. **95**, 226801 (2005).

[6] A. P. Schnyder, S. Ryu, A. Furusaki, and A. W. W. Ludwig, Phys. Rev. B **78**, 195125 (2008).

[7] A. Kitaev, in *AIP Conf. Proc.*, Vol. 1134 (2009) p. 22.

[8] S. Ryu, A. P. Schnyder, A. Furusaki, and A. W. W. Ludwig, New J. Phys. **12**, 065010 (2010).

[9] E. Majorana, Il Nuovo Cimento (1924-1942) **14**, 171 (1937).

[10] F. Wilczek, Nature Physics **5**, 614 (2009).

[11] A. Kitaev, Phys. Usp. **44**, 131 (2001).

[12] L. Fu and C. L. Kane, Phys. Rev. Lett. **100**, 096407 (2008).

[13] L. Fu and C. L. Kane, Phys. Rev. B **79**, 161408 (2009).

[14] J. D. Sau, R. M. Lutchyn, S. Tewari, and S. Das Sarma, Phys. Rev. Lett. **104**, 040502 (2010).

[15] R. M. Lutchyn, J. D. Sau, and S. Das Sarma, Phys. Rev. Lett. **105**, 077001 (2010).

[16] Y. Oreg, G. Refael, and F. von Oppen, Phys. Rev. Lett. **105**, 177002 (2010).

[17] A. Andreev, Zh. Eksp. Teor. Fiz. **46**, 1823 (1964).

[18] C. J. Bolech and E. Demler, Phys. Rev. Lett. **98**, 237002 (2007).

[19] K. T. Law, P. A. Lee, and T. K. Ng, Phys. Rev. Lett. **103**, 237001 (2009).

[20] L. Fidkowski, J. Alicea, N. H. Lindner, R. M. Lutchyn, and M. P. A. Fisher, Phys. Rev. B **85**, 245121 (2012).

[21] J. J. He, T. K. Ng, P. A. Lee, and K. T. Law, Phys. Rev. Lett. **112**, 037001 (2014).

[22] C. W. J. Beenakker, Ann. Rev. Condens. Matt. Phys. **4**, 113 (2013).

[23] A. Shelankov, JETP Lett., **32**, 111 (1980).

[24] G. E. Blonder, M. Tinkham, and T. M. Klapwijk, Phys. Rev. B **25**, 4515 (1982).

[25] V. Mourik, K. Zuo, S. Frolov, S. Plissard, E. Bakkers, and L. Kouwenhoven, Science **336**, 1003 (2012).

[26] M. Deng, C. Yu, G. Huang, M. Larsson, P. Caroff, and H. Xu, Nano Lett. **12**, 6414 (2012).

[27] A. Das, Y. Ronen, Y. Most, Y. Oreg, M. Heiblum, and H. Shtrikman, Nat. Phys. **8**, 887 (2012).

[28] H. O. H. Churchill, V. Fatemi, K. Grove-Rasmussen, M. T. Deng, P. Caroff, H. Q. Xu, and C. M. Marcus, Phys. Rev. B **87**, 241401 (2013).

[29] A. D. K. Finck, D. J. Van Harlingen, P. K. Mohseni, K. Jung, and X. Li, Phys. Rev. Lett. **110**, 126406 (2013).

[30] X.-L. Qi and S.-C. Zhang, Rev. Mod. Phys. **83**, 1057 (2011).

[31] B. A. Bernevig, T. L. Hughes, and S.-C. Zhang, Science **314**, 1757 (2006).

[32] M. König, S. Wiedmann, C. Brüne, A. Roth, H. Buhmann, L. W. Molenkamp, X.-L. Qi, and S.-C. Zhang, Science **318**, 766 (2007).

[33] A. Altland and M. R. Zirnbauer, Phys. Rev. B **55**, 1142 (1997).

[34] J. Alicea, Rep. Prog. Phys. **75**, 076501 (2012).

[35] X.-L. Qi, T. L. Hughes, S. Raghu, and S.-C. Zhang, Phys. Rev. Lett. **102**, 187001 (2009).

[36] X.-L. Qi, T. L. Hughes, and S.-C. Zhang, Phys. Rev. B **81**, 134508 (2010).

[37] K. Wölms, A. Stern, and K. Flensberg, Phys. Rev. Lett. **113**, 246401 (2014).

[38] K. Wölms, A. Stern, and K. Flensberg, Phys. Rev. B **93**, 045417 (2016).

[39] A. Keselman, L. Fu, A. Stern, and E. Berg, Phys. Rev. Lett. **111**, 116402 (2013).

[40] A. Keselman and E. Berg, Phys. Rev. B **91**, 235309 (2015).

[41] J. Alicea, Phys. Rev. B **81**, 125318 (2010).

[42] S. Nadj-Perge, I. K. Drozdov, J. Li, H. Chen, S. Jeon, J. Seo, A. H. MacDonald, B. A. Bernevig, and A. Yazdani, Science **346**, 602 (2014).

[43] R. Pawlak, M. Kisiel, J. Klinovaja, T. Meier, S. Kawai, T. Glatzel, D. Loss, and E. Meyer, NPJ Quantum Information **2**, 16035 (2016).

[44] M. Ruby, F. Pientka, Y. Peng, F. von Oppen, B. W. Heinrich, and K. J. Franke, Phys. Rev. Lett. **115**, 197204 (2015).

[45] A. Haim, E. Berg, K. Flensberg, and Y. Oreg, Phys. Rev. B **94**, 161110 (2016).

[46] A. Haim, K. Wölms, E. Berg, Y. Oreg, and K. Flensberg, Phys. Rev. B **94**, 115124 (2016).

[47] A. Haim, A. Keselman, E. Berg, and Y. Oreg, Phys. Rev. B **89**, 220504 (2014).

[48] E. Gaidamauskas, J. Paaske, and K. Flensberg, Phys. Rev. Lett. **112**, 126402 (2014).

[49] J. Klinovaja and D. Loss, Phys. Rev. B **90**, 045118 (2014).

[50] J. Klinovaja, A. Yacoby, and D. Loss, Phys. Rev. B **90**, 155447 (2014).

[51] J. Danon and K. Flensberg, Phys. Rev. B **91**, 165425 (2015).

[52] C. J. Pedder, T. Meng, R. P. Tiwari, and T. L. Schmidt, arXiv:1507.08881 .

[53] C. L. M. Wong and K. T. Law, Phys. Rev. B **86**, 184516 (2012).

[54] F. Zhang, C. L. Kane, and E. J. Mele, Phys. Rev. Lett. **111**, 056402 (2013).

[55] S. Nakosai, J. C. Budich, Y. Tanaka, B. Trauzettel, and N. Nagaosa, Phys. Rev. Lett. **110**, 117002 (2013).

[56] J. P. Dahlhaus, B. Béri, and C. W. J. Beenakker, Phys. Rev. B **82**, 014536 (2010).

[57] C. Schrade, A. A. Zyuzin, J. Klinovaja, and D. Loss, Phys. Rev. Lett. **115**, 237001 (2015).

[58] L. Fu and E. Berg, Phys. Rev. Lett. **105**, 097001 (2010).

[59] S. Nakosai, Y. Tanaka, and N. Nagaosa, Phys. Rev. Lett. **108**, 147003 (2012).

[60] S. Deng, L. Viola, and G. Ortiz, Phys. Rev. Lett. **108**, 036803 (2012).

[61] J. Wang, Y. Xu, and S.-C. Zhang, Phys. Rev. B **90**, 054503 (2014).

[62] P. M. R. Brydon, S. Das Sarma, H.-Y. Hui, and J. D. Sau, Phys. Rev. B **90**, 184512 (2014).

[63] G. E. Volovik, *The Universe in a Helium Droplet* (Oxford, 2003).

[64] E. Dumitrescu, B. Roberts, S. Tewari, J. D. Sau, and S. Das Sarma, Phys. Rev. B **91**, 094505 (2015).

[65] P. Kotetes, Phys. Rev. B **92**, 014514 (2015).

[66] I. C. Fulga, F. Hassler, A. R. Akhmerov, and C. W. J. Beenakker, Phys. Rev. B **83**, 155429 (2011).

[67] J. C. Budich and E. Ardonne, Phys. Rev. B **88**, 134523 (2013).

[68] I. Mandal, arXiv preprint arXiv:1503.06804 (2015).

[69] L. Fu and C. L. Kane, Phys. Rev. B **74**, 195312 (2006).

[70] O. Motrunich, K. Damle, and D. A. Huse, Phys. Rev. B **63**, 224204 (2001).

[71] P. W. Brouwer, M. Duckheim, A. Romito, and F. von Oppen, Phys. Rev. Lett. **107**, 196804 (2011).

[72] R. Shankar, Rev. Mod. Phys. **66**, 129 (1994).

[73] N. Kainaris and S. T. Carr, Phys. Rev. B **92**, 035139 (2015).

[74] S. Hart, H. Ren, T. Wagner, P. Leubner, M. Mühlbauer, C. Brüne, H. Buhmann, L. W. Molenkamp, and A. Yacoby, Nat. Phys. **10**, 638 (2014).

[75] A. V. Moroz and C. H. W. Barnes, Phys. Rev. B **60**, 14272 (1999).

[76] A. R. Akhmerov, J. P. Dahlhaus, F. Hassler, M. Wimmer, and C. W. J. Beenakker, Phys. Rev. Lett. **106**, 057001 (2011).

[77] S. Tewari and J. D. Sau, Phys. Rev. Lett. **109**, 150408 (2012).

[78] E. Dumitrescu, J. D. Sau, and S. Tewari, Phys. Rev. B **90**, 245438 (2014).

[79] A. Haim, E. Berg, F. von Oppen, and Y. Oreg, Phys. Rev. Lett. **114**, 166406 (2015).

[80] A. Haim, E. Berg, F. von Oppen, and Y. Oreg, Phys. Rev. B **92**, 245112 (2015).

[81] J. Li, W. Pan, B. A. Bernevig, and R. M. Lutchyn, Phys. Rev. Lett. **117**, 046804 (2016).

[82] S. B. Chung, J. Horowitz, and X.-L. Qi, Phys. Rev. B **88**, 214514 (2013).

[83] F. Zhang and C. L. Kane, Phys. Rev. B **90**, 020501 (2014).

[84] C. L. Kane and F. Zhang, Physica Scrip. **2015**, 014011 (2015).

[85] M.-T. Rieder, P. W. Brouwer, and i. d. I. m. c. Adagideli, Phys. Rev. B **88**, 060509 (2013).

[86] C. W. J. Beenakker, Phys. Rev. Lett. **67**, 3836 (1991).

[87] J. Bardeen, Phys. Rev. Lett. **6**, 57 (1961).

[88] J. D. Sau, R. M. Lutchyn, S. Tewari, and S. Das Sarma, Phys. Rev. B **82**, 094522 (2010).

[89] T. D. Stanescu, R. M. Lutchyn, and S. Das Sarma, Phys. Rev. B **84**, 144522 (2011).

[90] S. Albrecht, A. Higginbotham, M. Madsen, F. Kuemmeth, T. Jespersen, J. Nygård, P. Krogstrup, and C. Marcus, Nature **531**, 206 (2016).

[91] D. I. Pikulin, J. P. Dahlhaus, M. Wimmer, H. Schomerus, and C. W. J. Beenakker, New J. Phys. **14**, 125011 (2012).

[92] G. Kells, D. Meidan, and P. W. Brouwer, Phys. Rev. B **86**, 100503 (2012).

[93] J. Liu, A. C. Potter, K. T. Law, and P. A. Lee, Phys. Rev. Lett. **109**, 267002 (2012).

[94] S. Sasaki, S. De Franceschi, J. Elzerman, W. Van der Wiel, M. Eto, S. Tarucha, and L. Kouwenhoven, Nature (London) **405**, 764 (2000).

[95] D. Bagrets and A. Altland, Phys. Rev. Lett. **109**, 227005 (2012).

[96] E. J. Lee, X. Jiang, M. Houzet, R. Aguado, C. M. Lieber, and S. De Franceschi, Nat. Nanotech. **9**, 79 (2014).

[97] M. P. Anantram and S. Datta, Phys. Rev. B **53**, 16390 (1996).

[98] T. Posske and B. Trauzettel, Phys. Rev. B **89**, 075108 (2014).

[99] A. Golub and B. Horovitz, Phys. Rev. B **83**, 153415 (2011).

[100] D. S. Fisher and P. A. Lee, Phys. Rev. B **23**, 6851 (1981).

[101] S. Iida, H. A. Weidenmüller, and J. Zuk, Ann. Phys. **200**, 219 (1990).

[102] M. Leijnse and K. Flensberg, Phys. Rev. Lett. **107**, 210502 (2011).

[103] J. S. Lim, L. Serra, R. López, and R. Aguado, Phys. Rev. B **86**, 121103 (2012).

[104] S. Das Sarma, J. D. Sau, and T. D. Stanescu, Phys. Rev. B **86**, 220506 (2012).

[105] D. Rainis, L. Trifunovic, J. Klinovaja, and D. Loss, Phys. Rev. B **87**, 024515 (2013).

[106] D. Sticlet, C. Bena, and P. Simon, Phys. Rev. Lett. **108**, 096802 (2012).

[107] M. Guigou, N. Sedlmayr, J. Aguiar-Hualde, and C. Bena, arXiv:1407.1393 .

[108] J. Nilsson, A. R. Akhmerov, and C. W. J. Beenakker, Phys. Rev. Lett. **101**, 120403 (2008).

[109] S. Bose and P. Sodano, New J. Phys. **13**, 085002 (2011).

[110] H.-F. Lü, H.-Z. Lu, and S.-Q. Shen, Phys. Rev. B **86**, 075318 (2012).

[111] J. Liu, F.-C. Zhang, and K. T. Law, Phys. Rev. B **88**, 064509 (2013).

[112] B. Zocher and B. Rosenow, Phys. Rev. Lett. **111**, 036802 (2013).

[113] J. Alicea, Y. Oreg, G. Refael, F. von Oppen, and M. P. Fisher, Nat. Phys. **7**, 412 (2011).

[114] M.-T. Rieder, G. Kells, M. Duckheim, D. Meidan, and P. W. Brouwer, Phys. Rev. B **86**, 125423 (2012).

[115] F. Merz and J. T. Chalker, Phys. Rev. B **65**, 054425 (2002).

[116] C. W. J. Beenakker, Rev. Mod. Phys. **87**, 1037 (2015).

[117] R. M. Lutchyn, T. D. Stanescu, and S. Das Sarma, Phys. Rev. Lett. **106**, 127001 (2011).

[118] A. Papoulis, *Probability, Random Variables, and Stochastic Processes* (2nd ed. New York: McGraw-Hill, 1984).

[119] G. Ben-Shach, A. Haim, I. Appelbaum, Y. Oreg, A. Yacoby, and B. I. Halperin, Phys. Rev. B **91**, 045403 (2015).

[120] D. Vasyukov, Y. Anahory, L. Embon, D. Halbertal, J. Cuppens, L. Neeman, A. Finkler, Y. Segev, Y. Myasoedov, M. L. Rappaport, *et al.*, Nat. Nanotech. **8**, 639 (2013).

[121] H. Mamin, M. Kim, M. Sherwood, C. Rettner, K. Ohno, D. Awschalom, and D. Rugar, Science **339**, 557 (2013).

[122] A. D. K. Finck, D. J. Van Harlingen, P. K. Mohseni, K. Jung, and X. Li, Phys. Rev. Lett. **110**, 126406 (2013).

[123] K. Flensberg, Phys. Rev. B **82**, 180516 (2010).

[124] G. Kells, D. Meidan, and P. W. Brouwer, Phys. Rev. B **85**, 060507 (2012).

[125] F. Pientka, G. Kells, A. Romito, P. W. Brouwer, and F. von Oppen, Phys. Rev. Lett. **109**, 227006 (2012).

[126] P. Anderson, J. Phys. Chem. Solids **11**, 26 (1959).

[127] A. C. Potter and P. A. Lee, Phys. Rev. Lett. **105**, 227003 (2010).

[128] M. Wimmer, A. R. Akhmerov, J. P. Dahlhaus, and C. W. J. Beenakker, New J. Phys. **13**, 053016 (2011).

[129] J. Sau and S. Sarma, Nat. Commun. **3**, 964 (2012).

[130] M. Leijnse and K. Flensberg, Phys. Rev. B **86**, 134528 (2012).

[131] T.-P. Choy, J. M. Edge, A. R. Akhmerov, and C. W. J. Beenakker, Phys. Rev. B **84**, 195442 (2011).

[132] M. Kjaergaard, K. Wölms, and K. Flensberg, Phys. Rev. B **85**, 020503 (2012).

[133] H. Grabert and M. H. Devoret, Physics (Plenum Press, New York, 1992) (1992).

[134] B. Braunecker, G. I. Japaridze, J. Klinovaja, and D. Loss, Phys. Rev. B **82**, 045127 (2010).

[135] J. D. Sau, D. J. Clarke, and S. Tewari, Phys. Rev. B **84**, 094505 (2011).

בפרק 3 אנו בוחנים חתימות של מצבי מָיוֹרָנָה קשורים. שני החלקים הראשונים של הפרק דנים במִתְאָם בין זרמים חשמליים במערך אותו אנו מכנים "מְפָצֵל אלומה מסוג מָיוֹרָנָה". מערך זה הינו צומת-קָמָץ המורכב משתי זרועות עשיות מוליך רגיל במתח חשמלי, V, ומְרָגֵל אמצעית עשויה מוליך-על טופולוגי מֵאֲרָק. אנו מראים שהִמָּצְאוּת מצב מָיוֹרָנָה קשור ומבודד בצומת מכתיבה התנהגות אוניברסלית של המִתְאָם בין הזרמים בשתי הזרועות. המִתְאָם הבֵּין-זַרְמִי הינו שלילי ודועך לאפס כמו $-1/V$ במתחים גבוהים. התנהגות זו נותרת עמידה גם בנוכחות של אי-סדר ושל ערוצים רוחביים מרובים, ואף שורדת בטמפרטורות סופיות. בניגוד לכך, מצב קשור מְקָרִי מְסוּג אָנְדֶרֵייב בעל אנרגיה נמוכה גורם להתנהגות לא אוניברסלית של המִתְאָם הבֵּין-זַרְמִי. אנו מנתחים בפירוט את המקרה של מִתְאָם בֵּין-זַרְמִי מופרד-סְחָרוּר, היכן שההבחנה בין המקרה של מצב המָיוֹרָנָה הקשור והמקרה של מצב האָנְדֶרֵייב הקשור היא החדה ביותר. בחלקו האחרון של הפרק אנו בוחנים מצב בו מוליך העל-הטופולוגי הינו ארוך אך סופי, כך שישנה חפיפה מרחבית בין שני מצבי המָיוֹרָנָה הקשורים בשני קצוותיה של המערכת. בעוד שבמערכת אינסופית מצבי המָיוֹרָנָה הקשורים אינם נושאים מטען חשמלי, אין זה עוד המקרה כאשר מיקומיהם של מצבי המָיוֹרָנָה הקשורים מתחילים לחפוף. אנו מראים שהגם ששיאה של צפיפות המצבים מתקבל בקצוותיה של המערכת, המטען החשמלי הנישא על-ידי מצבי המָיוֹרָנָה הקשורים מָרוּחַ על פני המערכת. ההתנהגות הלא-אינטואיטיבית הזו יכולה לשמש כחתימה ניסויית של מצבי מיורנה קשורים מצומדים-בְּחֻלְשָׁה במערכות סופיות.

בפרק 4 אנו בוחנים באופן תיאורטי את האפשרות של מימוש מצבי מָיוֹרָנָה קשורים במערך ניסויי נשלט ואיתן. אנו מציעים להשיג זאת על-ידי פיצול של המערכת לשרשרת של נקודות קוונטיות, אשר מכוונות לעמוד בתנאים בהם המערכת יכולה להיחשב באופן אפקטיבי כמודל קִיטָייֵב, כך שהיא במצב טופולוגי מוגן מלווה במצבי מָיוֹרָנָה קשורים בנקודות הקיצוניות של השרשרת. מערך זה מתגבר על מכשולים, המוצבים על ידי אי-סדר וצפיפות-מצבים גבוהה, בדרך אל מימוש מצבי מיורנה קשורים מופרדים. אלגוריתם הכיוון של המערכת שאנו מציגים כולל שליטה במתחי שְׁעָרִים חשמליים ובפאזות של מוליכי-על. ספקטרוסקופיה תְּהוּדָתִית מסוג אָנְדֶרֵייב מאפשרת לנו לבצע את הכיוון באופן סתגלני, כאשר בכל שלב זוג נקודות קוונטיות עובר כיוון באופן בלתי תלוי בזוגות האחרים. חישוב של המוליכות הדיפרנציאלית אשר מראה שישנו שיא מְקוּוָנְטָט במתח חשמלי אפסי משמש כחתימה של טיבה הטופולוגי של הפאזה.

תקציר

ב-1937 אֶטוֹרֶה מָיוֹרָנָה העלה השערה על קיום של חלקיק שהוא האנטי-חלקיק של עצמו. השאלה האם חלקיק זה - אשר קיבל את השם "פֶּרְמִיוֹן הַמָיוֹרָנָה" - מתקיים בטבע כחלקיק יסודי נותרת כיום ללא מענה. בתחום הפיסיקה של חומר מָעוּבֶּה, לעומת זאת, אין אנו מוגבלים על-ידי נדיבותו של הטבע. אכן, פֶּרְמִיוֹן הַמָיוֹרָנָה (אשר מכונה לרוב אוֹפַן מָיוֹרָנָה מאוּפָּס או מצב מָיוֹרָנָה קשׁוּר בהקשרים של פיסיקת החומר המעובה) יכול להתהוות כְּעֵירוּר בעל אפס אנרגיה על גבולה של פאזה חדשה הנקראת מוליכות-על טופולוגית. פאזה זו יכולה להיווצר במערכות בעלות מספר נמוך של ממדים כתוצאה משילוב של מוליכות-על, מגנטיות וצימוּד סְחָרוּר-מְסִילָה. הרבה מהעניין שמעוררים מצבי המיורנה הקשורים נובע מטיבם האִי-מְקוֹמִי, תכונה אשר מותירה אותם חסרי רגישות להפרעות מקומיות ולאיבוד קוֹהֶרֶנְטִיוּת. כתוצאה מכך, ומסטטיסטיקת חליפין אי-חילופית, יש להם פוטנציאל לשמש בעתיד כמצע לטובת עיבוד מידע קוונטי עמיד-שגיאות.

בבואנו לחקור מצבי מָיוֹרָנָה קשורים במערכות של פיסיקת החומר המעובה, בין אם מנקודת מבט תיאורטית ובין אם מנקודת מבט יישומית, עולות מספר שאלות. ראשית, מהן המערכות אשר מניבות מוליכות-על טופולוגית? ובפרט, מהם המערכים הפיסיקאליים האיתנים ביותר ואשר מאפשרים שליטה מרבית על מצבי המָיוֹרָנָה הקשורים? שנית, מהן החתימות הפיסיקאליות של מצבי המָיוֹרָנָה הקשורים במערכות אלו? ובפרט, האם ביכולתנו להבחין בתכונת אי-המקומיות שלהם? בתזה המוצגת כאן, אנו מנסים לשפוך אור על נושאים אלו.

אנו מתחילים בפרק 1 בהיכרות עם נושא מוליכות העל הטופולוגית, ובסקירה של ההתפתחויות האחרונות אשר הובילו אל מצב העניינים העדכני בחקר מצבי המָיוֹרָנָה הקשורים. אנו מתרכזים בפרט במימושים של מוליכות-על טופולוגית במערכות ננו-חוטים מוליכים למחיצה, ובחתימות של מצבי מָיוֹרָנָה קשורים במדידות של מוליכות דיפרנציאלית במערכות אלה.

פרק 2 עוסק במימוש של מוליך-על טופולוגי בעל סימטריה להיפוך בזמן. אנו מראים, שבניגוד למקרה בו הסימטריה להיפוך בזמן נשברת, כאן הידוד אלקטרון-אלקטרון דוחה הינו הכרחי למימוש של הפאזה הטופולוגית. בפרט, לא ניתן לממש פאזה זו על-ידי צימוד של מערכת של אלקטרונים בלתי-מהדדים למוליך-על קונבנציונאלי. בשלב הבא אנו פונים לחקור את ההשפעה של הידוד אלקטרון-אלקטרון דוחה. אנו מציגים וחוקרים מודל אנרגיות-נמוכות כללי עבור מערכת חד-ממדית בָּקְרָבָה למוליך-על, ומראים שמודל זה נכנס אל פאזת מוליך-העל הטופולוגי הסימטרי להיפוך בזמן כתוצאה מהידוד דוחה קצר-טווח. את ההשפעה של הידוד האלקטרונים אנו חוקרים בעזרת קירוב שדה-ממוצע ובעזרת ניתוח של חֲבוּרַת הָרֶנוֹרְמָלִיזַצְיָה. בנוסף, אנו מציעים שני מערכים ניסויים ומראים שהם מתוארים באנרגיות נמוכות על יד המודל הנ"ל. כדי לבחון את מסקנותינו, אנו בוחנים מודל מיקרוסקופי עבור אחד המערכים הללו בעזרת חישוב הַרְטְרִי-פּוֹק נומרי ובעזרת חבורת הרנורמליזציה של מטריצת הצפיפות.

מכון ויצמן למדע

WEIZMANN INSTITUTE OF SCIENCE

Thesis for the degree
Doctor of Philosophy

Submitted to the Scientific Council of the
Weizmann Institute of Science
Rehovot, Israel

עבודת גמר (תזה) לתואר
דוקטור לפילוסופיה

מוגשת למועצה המדעית של
מכון ויצמן למדע
רחובות, ישראל

By
Arbel Haim

מאת
ארבל חיים

מצבי מָיוֹרָנָה קשורים במערכות חומר מעובה: מימושים וחתימות פיסיקאליות

Majorana Bound States in Condensed Matter Systems: Realizations and Physical Signatures

Advisor:
Prof. Yuval Oreg

מנחה:
פרופ' יובל אורג

August 2016

ניסן תשע"ו